nature cell biology

Article

https://doi.org/10.1038/s41556-024-01530-8

SERRATE drives phase separation behaviours to regulate m6A modification and miRNA biogenesis

Received: 7 December 2023

Accepted: 12 September 2024

Published online: 29 October 2024

Check for updates

Songxiao Zhong[1], Xindi Li[1], Changhao Li[1], Haiyan Bai[2], Jingjing Chen[2], Lu Gan[3,4], Jiyun Zhu[1], Taerin Oh[1], Xingxing Yan[1], Jiaying Zhu[1], Niankui Li[1], Hisashi Koiwa[5], Thomas Meek[1], Xu Peng[6], Bin Yu[3], Zhonghui Zhang[2] ✉ & Xiuren Zhang[1,7] ✉

The methyltransferase complex (MTC) deposits *N*6-adenosine (m^6A) onto RNA, whereas the microprocessor produces microRNA. Whether and how these two distinct complexes cross-regulate each other has been poorly studied. Here we report that the MTC subunit B tends to form insoluble condensates with poor activity, with its level monitored by the 20S proteasome. Conversely, the microprocessor component SERRATE (SE) forms liquid-like condensates, which in turn promote the solubility and stability of the MTC subunit B, leading to increased MTC activity. Consistently, the hypomorphic lines expressing SE variants, defective in MTC interaction or liquid-like phase behaviour, exhibit reduced m^6A levels. Reciprocally, MTC can recruit the microprocessor to the *MIRNA* loci, prompting co-transcriptional cleavage of primary miRNA substrates. Additionally, primary miRNA substrates carrying m^6A modifications at their single-stranded basal regions are enriched by m^6A readers, which retain the microprocessor in the nucleoplasm for continuing processing. This reveals an unappreciated mechanism of phase separation in RNA modification and processing through MTC and microprocessor coordination.

Biomolecules such as intrinsically disordered proteins (IDPs) and nucleic acids can form discrete condensates and membrane-less compartments within a cellular or solute milieu[1]. IDPs typically contain unfolding regions that might serve as docking points for homotypic or heterotypic multi-valent interactions, instigating phase separation or co-phase separation[2]. Liquid–liquid phase separation (LLPS) can amplify enzymatic reactions[3] and facilitate transcription[4,5] and RNA metabolism[6,7], among other biological processes[3,8]. Nonetheless, biomolecules may also assemble comparatively inert or inactive condensates. For example, IDPs can undergo spontaneous phase transition among heterogeneous behaviours, known as maturation and hardening, enabling functional switch[1,9]. To overcome these disorders or constraints, cells can deploy molecular chaperones for maintaining protein conformation and proteasomes for eliminating the misfolded proteins[10]. The plant kingdom encodes a multitude of IDPs, yet only a tiny fraction have been studied concerning their phase behaviours and physiological relevance[11,12].

[1]Department of Biochemistry and Biophysics, Texas A&M University, College Station, TX, USA. [2]Guangdong Provincial Key Laboratory of Biotechnology for Plant Development, School of Life Science, South China Normal University, Guangzhou, China. [3]School of Biological Sciences and Center for Plant Science Innovation, University of Nebraska–Lincoln, Lincoln, NE, USA. [4]Biotechnology Research Institute, Chinese Academy of Agricultural Sciences, Beijing, China. [5]Department of Horticulture, Texas A&M University, College Station, TX, USA. [6]Department of Medical Physiology, College of Medicine, Texas A&M University, College Station, TX, USA. [7]Department of Biology, Texas A&M University, College Station, TX, USA. ✉e-mail: zhzhang@m.scnu.edu.cn; xiuren.zhang@tamu.edu

SERRATE (SE), the plant homologue of mammalian arsenic resistance protein 2 (ARS2), is a multi-functional IDP that acts in transcription, microRNA (miRNA) biogenesis and pre-messenger RNA splicing, among other processes[13]. SE also undergoes LLPS to facilitate the processing of primary miRNA substrates (pri-miRNAs) by the microprocessor and shuttling of miRNA/* duplexes to the RNA-induced silencing complex[6,14]. Conversely, two other IDPs, namely, SAID1/2, can form co-condensates with SE and sequester pri-miRNAs from the microprocessor to inhibit miRNA production[15]. Notably, misfolded or unsheltered SE is degraded by the 20S proteasome[16,17]. These findings illuminate that SE, through its intrinsically disordered properties, serves as an assemblage nexus for multiple ribonucleoprotein (RNP) complexes to orchestrate the above-mentioned RNA processing eve nts[13]. This notwithstanding, it remains unclear whether and how SE/ARS2 contribute to additional RNA metabolism exemplified by epitranscriptome modifications.

mRNA adenosine methyltransferase complex subunit A and B (MTA and MTB), plant homologues of mammalian methyltransferase-like 3 and 14 (METTL3 and METTL14), respectively, function as essential constituents of the methyltransferase complex (MTC) that catalyse *N*6-adenosine (m^6A) deposition. METTL3, once fused with a low-complexity domain of *Arabidopsis* photoreceptor protein CRY2, displays punctuated foci in mammalian cells[18]. In *Arabidopsis*, MTA seems to undergo co-LLPS with CRY2, granting light regulation of m^6A of circadian clock-associated transcripts[19]. Intriguingly, m^6A itself can also serve as a scaffold facilitating the phase separation of RNP complexes[20,21]. In eukaryotes, the m^6A level is positively correlated with miRNA amount[22–24]. The m^6A modification might locate in a stem-loop region, triggering a structural switch of pri-miRNAs that would be recognized by an RNA-binding protein and enabling the recruitment of DGCR8 for processing[24,25]. Alternatively, METTL3/MTA can recruit DGCR8 or TOUGH to facilitate pri-miRNA processing[22,23]. However, whether and how MTB undergoes the regulation of phase behaviours is unknown. In addition, the precise mechanism underlying MTC regulation of pri-miRNA processing remains unclear.

Here, we identified a non-canonical function of SE in promoting MTC-mediated m^6A deposition. Unlike well-folded METTL14, MTB is an IDP and prone to forming insoluble condensates. However, SE could utilize its liquid-like phase behaviours to maintain the MTB solubility, allowing the uptake of RNA substrate by MTC to fulfil the enzymatic activity. Moreover, co-condensation of SE and MTB could also mutually protect each other from degradation by the 20S proteasome. Reciprocally, MTC could tether the microprocessor to chromatin, facilitating co-transcriptional pri-miRNA processing. Furthermore, MTC could deposit m^6A onto single-strand (ss) basal regions of pri-miRNAs, enabling m^6A readers to retain the microprocessor for further processing in the nucleoplasm. Thus, this study reveals how the two IDPs fine tune their phase behaviours to regulate the epitranscriptome modification, and how the two otherwise separate complexes orchestrate each other to promote miRNA production.

Results

SE displays spatiotemporal and physical association with MTC

To explore additional functions of SE, we conducted a pan co-expression network analysis for principal components of microprocessor and MTC using over 1,000 RNA sequencing (RNA-seq) datasets[26] (Extended Data Fig. 1a and Supplementary Table 1). *SE*, *HYL1* and *TOUGH* mutually exhibited moderate correlations, whereas their coordination with *DCL1* was less pronounced. Importantly, substantial correlations emerged among *MTA*, *MTB* and *SE*. Another MTC subunit, *FK506-BINDING PROTEIN 12 KD INTERACTING PROTEIN 37KD* (*FIP37*), also showed a robust correlation with *SE*. Furthermore, *MTA* and *MTB* displayed correlation to other microprocessor components to a certain extent, but not with the control gene, *Actin*. Additionally, *SE* and *MTC* depicted a co-expression pattern throughout various tissue (Extended Data Fig. 1b). To investigate whether SE and MTC functioned genetically in a parallel or cooperative manner, we generated knockdown mutants for *MTA*, *MTB* and *FIP37* (Extended Data Fig. 2a–f). All MTC mutants displayed developmental defects reminiscent of *se*, exemplified by upward-curly and narrow true leaves on 1-week-old seedlings, as well as notched and trident-like, irregularly curled leaves, and stunted growth on 3-week-old plants (Fig. 1a, Extended Data Fig. 2g). Subsequent RNA-seq profiling revealed a significant overlap of differentially expressed genes between *se-2* and *mta* (Fig. 1b and Supplementary Table 2). Moreover, yeast two hybrid (Y2H) screening assays showed that SE directly interacted with MTB and FIP37 but not with MTA (Fig. 1c and Extended Data Fig. 2h). Additionally, co-immunoprecipitation (co-IP), luciferase complementation imaging (LCI) and bimolecular fluorescence complementation (BiFC) (Fig. 1d and Extended Data Fig. 2i–m) further validated the association of SE with MTC. These results all suggest that SE and MTC might function within a shared genetic pathway.

SE impacts transcriptome-wide m^6A deposition

We next assessed the impact of SE on m^6A deposition through high-performance liquid chromatography tandem mass spectrometry (HPLC–MS). We quantified the m^6A amount of poly(A)+ RNAs with two controls (Extended Data Fig. 3a). Indeed, *se-2*, like *mta*, displayed a significant reduction in m^6A versus Col-0 (Fig. 1e). Next, we conducted methylated RNA immunoprecipitation (MeRIP) assays (Extended Data Fig. 3b). Whereas the starting amount of RNA input was comparable across the samples, MeRIP-enriched signals of m^6A-harboured fragments were clearly reduced for *se-2* and *mta* mutants versus Col-0 (Extended Data Fig. 3c), indicative of reduced levels of methylated mRNAs from the mutants versus Col-0.

To quantitatively compare the m^6A epitranscriptome across different samples, we recalled over 50,000 m^6A candidate peaks via exomePeak2 software with a setting of $\log_2$(enrichment) >0 (Supplementary Table 3). We defined high-confidence (HC)-m^6A peaks of interest using a threshold of $P < 0.05$ and $\log_2$(enrichment) >1, while the rest of peaks were claimed as non-significant-m^6A peaks and used as controls for comparative analysis with DEseq2. In this scenario, we identified 11,487 HC-m^6A peaks in Col-0, wherein a substantial proportion of the peaks were hypomethylated in *se-2* and *mta* (Fig. 1f,g and Supplementary Table 3). Specifically, 7,496 and 9,097 peaks were hypomethylated on 7,302 and 8,672 transcripts in *se-2* and *mta*, respectively, with 6,968 in common (Fig. 1h,i). A meta-analysis of m^6A-enriched reads showed reduced distributions at the 3′ end of transcripts (Fig. 1j). A motif analysis of the hypo-peaks revealed the presence of the canonical m^6A motif, RRACH context (R = A and G; H = A, C and U) and the plant-specific URUAY (Y = C and U) motif (Extended Data Fig. 3d)[27].

Similarly, we obtained a total of 11,963 and 11,667 seemingly 'HC'-m^6A peaks in *se-2* and *mta*, respectively, with 1,494 and 3,309 peaks enriched specifically in the according mutants (Supplementary Table 3). These peaks are probably false positives (hereafter referred to as FP-m^6A peaks) in part due to the internal normalization algorithm within the samples, given that the overall m^6A level on FP-m^6A peaks was reduced in the mutants versus Col-0 (Fig. 1k). Furthermore, Go Ontology (GO) analysis showed that the m^6A transcripts co-regulated by SE and MTA were significantly enriched in metabolic processes and proteasome-activating and lipid transporter pathways (Fig. 1l). Taken together, these results indicated that SE may promote MTC-mediated m^6A deposition.

IDRs confer the SE–MTB interaction

We employed an in silico approach to explore the structural basis underlying the contribution of MTB–SE contribution to m^6A deposition. Both IUPred3 (ref. 28) and neural network-based[29] bioinformatic analyses suggested that plant MTBs, unlike their counterparts in metazoans and fungi, had largely extended N-terminal IDRs (up to 600 amino acids (a.a.)), whereas plant MTAs exhibited a comparable

https://doi.org/10.1038/s41556-024-01530-8

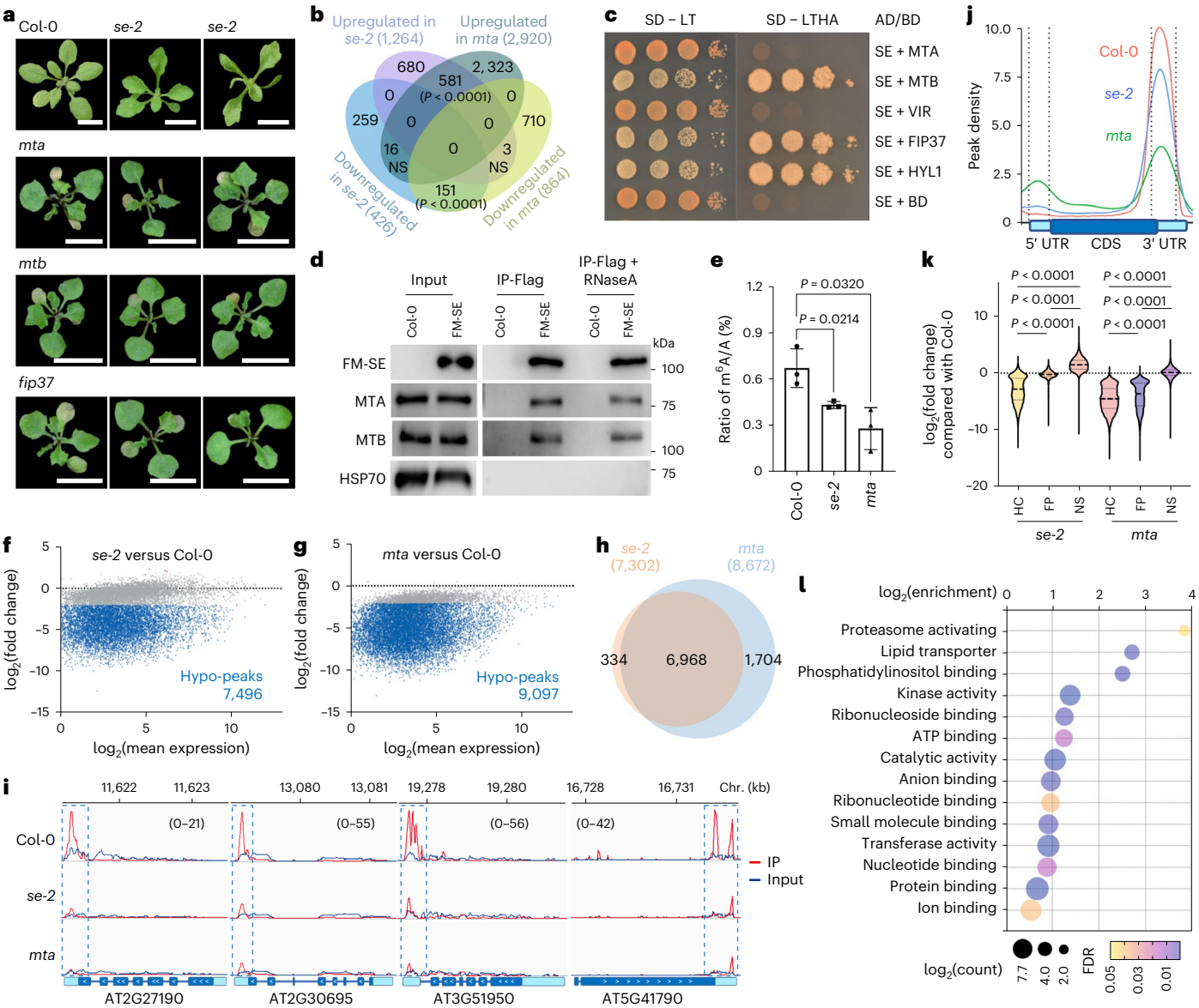

Fig. 1 | SE promotes m^{6}A modification in *Arabidopsis*. **a**, *mta*, *mtb* and *fip37* displayed developmental defects in 3-week-old plants. Scale bar, 1 cm. **b**, A Venn diagram illustrating significant overlap of differentially expressed genes between *se-2* and *mta* mutants versus Col-0. *P* values for shared upregulated and downregulated genes in *se-2* and *mta* are both <0.0001. **c**, Y2H screening identified MTB and FIP37 as additional partners of SE. VIR, virilizer; SD−LT, synthetic defined medium lacking Leu and Trp; −LTHA, lacking Leu, Trp, His and Ade; AD/BD, transcription activation/DNA-binding domain. **d**, Co-IP assays validated the interaction between SE and MTC in the stable transgenic plants of Col-0; *pSE::Flag-4×MYC(FM)-SE*. IPs were conducted with anti-Flag antibodies. Immunoblots were detected with anti-Flag or endogenous protein antibodies, respectively. HSP70 was a negative control. **e**, HPLC–MS analysis revealed a significant reduction of m^{6}A global abundance in *se-2* and *mta* versus Col-0. Data are mean ± s.d. of three independent experiments. *P* values for *se-2* and *mta* versus Col-0 are 0.0214 and 0.0320, respectively. **f**,**g**, MA plots show the differentially methylated peaks in *se-2* (**f**) and *mta* (**g**) versus Col-0. The red, blue and grey dots represent hypermethylated ($\log_2$(fold change) >2, *P* < 0.01), hypomethylated ($\log_2$(fold change) <−2, *P* < 0.01) and comparable methylated m^{6}A peaks, respectively. **h**, A Venn diagram showing the overlap of hypomethylated genes from MeRIP-seq between *se-2* and *mta* when compared with Col-0. **i**, IGV files of selected hypomethylated genes. IP and input are represented in red and blue, respectively. Chr., chromosome. **j**, Metagene profile showing m^{6}A distribution across the gene body, with the *x* and *y* axes representing the relative position and abundance of m^{6}A modification on transcripts, respectively. UTR, untranslated region. **k**, A violin plot showing peak differential methylation levels enriched in mutants relative to Col-0. The lines represent the median (dashed) and quartiles (dotted). NS, non-significant m^{6}A peaks. *P* values for all comparisons are <0.0001. **l**, GO analysis of shared hypomethylated genes in mutants versus Col-0. FDR, false discovery rate. At least 15 independent transgenic lines were photographed (**a**), ten independent colonies (**c**) and three biological replicates (**d**) were tested, and representative images are shown. Hypergeometric distribution test (**b** and **l**), unpaired two-sided *t*-test (**e**), DESeq2 (**f** and **g**) and one-way ANOVA with Dunnett's multiple comparison test (**k**) were used.

feature to mammalian METTL3 (Fig. 2a–c and Extended Data Fig. 4a–e). A three-dimensional (3D) simulation of the MTA–MTB heterodimer via AlphaFold-multimer[30] showed that the core domains assembled in an architecture reminiscent of human MTC[31] (Extended Data Fig. 4g). Subsequently, the simulation of SE–MTB assembly revealed that IDRs of the two proteins intermingled each other (Extended Data Fig. 4h) with the majority of interactive hydrogen bonds (IHBs) harboured in their IDRs (Extended Data Fig. 4b–e). Indeed, Y2H assays validated that the C-terminal region (469–720 a.a.) of SE interacted with the N-terminal IDR (1–634 a.a.) of MTB (Fig. 2f). Computation analysis

predicted that seven putative a.a. within the C-terminal region of SE may serve as donors for IHBs with MTB (Extended Data Fig. 4i). Y2H assays with alanine scanning variants of seven potential hydrogen bond donors (562, 580, 584, 586, 589, 666 and 718) pinpointed R718 as a critical residue for the interaction of SE with MTB, but not with DCL1 (Fig. 2f,g). Importantly, R718 was depleted in all *se* mutants (Fig. 2h)

SE modulates phase behaviours of MTB in vitro

Since SE and MTB are IDPs and interact with each other, we next investigated their phase behaviours. Recombinant SE indeed formed spherical condensates (Extended Data Fig. 5a,b). This phase behaviour relied on the N-terminal IDR (IDR1) as its depletion (SEΔIDR1) disrupted the condensation, and the defect could be rescued by the fusion of a low-complexity domain from mammalian FUS (LCD^{FUS}-SEΔIDR1), as observed previously[6] (Extended Data Fig. 5a,b). Moreover, SE-R718A showed analogous LLPS capability to wild-type (WT) SE and LCD^{FUS}-SEΔIDR1 (Extended Data Fig. 5a,b). This result indicated that the mutation of R718A did not alter SE phase behaviour despite compromising its interaction with MTB in vitro.

Recombinant MTB was soluble in a 500 mM salt buffer but turned turbid upon lowering the salt concentration to 150 mM (Extended Data Fig. 5c). Subsequent microscopic examination revealed irregular morphology of MTB condensates (Fig. 2i). MTA remained soluble under low salt conditions but became susceptible to irregular condensate upon stimulation by a crowder (5% Ficoll) (Extended Data Fig. 5e). Notably, these condensates could not be disrupted with the addition of 10% 1,6-hexanediol (1,6-HD), indicative of insoluble states (Fig. 2i and Extended Data Fig. 5d). In addition, the phase behaviours of neither MTA nor MTB were affected by fluorescence tag (Extended Data Fig. 5e).

The strong tendency of SE–MTB to form heterotypic assembly raised a question of whether SE could impact the phase behaviours of MTB. To test this, we conducted in vitro phase separation assays in different ways. We first reduced the salt concentration of the protein solutions to 150 mM NaCl, and then mixed the two proteins in the identical condition. Upon dilution, MTB promptly aggregated, leaving SE onto the surface of insoluble condensates, thereby forming co-condensates in irregular shapes (Fig. 2j, top). Consequently, a few puncta comprising solely SE were observed (Fig. 2j, top). We next mixed the solution of two proteins before the buffer conversion. Similarly, the procedure also resulted in concurrent irregular condensates (Fig. 2j, middle). These observations prompted us to hypothesize whether the initial formation of SE droplets is necessary to avert protein aggregation. To test this, a gradient amount of SE was used for droplet assembly before the addition of MTB (Fig. 2j, bottom). This time, upon mixing, SE and MTB simultaneously exhibited a spherical morphology when SE was tenfold or more the amount of MTB (Fig. 2j, bottom). However, increasing the ratio of MTB/SE would readily cause the formation of irregular condensates (Fig. 2k). Moreover, the use of LCD^{FUS}-SEΔIDR1, but neither SE-R718A nor SEΔIDR1, displayed spherical co-condensates (Fig. 2l). In addition, the human LCD^{FUS} condensates were unable to confer the liquid-like behaviour to MTB (Extended Data Fig. 5f). These results indicated that SE droplets could modulate the phase behaviours of MTB, a process entailing direct interaction at the C-terminal of SE and the intrinsic LLPS properties conferred by the N-terminal IDR of SE. In contrast, a mixture of MTA and MTB in this scenario formed exclusively irregular co-condensates (Extended Data Fig. 5g).

We further assessed the phase behaviours of SE–MTB co-condensates. The 3D rendering images revealed that both SE and MTB indeed displayed a spherical shape (Extended Data Fig. 5h). The condensates were disrupted by addition of 1,6-HD (Fig. 2l, bottom). Importantly, the approaching droplets that consisted of two proteins were able to fuse into one larger condensate (Fig. 2m). In addition, fluorescence recovery after photobleaching (FRAP) assays showed the recovery of fluorescence after bleaching, indicative of the bona fide mobility of SE–MTB condensates (Fig. 2n,o). Taken together, the observations indicated that pre-existing SE liquid droplets would be a perquisite of controlling the phase behaviour of MTB to prevent the protein aggregation in vitro.

MTC displays SE-dependent LLPS in vivo

We next asked whether SE could influence the phase behaviours of MTC in vivo. We co-expressed MTA–cyan fluorescent protein (CFP), yellow fluorescent protein (YFP)–MTB and mCherry–SE in mesophyll cells obtained from Col-0. The rendered 3D fluorescence revealed that the three proteins co-localized within discrete, spherical condensates (Extended Data Fig. 5i,j). Time-lapse live imaging demonstrated that two approaching condensates could fuse into one larger body (Extended Data Fig. 5k). Furthermore, FRAP assays revealed that both signals regained within a 2 min timeframe, suggesting a dynamic fluidity intrinsic to the SE–MTC co-condensates in vivo (Extended Data Fig. 5l,m).

In parallel, we prepared protoplasts from *se-1* in which the SE protein is negligibly presented. In this situation, MTA–CFP and YFP–MTB also exhibited condensates (Extended Data Fig. 5n). However, these condensates could not recover after bleaching in FRAP assays (Fig. 3a), indicative of gel-like or solid-like phase behaviours, reminiscent of their in vitro patterns (Extended Data Fig. 5f) and also some other insoluble RNPs in vivo[32–34]. Again, the supplement of WT SE and LCD^{FUS}-SEΔIDR1, but not SE-R718A or SEΔIDR1, could confer fluid properties to the co-condensates as the fluorescence of the former, but not the latter condensates, was quickly recovered after bleaching as observed in Col-0 (Fig. 3a and Extended Data Fig. 5n). Additionally, treatment of 1,6-HD disrupted the SE-granted mobility of MTC condensates, reflecting by a hardening of the complex (Fig. 3a and Extended Data Fig. 5n).

Furthermore, we transiently expressed MTC and SE under the 35S promoter or their native promoters in *Nicotiana benthamiana*.

Fig. 2 | SE modulates the phase behaviours of MTC in vitro. a, Phylogenetic tree showing that plant MTBs have extended N-terminal IDRs. **b**,**c**, Computational simulation-predicted disordered (red) and ordered (blue) regions of MTB (**b**) and SE (**c**) and their IHBs. The triangles and the right *y* axis show IHBs and their corresponding distances, respectively. Ave, average; MTD, methyltransferase domain; ZF, zinc finger; FRG, (F/Y)RG motif enriched region. **d**,**e**, Simulation indicating the significant enrichment of IHBs in the IDRs of MTB (**d**) and SE (**e**) in the complex. *P* values for H bond versus no H bond at MTB and SE are <0.0001 and 0.0002, respectively (two-sided Fisher's exact test). **f**, Fine mapping of SE–MTB interaction regions. 7As-SE, alanine substitutes of all seven potential IHB donors in SE; 6As-SE, a variant resembling 7As-SE except R718. Refer to Fig.1c for the legend. **g**, Simulation identifying R718 as key in the SE–MTB interaction. **h**, Illustration of alleles of *se* mutants. T-DNA, transfer DNA. **i**, In vitro phase behaviours of 3 μM YFP–MTB in the droplet buffer with or without 10% 1,6-HD. **j**, Confocal microscopy detected three non-exclusive SE–MTB co-condensate scenarios. The top, middle and bottom images show MTB aggregates encapsulated inside a SE shell, the co-aggregation and fully overlapping spherical condensates, respectively, using 1 μM of SE and 0.5 μM (top and middle) or 0.1 μM (bottom) of MTB. **k**, Confocal microscopy of SE–MTB in vitro co-condensation at different ratios. SE versus MTB (in μM), from top to bottom, 10 versus 0, 5 versus 0.15, 1.5 versus 0.5 and 0.5 versus 3. **l**, Confocal microscopy shows the dependence of SE–MTB co-condensation on the IDR1 of SE and its interaction with MTB in vitro. SE-R718A, which has compromised interaction with MTB; SEΔIDR1, which lacks the N-terminal IDR; LCD^{FUS}-SEΔIDR1, a chimeric protein of human FUS's LCD and SEΔIDR1. **m**, Time-lapse live images showing the fusion of SE–MTB co-condensates. **n**,**o**, FRAP analysis (**n**) and recovering curves (**o**) showed the mobility of SE–MTB condensates in vitro. Data are mean ± s.d. of eight independent experiments. BF, bright field (**j**–**m**). At least ten colonies (**f**) and three (**i**–**m**) or eight (**o**) independent experiments were performed, and representative images are shown. Scale bars, 10 μm (**i** and **m**), 5 μm (**j**–**l**) and 2.5 μm (**n**).

https://doi.org/10.1038/s41556-024-01530-8

In either case, SE and MTC could form co-condensates, despite the lower expression under the native promoters leading to fewer and smaller co-condensates than that of 35S promoter (Extended Data Fig. 6a). Notably, the co-condensates exhibited similar mobility regardless of protein levels in vivo (Extended Data Fig. 6b–d). Finally, we assessed phase separation of native MTB that was expressed via its own promoter in stable transgenic plants. Again, MTB and SE could form co-condensates in both somatic cells and pollens (Fig. 3b,c). Clearly, the condensates displayed mobility as the fluorescence were recuperated within a 30 s duration in FRAP assays (Extended Data Fig. 6e). Furthermore, the application of 1,6-HD induced a phase transition to hardened condensates (Extended Data Fig. 6e). Importantly, the MTB

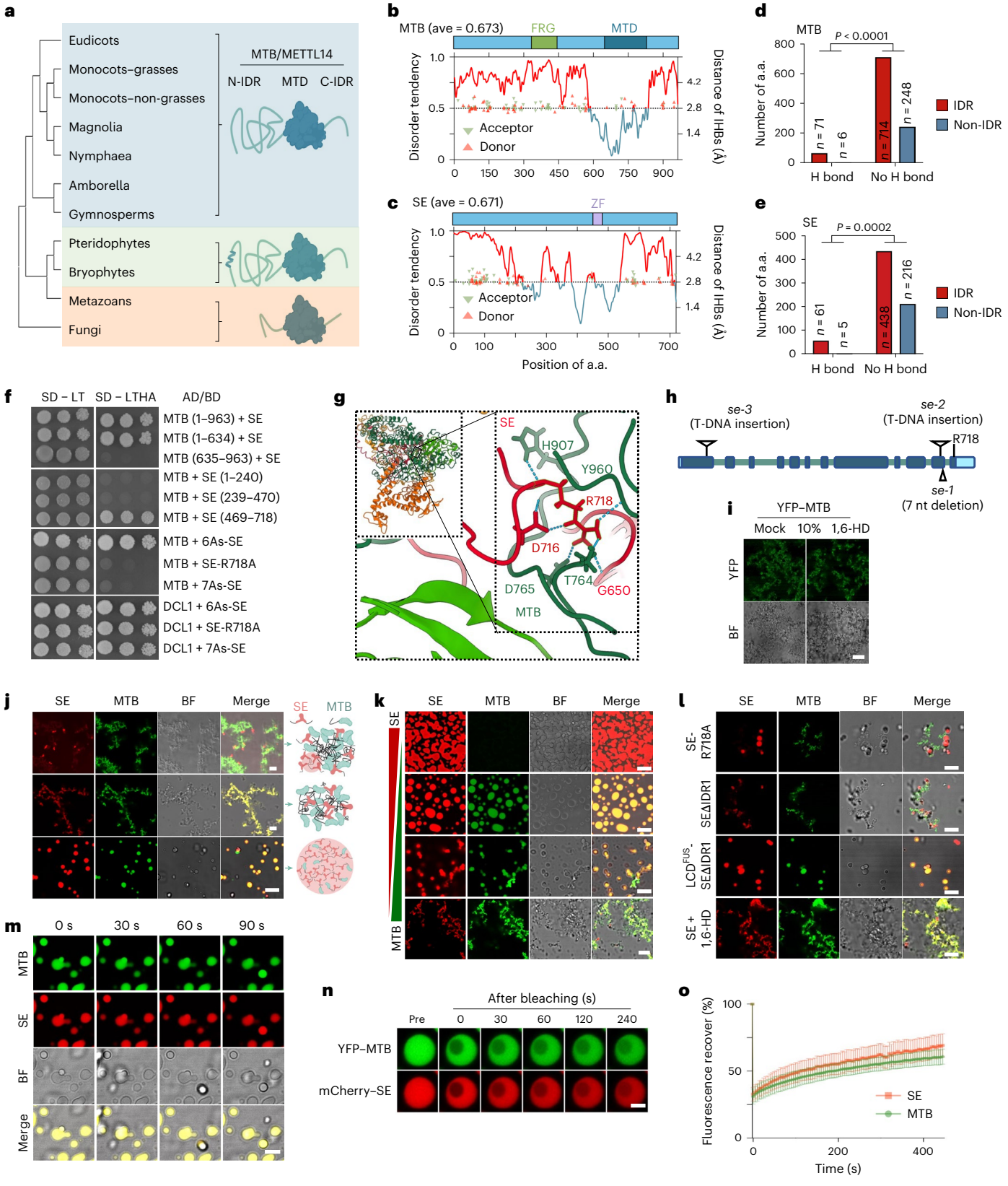

https://doi.org/10.1038/s41556-024-01530-8

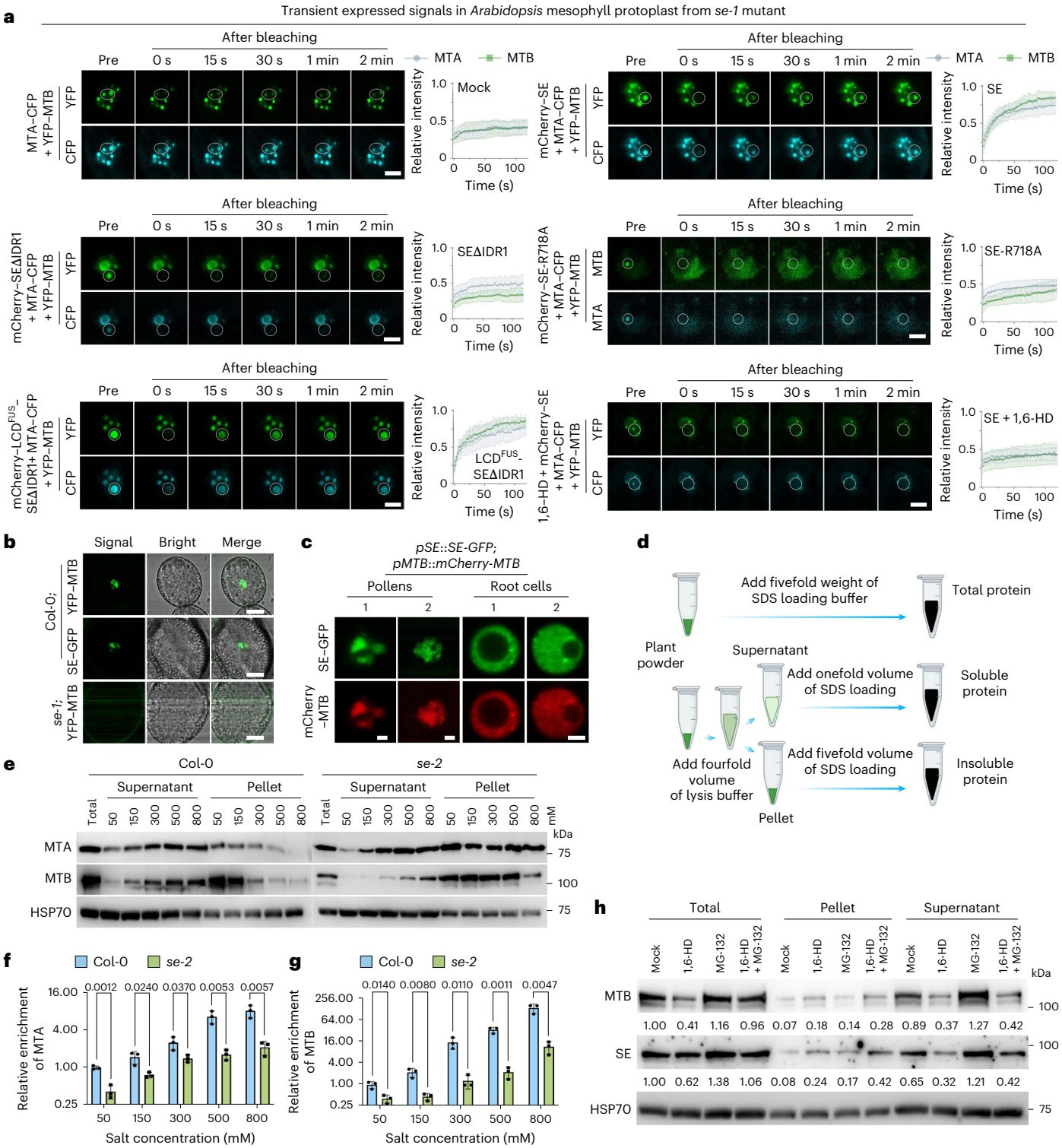

Fig. 3 | SE confers liquid-like phase behaviours to MTC in vivo. a, FRAP assays showing that transiently expressed proteins in mesophyll cells from *se-1*, supplemented with or without different forms of SE variants, display distinct phase behaviours. SE-R718A, SEΔIDR1 and LCD^{FUS}-SEΔIDR1 refer to Fig. 2l. **b**,**c**, Confocal microscopy images showing the SE-dependent MTB condensates in pollens of transgenic plants (**b**) and the SE and MTB co-condensates in both somatic cells and pollens (**c**). **d**, A schematic illustration of the protein extraction from plant powder for sedimentation assay. See Methods for a detailed description. **e**–**g**, Immunoblots (**e**) and statistical analysis of sedimentation assays demonstrate the obvious enrichments of both MTA (**f**) and MTB (**g**) proteins in the insoluble fraction from *se-2* versus Col-0. HSP70 was a loading control. The ratio was calculated as (soluble MTB/soluble HSP70)/(insoluble MTB/insoluble HSP70) and was normalized to the Col-0 value at 50 mM salt concentration, which is set to 1. *P* values at the salt concentrations of 50, 150, 300, 500 and 800 mM for MTA (**f**) are 0.0012, 0.024, 0.037, 0.0053 and 0.0057, and for MTB (**g**) are 0.014, 0.0080, 0.011, 0.0011 and 0.0047, respectively (unpaired two-sided *t*-test). **h**, Immunoblots detect the protein solubility upon chemical treatments. Ten-day-old seedlings were used. Note that both 1,6-HD and co-supply of 1,6-HD and MG-132 triggered the transition of the SE and MTB complex from a soluble form to aggregates, compared with mock and MG-132 treatment, respectively. Data are mean ± s.d. of eight (**a**) and three (**f** and **g**) independent experiments. At least eight independent protoplasts and cells were used (**a**–**c**) or three independent experiments were performed (**e** and **h**), and representative images are shown. Scale bars 5 µm (**a** and **b**) and 2.5 µm (**c**).

signal intensity became weaker and the condensates disappeared when crossed into *se-1* (Fig. 2b and Extended Data Fig. 6f,g), indicative of SE-driven formation of MTC droplets in plants. Hence, SE was also able to confer liquid-like properties to MTC in vivo.

MTC exhibits SE-dependent soluble condensates in plants

To further study the impact of SE on the physical status of MTC, we evaluated the solubility of MTC in Col-0 and *se-2* plants by sedimentation analysis. In the assays, soluble proteins were prepared using lysis buffers containing a potent detergent and varying salt concentrations, while the resulting pellet after centrifugation, reflecting the insoluble protein fraction, was resuspended with SDS loading buffer (Fig. 3d). Western blot analysis revealed that MTB, along with MTA but to a lesser extent, was significantly enriched in the insoluble fraction of *se-2* versus Col-0 (Fig. 3e–g). Meanwhile, the levels of both soluble MTA and MTB were reduced more significantly in the null-allele *se-3* (Extended Data Fig. 6h). Slightly different from the scenario in the adult plants (Extended Data Fig. 2c), the *MTB* mRNA level, and resultant protein amount, slightly increased in young seedling of *se-2* versus Col-0 (Extended Data Fig. 6i). Despite this, the ratio of the soluble fraction versus the one in insoluble pellet remained decreased in the *se-2* versus Col-0 (Extended Data Fig. 6j). To further clarify whether liquid-like properties were required for their solubility, we conducted 1,6-HD treatment before protein extraction and found that both MTB and SE condensed into the pellets. We noticed that total proteins of SE and MTB were reduced after 1,6-HD treatment and this reduction could be restored by co-supply of MG-132, in which the soluble protein contents were still decreased while it became enriched in the pellet fraction (Fig. 3h). Collectively, these results suggest that SE-driven liquid-like phase behaviours of MTC are critical for the protein solubility in plants.

SE facilitates m^{6}A deposition

Since LLPS could mediate the exchange of molecules with the surrounding milieu, we hypothesized that SE modulation of MTA/MTB condensates might impact the incorporation of RNA in the complex. To test this, we introduced Cy5-labelled RNA into a mixture of SE droplets and protein solutions of MTC. We observed that the fluorescence signal of condensates, encompassing a tripartite protein ensemble in a spherical shape along with the RNA, exhibited substantial overlap (Fig. 4a). In contrast, when we treated the protein mixture with 1,6-HD before the supply of RNA, the displayed signals only partially overlapped (Fig. 4a), implying that RNA lingered on the surface of irregular-shaped condensates in vitro. Meanwhile, we immunoprecipitated MTA from nuclear fractions and found that the enrichment of MTC-bound RNAs was reduced in *se-2* versus Col-0 (Fig. 4b). These results indicate that SE promotes RNA incorporation into MTC condensates. The prediction from this model would be that the compromised loading of RNA into MTC caused by the loss of SE might inhibit the MTC enzymatic activity. To test this, we conducted in vitro methylation assays with or without SE or its variants. After the reaction, we removed proteins and enriched methylated RNAs using an anti-m^{6}A antibody, followed by P^{32} labelling and autographic imaging. Indeed, SE and LCD^{FUS}-SEΔIDR1 caused a significant increase in MTC activity, whereas SE-R718A and SEΔIDR1 had minimal effect, compared with controls (Fig. 4c,d). Altogether, we concluded that SE could modulate the phase behaviours of MTC to facilitate m^{6}A deposition.

Co-condensates mutually stabilizes each other in plants

Since MG-132 restored both MTB and SE from 1,6-HD-induced protein reduction, we next studied how protein stabilities were regulated. Upon the treatment of cycloheximide, an inhibitor of protein synthesis, MTB had a much shorter half-life in *se-1* versus Col-0, and the half-life was clearly extended in the presence of MG-132 in the two backgrounds (Fig. 4e and Extended Data Fig. 7a). Notably, the half-life of MTB in Col-0 could be slightly extended by PYR-41, an inhibitor specific for E1 enzyme for the 26S proteasome pathway[16], whereas this effect was not detected in *se-1* (Fig. 4e and Extended Data Fig. 7a). These results suggested that the IDP MTB might be subjected to destruction via 20S proteasome, and this regulation became obvious in *se-1* versus Col-0. Next, we performed cell-free protein decay assays with recombinant MTB protein. Again, glutathione S-transferase (GST)–His–MTB was quickly degraded when incubated with the cell lysate derived from *se*-2 compared with that of Col-0, and this degradation was substantially blocked by MG-132 (Extended Data Fig. 7b,c). Furthermore, poly-ubiquitinated MTB conjugates were undetectable compared with DMS3, a control degraded by the 26S proteasome[35] (Fig. 4f,g). Thus, SE might stabilize MTB from 20S proteasome-mediated degradation. Further supporting this idea was that MTB could directly bind to three 20S proteasome subunits: a structural subunit, PAG1 and two proteolytically active subunits, PBE1 and PBE2 (Fig. 4h and Extended Data Fig. 7d,e).

We next performed in vitro 20S proteasome reconstitution assays[16]. Indeed, MTB was degraded by 20S proteasome and this process was hindered by MG-132 (Fig. 4i,k). Interestingly, pre-incubation of MTB and SE before the addition of the 20S proteasome could significantly stabilize both MTB and SE concordantly (Fig. 4i–l). Of note, the co-stabilization effect was also sustained by pre-incubation of LCD^{FUS}-SEΔIDR1, but only weakly by SE-R718A and SEΔIDR1 (Fig. 4i–l). In line with these results, MTB protein was accumulated in *pag1* and *pbe1* versus Col-0 (Fig. 4k–m and Extended Data Fig. 7f), reminiscent of SE accumulation in 20S mutants[16]. These results indicate

Fig. 4 | The SE-dependent phase behaviour of MTC is critical for its enzymatic activity and protein stability. a, Confocal microscopy examining the incorporation of proteins and RNA into condensates in vitro without (top) or with (bottom) 10% 1,6-HD. Scale bars, 5 µm (top) and 1 µm (bottom). **b**, MTA RIP qPCR showing the decreased association between MTC and RNA in *se-2* versus Col-0. IPs were conducted with the nuclear fraction using an anti-MTA antibody. *P* values at the indicated loci are 0.036, 0.021, 0.00071, 0.085, 0.0029, 0.0033, 0.0028 and 0.46, respectively. **c**,**d**, In vitro m^{6}A methylation assays (**c**) and their statistical analysis (**d**). *P* values for indicated treatments versus MTA + MTB are <0.0001, 0.99, 0.93, <0.0001 and 0.99, respectively. **e**, MTB shows a shorter half-life in *se-1* versus Col-0, and the decay rate was hindered by MG-132 but not by PYR-41 or DMSO. The *P* value for Col-0 (PYR-41 versus DMSO) is 0.64, and the *P* values for the other treatments versus Col-0 (DMSO) are <0.0001. **f**,**g**, Immunoblot assays of indicated immunoprecipitates did not detect poly(Ubi)-conjugated forms of MTB in planta. IPs were conducted using anti-MTB-conjugated (**f**) or GFP-trap beads (**g**). IgG-IP used as a negative control. Immunoblots were performed with the indicated antibodies. **h**, Y2H assays showing the interactions between MTB and 20S proteasome subunits. Refer to Fig.1c for the legend. **i**–**l**, The quantitive analysis of decay rates (for MTB (**i**) and for SE and variants (**j**)) and immunoblots (for MTB (**k**) and SE and variants (**l**)) of 20S proteasome reconstitution assays shows that pre-incubation of MTB with mCherry-tagged SE and LCD^{FUS}-SEΔIDR1, but not SEΔIDR1 or SE-R718A, could mutually protect each other from degradation. The notations inside and outside the brackets represent detected and co-incubated proteins, respectively. In **i**, the *P* values for MTB (SEΔIDR1) and MTB (SE-R718A) versus MTB (DMSO) are 0.0003 and 0.0016, respectively, and are <0.0001 for the rest of the comparisons. In **j**, the *P* values for SE (MTB), LCD^{FUS}-SEΔIDR1 (MTB), SE-R718A (MTB), SEΔIDR1 (MTB), SEΔIDR1 (mock), SE-R718A (mock) and SE (mock) versus LCD^{FUS}-SEΔIDR1 (mock) are <0.0001, <0.0001, 0.82, 1.00, 0.018, 0.033 and 0.0010, respectively. **m**,**n**, Immunoblots showing that MTB accumulates in *pag1-2* (**m**) and *pbe1* (**n**) versus Col-0, where the amount was arbitrarily assigned a value of 1. MTB was detected with endogenous protein antibodies. HSP70 was an internal control. For **c**, **d** and **i**–**l**, SE-R718A, SEΔIDR1 and LCD^{FUS}-SEΔIDR1 refer to Fig. 2l. Data are mean ± s.d. of three independent experiments in **b**, **e**, **i** and **j**. At least three independent experiments were performed in **a**, **c**, **f**, **g** and **k**–**n**, and ten colonies were detected in **h**, with representative images shown. *P* values are from an unpaired two-sided *t*-test (**b**) and one-way ANOVA analysis with Tukey's multiple comparisons test (**d**, **e**, **i** and **j**). Only the comparisons with significance (**d**) and the Col-0 (DMSO) (**e**), MTB (DMSO) (**i**) and LCD^{FUS}-SEΔIDR1 (mock) (**j**) groups are shown. *P* values for the remaining comparisons are presented in Supplementary Table 4.

https://doi.org/10.1038/s41556-024-01530-8

that SE–MTB assembly might mutually protect each other from 20S proteasome-mediated degradation through co-condensation.

We next hypothesized that a developmental deficit of *se* might in part result from destabilization of MTC. To test this, we generated overexpression lines of *MTA* and *MTB* in Col-0. Overexpression of *MTA* led to the accumulation of both MTB and SE (Fig. 5a). However, overexpression of *MTB* only increased SE, but not MTA, suggesting that MTA might undergo an additional regulatory survey in vivo (Fig. 5a). Interestingly, once being crossed, the *se-1*; *p35S*::*Flag-MTA* could partially restore mutant developmental defects as evidenced by plant size, flowering transition and visible enrichment of truncated SE-1 (Fig. 5a–c and Extended Data Fig. 7g). In sharp contrast, overex-

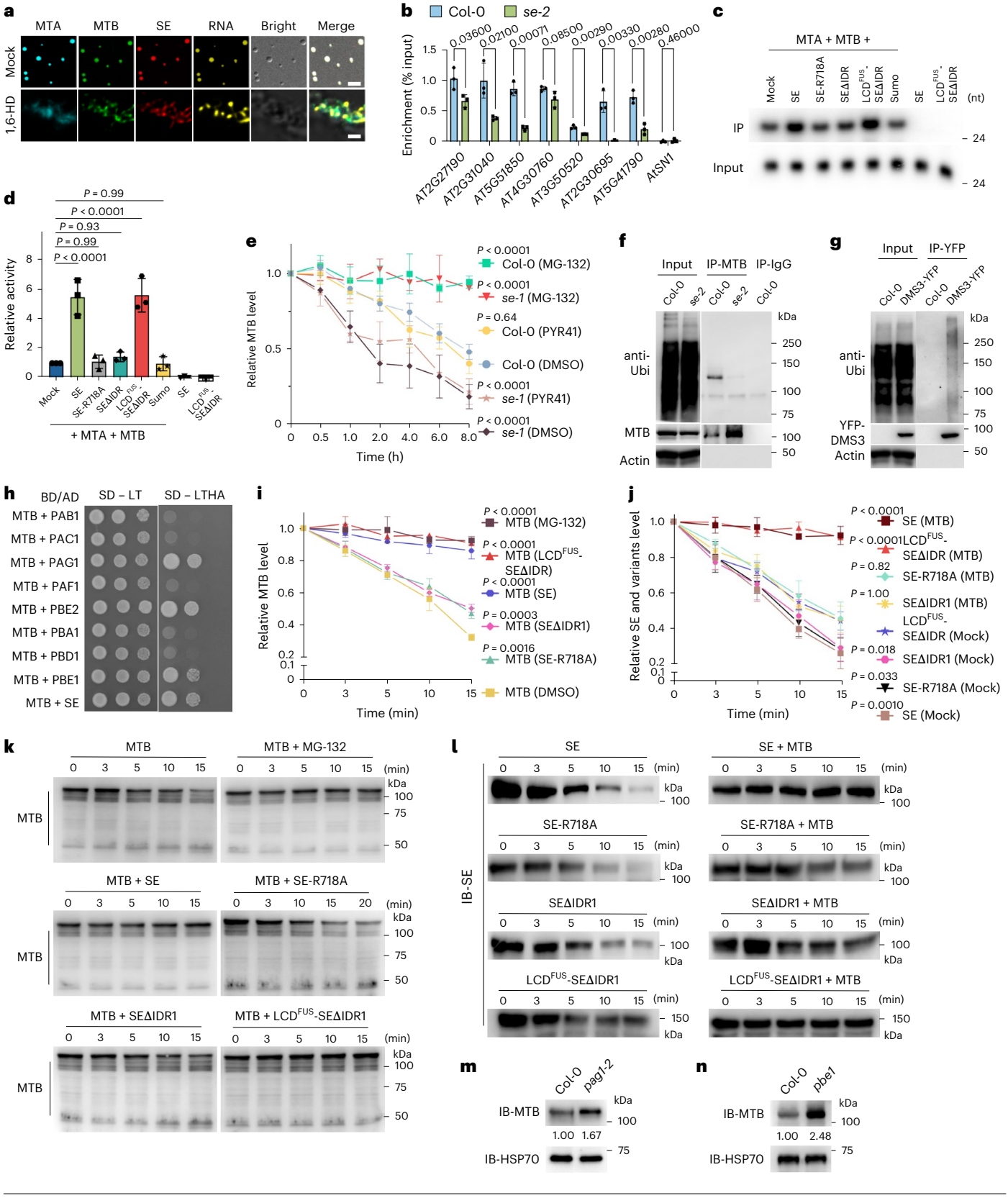

https://doi.org/10.1038/s41556-024-01530-8

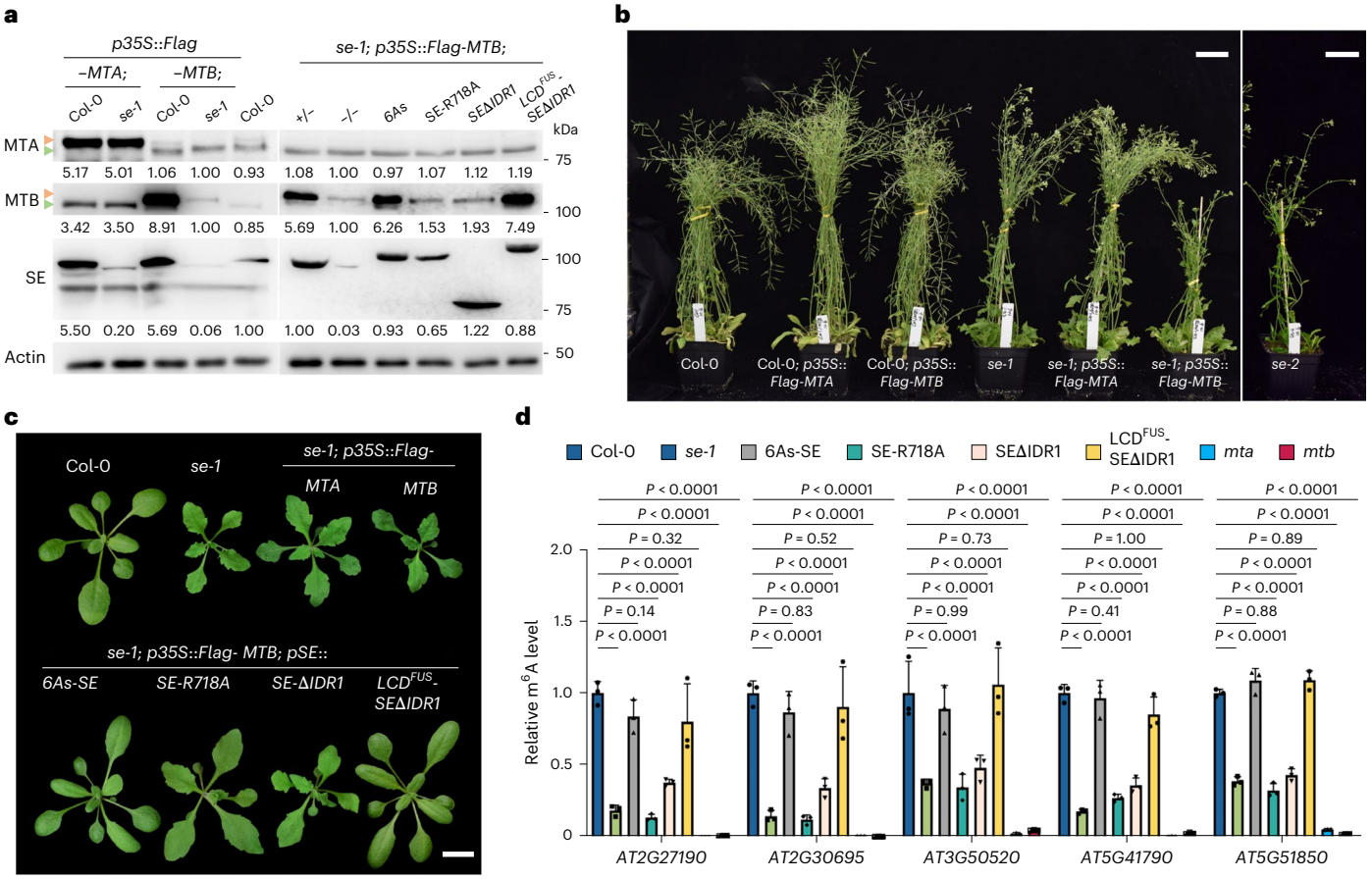

Fig. 5 | Proper phase behaviours of SE and MTB are required for protein accumulation and plant development. a–**c**, Immunoblots (**a**) and images of adult (**b**) and 3-week-old (**c**) plants indicating the importance of both SE–MTB interaction and liquid-like properties for plant development and protein accumulation in vivo. Immunoblots were performed with indicated endogenous protein antibodies. Actin was a loading control. Triangles indicate the Flag-tagged (orange) and endogenous protein (green) bands, respectively. Scale bars, 5 cm (**b**) and 2 cm (**c**). Three biological replicates of immunoblots were tested, at least ten independent transgenic lines were photographed and representative images are shown. **d**, MeRIP qPCR showing the m^{6}A levels of selected genes in different complementation plants versus Col-0. Data are mean ± s.d. of three independent experiments. *P* values for all detected genes at *se-1*, SE-R718A, SEΔIDR1, *mta* and *mtb* versus Col-0 are <0.0001; at 6As-SE versus Col-0 are 0.14, 0.83, 0.99, 0.41 and 0.88; and at LCD^{FUS}-SEΔIDR1 versus Col-0 are 0.32, 0.52, 0.73, 1.00 and 0.89, respectively, by two-way ANOVA analysis with Dunnett's multiple comparisons test.

pression of MTB could not be achieved in *se-1*, and *se-1*; *p35S*::*Flag-MTB* plants now phenocopied *se-2*, which is a more severe allele versus *se-1* (Fig. 5a–c and Extended Data Fig. 7g). These results suggested that MTB, rather than MTA, specifically the soluble portions, display SE-dependent accumulation, with a further suggestion that the *se* developmental defects were partially accredited to concurrent reduction of functional MTB.

To further investigate whether SE–MTB-regulated phenotypes entailed their interaction and condensation, we performed complementation assays of *se-1* with various SE variants. Notably, only the variants that could stabilize MTB, specifically *se-1*; *pSE*::*6As-SE* and *se-1*; *pSE*::*LCD^{FUS}-SEΔIDR1*, but not *se-1*; *pSE*::*SE-R718A* or *se-1*; *pSE*::*SEΔIDR1*, could rescue the mutant phenotype (Extended Data Fig. 7h). Consistent with the morphological changes, the m^{6}A modification exhibited reduced levels in the *se-1*; *pSE*::*SE-R718A* and *se-1*; *pSE*::*SEΔIDR1* hypomorphs versus WT and *se-1*; *pSE*::*6As-SE* and *se-1*; *pSE*::*LCD^{FUS}-SEΔIDR1* lines, albeit to a lesser extent, compared to the amount in *mta* and *mtb* mutants (Fig. 5d). Additionally, only 6As-SE and LCD^{FUS}-SEΔIDR1 could accumulate MTB upon introducing into *se-1*; *p35S*::*Flag-MTB* (Fig. 5a,b). These results suggest that liquid-like phase behaviours of the SE–MTB complex could shield the proteins from 20S proteasome-mediated degradation, thereby being critical for their functionality in plants. Altogether, we conclude that SE and MTC form liquid-like co-condensates and through this, SE maintains the solubility of MTC, promoting MTC enzymatic activity and protein stabilization.

Methylation promotes pri-miRNA processing in *Arabidopsis*

It has been reported that m^{6}A positively regulates pri-miRNA processing[22–25], but the underlying mechanism remains unclear. Next, we hypothesized that the SE–MTB interaction might impact m^{6}A modification on pri-miRNAs. To test this, we first pinpointed methylation sites of pri-miRNAs. Despite a general decline in the m^{6}A epitranscriptome in *se-2*, the majority of methylation remained discernible (Fig. 1d). Taking advantage of highly accumulated defectively processed pri-miRNAs, we relaxed the peak calling stringency using a moderate threshold as $\log_2$(enrichment) >0 and $P < 0.05$, and through this, 79 candidates from 127 detected pri-miRNAs were identified (Fig. 6a, Extended Data Fig. 8a and Supplementary Table 5). In parallel, an independent approach[36] using a sliding window algorithm of 25 nucleotides was applied. The m^{6}A enrichment for each window was normalized using the median coverages of the corresponding genes for both immunoprecipitation (IP) and input. This analysis yielded 83 methylated pri-miRNAs (Supplementary Table 5), with 71 shared in both algorithms (Fig. 6a). Indeed, Integrative Genomics Viewer (IGV) files revealed that the reads in IP samples exhibited clear enrichments that were distinct from the patterns in inputs (Fig. 6b). To further validate this, we conducted

MeRIP quantitative PCR (qPCR) assays using the mixture of full-length poly(A)+ mRNA and two standards. Consistently, pri-miRNAs detected were enriched in IP samples, but their methylation levels significantly decreased in *se-2* and *mta* compared with Col-0 (Fig. 6c). In contrast, the enrichment of methylated spikes was increased in the mutants (Extended Data Fig. 8b). We further explored the distribution of m^{6}A on pri-miRNAs and found that methylation was predominantly deposited onto the ss basal regions (Fig. 6d). Thus, SE also contributed to m^{6}A methylation on pri-miRNAs mediated by MTC.

We found that the accumulation of miRNAs was significantly reduced in MTC mutants versus Col-0 (Extended Data Fig. 8c,d and Supplementary Table 6). The reduction was more pronounced in miRNAs derived from methylated pri-miRNAs compared with others (Fig. 6e). In line with these results, the expression of miRNA targets was significantly increased (Extended Data Fig. 8e). The decrease in miRNA accumulation was probably attributable to a deficit in post-transcriptional processing of pri-miRNAs, as pri-miRNAs were accumulated (Extended Data Fig. 8f) whereas no obvious defects of *MIRNA* transcription, splicing of intron-containing pri-miRNAs or expression of tested miRNA pathway components were detected in *mta* versus Col-0 (Extended Data Fig. 8g–j). Taken together, we pinpointed m^{6}A loci on most pri-miRNAs and uncovered a positive regulatory role of writers in miRNA production.

MTC involved in co-transcriptional processing of pri-miRNAs

Since both m^{6}A deposition and the initial processing of pri-miRNAs take place co-transcriptionally, we next accessed published SE chromatin IP sequencing (ChIP-seq)[37] and found that SE is preferably recruited to the loci generating methylated pri-miRNAs (Extended Data Fig. 9a). Thus, we hypothesized that MTC might contribute to co-transcriptional processing of pri-miRNAs. To test this, we performed ChIP qPCR using *MTA* isogenic transgenic plants in which the protein levels of MTC components are comparable in Col-0 and *se-1*. The results showed that MTA could be recruited to *MIRNA* loci in Col-0 and the enrichment was even increased in the absence of SE, suggestive of MTA retention onto chromatin in *se-1* versus Col-0 (Fig. 6f). Conversely, the recruitment of SE to the loci was compromised in *mta* and *mtb* (Fig. 6g), indicating that SE association with the m^{6}A-conferring loci depends on MTC in this context.

To determine whether MTC could handover pri-miRNAs to the microprocessor, we investigated the binding affinity of MTC to pri-miRNAs. The electrophoretic mobility shift assay (EMSA) showed a very weak RNA association with FIP37, an MTC component (Extended Data Fig. 9b). Differently, MTA and MTB both had robust RNA-binding abilities with respective K_d values of 3.95 (±1.92) nM (Fig. 6h,i) and 1.92 (±0.77) nM (Fig. 6j,k), but the affinities were relatively weaker than that of HYL1, which has two double-stranded RNA-binding domains and a much stronger RNA affinity, with a K_d value of 0.74 (±0.16) nM (ref. 38). Consistently, HYL1 could effectively absorb RNAs from MTA and MTB in competition binding assays (Fig. 6l,m). Notably, HYL1 association of pri-miRNAs is reduced in *mta*[23], indicating that MTC might deliver pri-miRNAs to HYL1. Next, we performed Histone 3 RNP complex IP assays (H3-RIP) to examine the chromatin retention of nascent or partially processed pri-miRNAs[39]. H3-RIP qPCR showed that the aberrant accumulation of full-length pri-miRNAs rather than partially processed intermediates was detected in H3-RIP from the MTC mutants versus Col-0 (Fig. 6n and Extended Data Fig. 9c–e). Thus, these results suggest that MTC could recruit the microprocessor to *MIRNA* loci through MTB–SE interaction, and then convey pri-miRNAs to the machinery for initial processing.

M^{6}A readers affect pri-miRNA processing

Pri-miRNA processing also occurs in the nucleoplasm[39]. We found that pri-miRNAs were accumulated in the nucleoplasm of *mta* versus those of Col-0, suggestive of a critical role m^{6}A in pri-miRNA processing (Fig. 7a). A series of m^{6}A readers, evolutionarily conserved C-terminal region (ECT)1–3, ECT5 and cleavage and polyadenylation specificity factor 30 (CPSF30), were recovered from a proteomic assay of SE immunoprecipitates[40] (Extended Data Fig. 10a). Among YTH (YT521-B homology) domain-containing proteins, *ECT2* is the most abundantly expressed gene throughout various developmental stages and tissues (Extended Data Fig. 10b). Earlier confocal microscope imaging suggested the predominant presence of ECT2 in the cytoplasm and an observable amount in the nucleus[41,42]. To clarify this, we conducted a nucleus–cytoplasm fraction assay and found that ECT2 could indeed be detected in the nucleus fraction (Fig. 7b). Furthermore, ECT2 were readily detected in the nucleus upon leptomycin B treatment, a chemical that blocks protein trafficking from the nucleus to the cytoplasm (Fig. 7c,d). These results suggested that ECT2 could perform some unexplored functions in the nucleus. Indeed, Y2H and co-IP experiments showed that ECT2 could associate with the microprocessor through SE (Fig. 7e and Extended Data Fig. 10c). Importantly, the majority of tested miRNAs were reduced, coupled with an accumulation of some pri-miRNAs in *ect2; ect3; ect4* versus Col-0 (Fig. 7f and Extended Data Fig. 10d). These results further suggested that m^{6}A might be an essential marker for effective processing of pri-miRNAs.

To further study how the m^{6}A reader ECT2 contributed to pri-miRNA processing, we detected its binding affinity to different

Fig. 6 | MTC facilitates miRNA biogenesis via m^{6}A-dependent and m^{6}A-independent means. a, Exomepeak2 and winscore algorithms identified largely overlapping methylated pri-miRNAs in *se-2*. **b**, IGV files of the selected methylated pri-miRNAs in *se-2*. The dark blue colour region within the light blue horizontal line represents the pre-miRNA within the pri-miRNA. The *x* axis shows chromosomal locations, and the *y* axis shows normalized reads. Chr, chromosome. **c**, MeRIP RT–qPCR assays validated the reduction of m^{6}A levels on pri-miRNAs in *se-2* and *mta* versus Col-0. The *P* value for *se-2* versus Col-0 at *pri-miR172B* is 0.0032 and *P* values are <0.0001 for other comparisons. **d**, A metagene profile portraying the average m^{6}A distribution across pri-miRNAs. The *x* axis shows the relative position, and the *y* axis shows m^{6}A abundance. The dark blue colour region within the light horizontal line represents the pre-miRNA within the pri-miRNA. **e**, A violin plot illustrating that the levels of miRNAs derived from methylated pri-miRNAs were significantly reduced versus those derived from unmethylated pri-miRNAs in mutants versus Col-0. The lines represent the median and quartiles. *P* values for m^{6}A(−) versus m^{6}A(+) at *se-2* and *mta* are <0.0001 and 0.13, respectively. **f**,**g**, ChIP qPCR assays show that MTA and MTB acted upstream of SE in tested *MIRNA* loci. ChIP assays were performed with anti-Flag (**f**) and anti-SE (**g**) antibodies. In **f**, the *P* values for Col-0; *Flag-MTB* and *se-1*; *Flag-MTA* versus Col-0; *Flag-MTA* at *MIR156A* are 0.084 and 0.0001; at *MIR156C* are 1.00 and <0.0001; at *MIR162A* are 0.070 and 0.026; at *MIR166A* are 0.56 and 0.0022; at *MIR171C* are 0.47 and <0.0001; and at *MIR172B* are 0.053 and <0.0001, respectively. In **g**, the *P* values for *mta* and *mtb* versus Col-0 are 0.0005 and 0.0022, for *se-2* versus Col-0 at *MIR162A* is 0.0014 and for the rest comparisons are <0.0001. **h**–**k**, EMSA assays (for MTA (**h**) and MTB (**j**)) and the binding curves (for MTA (**i**) and MTB (**k**)) show that MTA and MTB possess strong binding affinities to structured pri-miRNAs. **l**,**m**, EMSA assays show that HYL1 could sequester structured pri-miRNA from MTA (**l**) and MTB (**m**). The numbers on top of gels indicated the amount of recombinant HYL1 (nM) added to 20 nM MTA and MTB. **n**, H3-RIP qPCR assays show the increased retention of stem-loop fragments of tested pri-miRNAs along *MIRNA* loci in the mutants versus Col-0. A, B and C refer to 5′′ flanking, pre-miRNA and 3′ flanking sequences of pri-miRNA, respectively. *P* values for A versus B, B versus C and A versus C at Col-0 are 0.038, 0.014 and 0.99; at *mta* are 0.98, 0.99 and 0.99; at *mtb* are 0.80, 0.99 and 0.76; at *se-2* are 0.86, 0.93 and 0.99; and at IgG control are 0.99, 0.61 and 0.83, respectively. Data are mean ± s.d. of three independent experiments in **c**, **f**, **g**, **i**, **k** and **n**. At least three independent experiments were performed, and representative images are shown in **h**, **j**, **l** and **m**. *P* values are from unpaired two-sided *t*-tests (**e**) and two-way ANOVA analysis with Dunnett's (**c**, **f** and **g**) or Tukey's (**n**) multiple comparisons test.

https://doi.org/10.1038/s41556-024-01530-8

types of RNAs. Purified ECT2 had a strong propensity to bind to methylated ssRNAs, but not to unmethylated ssRNAs (Fig. 7g and Extended Data Fig. 10e,f, top). Moreover, W521A mutation abolished the association of ECT2 with the methylated ssRNAs (Extended Data Fig. 10e,g, top), indicative of the binding's reliance on the m^{6}A group, as observed previously[42]. Then, we generated structured RNAs with or without m^{6}A (Fig. 7h and Extended Data Fig. 10h). Remarkably, we found that ECT2 could bind structured RNAs in an m^{6}A-independent manner, with a moderate K_d of 35.09 (±2.34) nM (Fig. 7i, left, and Extended Data Fig. 10i). However, the presence of m^{6}A could booster the association

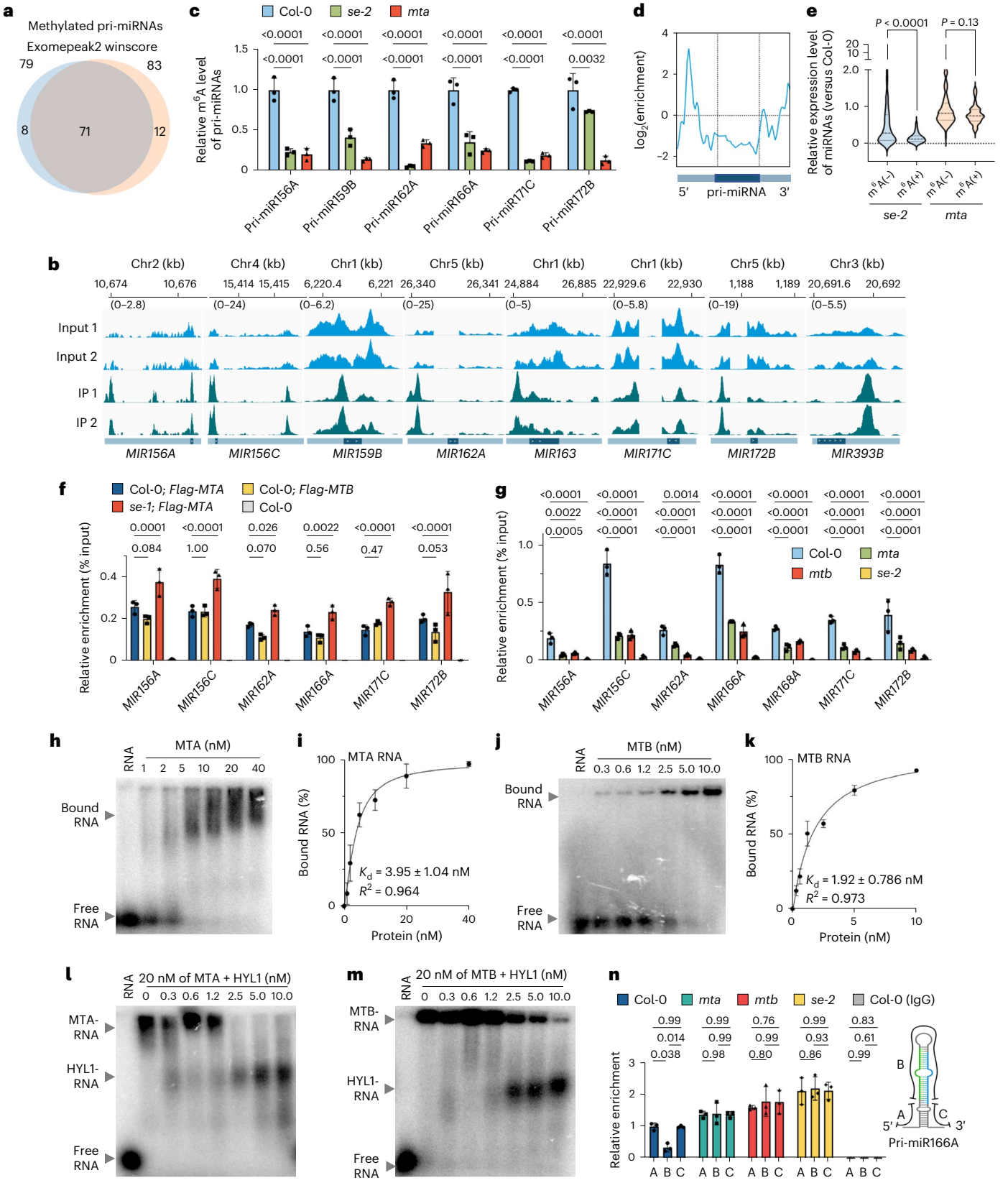

https://doi.org/10.1038/s41556-024-01530-8

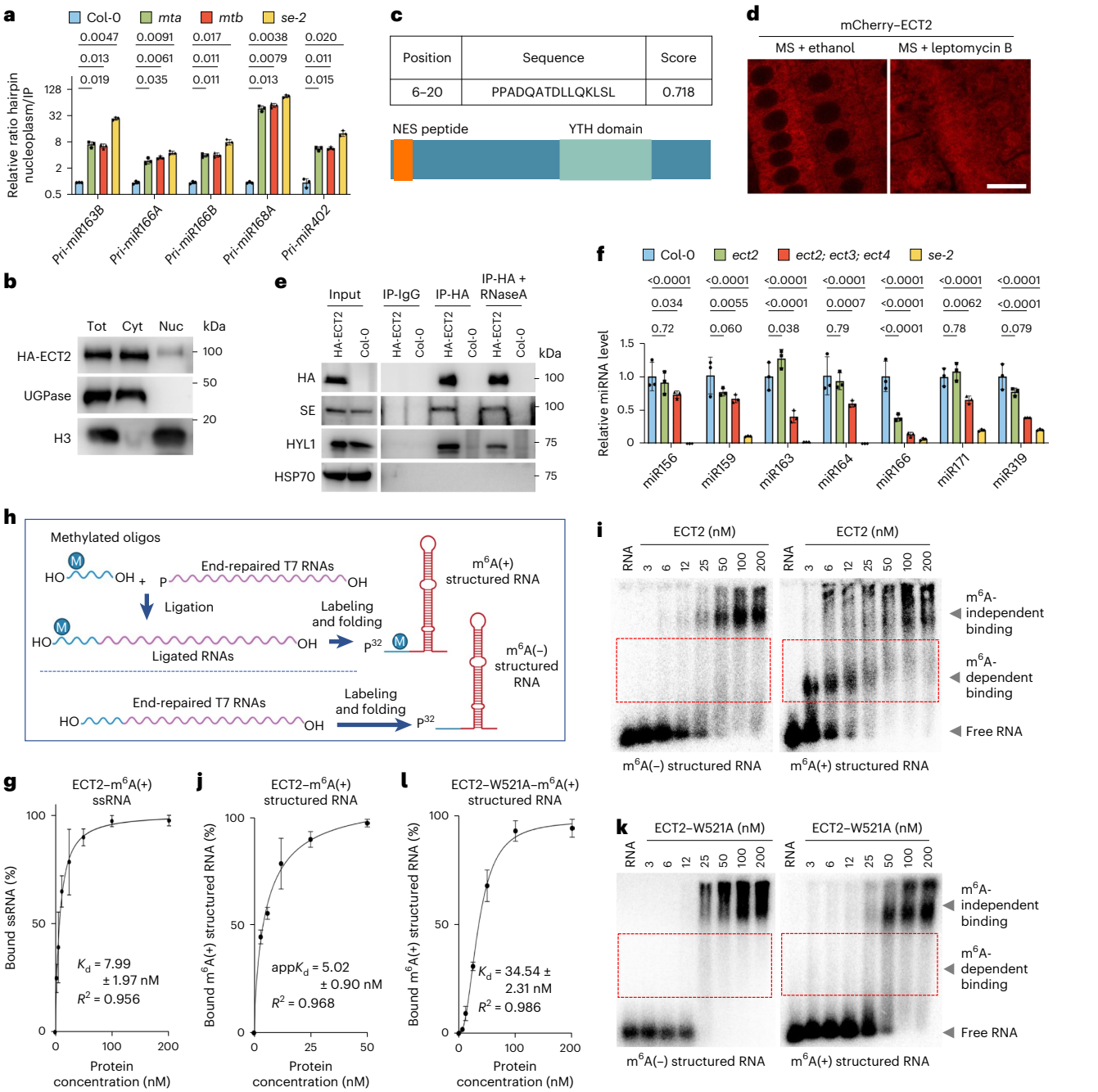

Fig. 7 | The m^{6}A readers promote pri-miRNA processing. a, RT–qPCR assays detected the accumulation of tested pri-miRNAs in the nucleoplasm fraction of m^{6}A writer mutants versus Col-0. *UBQ10* was an internal control for normalization. *P* values for *mta*, *mtb* and *se-2* versus Col-0 at *pri-miR163B* are 0.019, 0.013 and 0.0047; at *pri-miR166A* are 0.035, 0.0061 and 0.0091; at *pri-miR166B* are 0.011, 0.011 and 0.017; at *pri-miR168A* are 0.013, 0.0079 and 0.0038; and at *pri-miR402* are 0.015, 0.011 and 0.020, respectively. **b**, Immunoblots of fractionation assays using 3-week-old *pECT2*::*3xHA-ECT2* plants. ECT2 was detected by an anti-HA antibody. UDP–glucose pyrophosphorylase (UGPase) and Histone 3 (H3) were used as cytoplasmic (Cyt) and nuclear (Nuc) markers, respectively. Tot, total extraction. **c**, The predicted CRM1 (exportin 1)-dependent nuclear export signal (NES) peptide in ECT2. **d**, Microscopic images show the nuclear localization of ECT2–mCherry signals in 5-d-old transgenic plants upon CRM1 inhibitor leptomycin B treatment. Ethanol was a negative control. Scale bar, 10 µm. **e**, Co-IP assays validated the interaction between ECT2 and microprocessor key components. IPs were conducted with *pECT2*::*3xHA-ECT2* plants using HA antibodies. Immunoblots were detected with the indicated antibodies. HSP70 was a negative control. **f**, RT–qPCR assays show the decreased levels of tested miRNAs in m^{6}A reader mutants versus Col-0, with *se-2* serving as a control. U6 was used as an internal control for normalization. *P* values for *ect2* and *ect2; ect3; ect4* versus Col-0 at miR156 are 0.72 and 0.034; at miR159 are 0.060 and 0.0055; at miR163 are 0.038 and <0.0001; at miR164 are 0.79 and 0.0007; at miR166 are both <0.0001; at miR171 are 0.78 and 0.0062; and at miR319 are 0.079 and <0.0001, respectively. *P* values for *se-2* versus Col-0 are <0.0001 at all detected miRNAs. **g**, The binding curve of the affinity of ECT2 to m^{6}A(+) ssRNA. **h**, A schematic illustration of the strategy to synthesize m^{6}A-modified structured RNAs. T7 in vitro transcribed RNA was used for end repair, followed by ligation to a methylated oligonucleotide. The products were labelled with P^{32} and purified before in vitro folding. An unmethylated control was also synthesized using T7 in vitro transcription with an identical sequence. **i**–**l**, EMSA assays (for ECT2 (**i**) and ECT2-W521A (**k**)) and their binding curves (for ECT2 (**j**) and ECT2-W521A (**l**)) show that ECT2 and ECT2-W521A, a variant lacking of m^{6}A recognition, both possessed a binding affinity to m^{6}A(–) structured pri-miRNAs and the binding affinity stimulated by the presence of m^{6}A on RNAs could only be found by ECT2. App, apparent. Data are mean ± s.d. of three independent experiments in **a**, **f**, **g**, **j** and **l**. At least three independent experiments were performed, and representative images are shown in **b**, **d**, **e**, **i** and **k**. *P* values are from two-way ANOVA analysis with Dunnett's multiple comparisons test (**a** and **f**).

https://doi.org/10.1038/s41556-024-01530-8

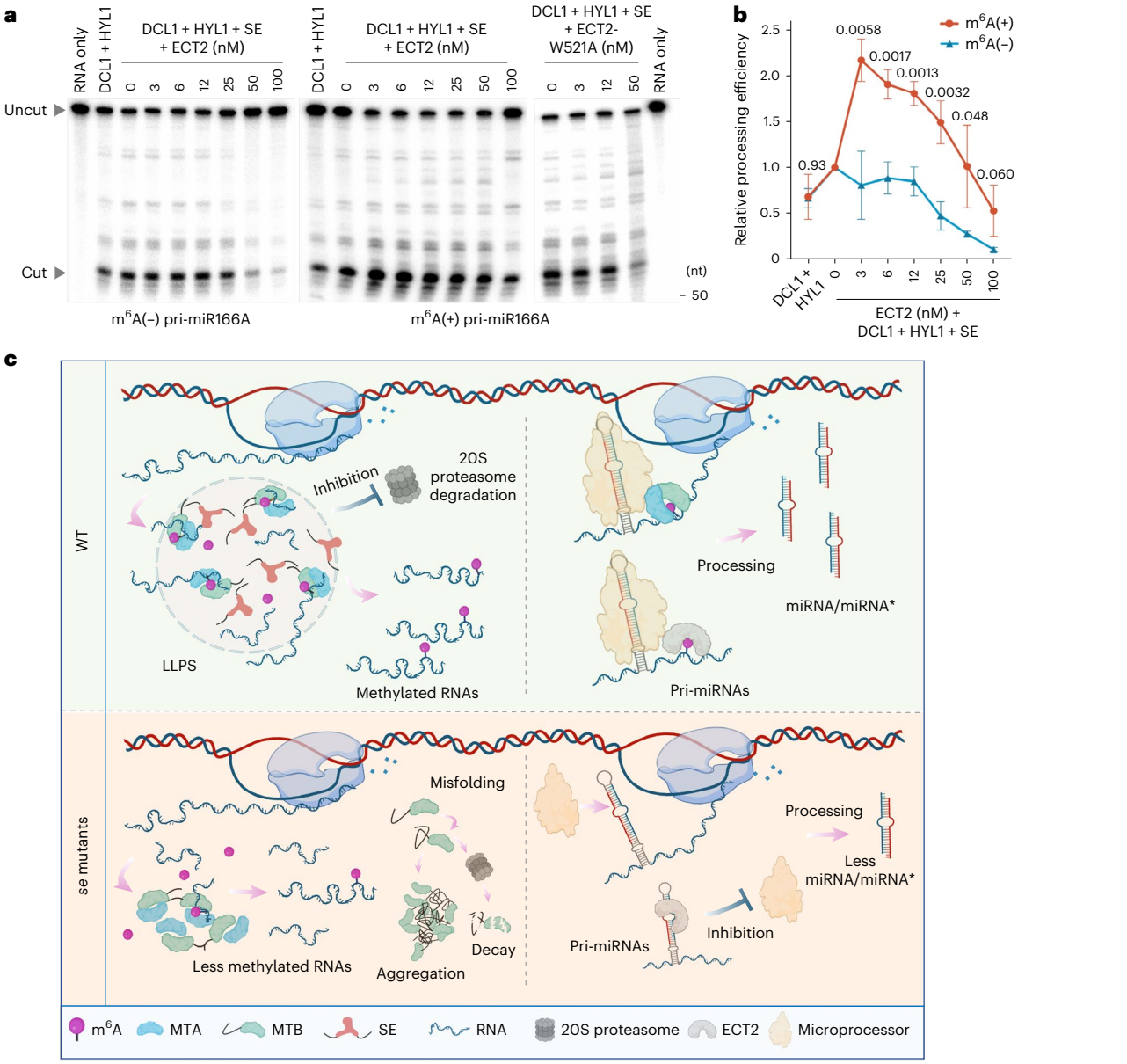

Fig. 8 | m^{6}A modification promotes miRNA production in in vitro microprocessor reconstitution assays and a proposed model for reciprocal regulation of m^{6}A modification and miRNA production machineries. **a**,**b**, In vitro microprocessor assays (**a**) and statistical analysis (**b**) of processing efficiency showed that appropriate concentrations of ECT2 were essential for effective promotion of the processing of m^{6}A-harboured pri-miRNAs compared with their m^{6}A-depleted counterparts. Data are mean ± s.d. of three independent experiments performed, and representative images are shown. The *P* value for m^{6}A(+) versus m^{6}A(−) without ECT2 is 0.93, and with SE and 3, 6, 12, 25, 50 and 100 nM of ECT2 are 0.0058, 0.0017, 0.0013, 0.0032, 0.048 and 0.060, respectively. **c**, A proposed model of cross-regulation between m^{6}A modification and miRNA production machineries. Top left: MTB can co-condense with SE droplets, thereby maintaining solubility and enzymatic activity in a WT condition. Bottom left: MTB may undergo misfolding, leading to either aggregation or degradation in *se* mutants. Top right: MTC can reciprocally recruit microprocessor to *MIRNA* loci to engage in co-transcriptional processing of pri-miRNAs. Concurrently, the readers interact with both the basal or flanking region of methylated pri-miRNAs and microprocessor to facilitate processing. Bottom right: the absence of writers results in the impairment of both co-transcriptional processing and methylation of pri-miRNAs. Additionally, readers occupy structural regions within pri-miRNAs, consequently obstructing downstream processing events.

of ECT2 with the structured RNAs, with a K_d of 5.05 (±0.92) nM, which is equivalent to or slightly lower than that of the strong RNA-binding protein HYL1 (ref. 38) (Fig. 7i, right and j). Such high affinity would enable ECT2 to recognize and pool substrates at a much lower concentration. On the other hand, the removal of putative ECT2 target motif UYUYU[42,43] exhibited a slight reduction in RNA affinity (Extended Data Fig. 10f, bottom, and j). Consistently, W521A did not impact ECT2 binding of structured RNA but erased its binding with the m^{6}A-dependent portion (Fig. 7k,l and Extended Data Fig. 10g, bottom and k,l), indicating that the ECT2 association of structured RNA is independent of m^{6}A modification. Together, our results indicate that ECT2 had a stronger binding affinity to m^{6}A-harboured ss segments of pri-miRNAs, while also associated with the structured regions of pri-miRNAs but with a relatively weaker affinity in an m^{6}A recognition-independent manner.

Finally, we assessed the impact of two-pronged RNA-binding capacity of ECT2 on pri-miRNA processing. In vitro microprocessor reconstitution assays showed that the processing efficiency of methylated and unmethylated pri-miRNAs was comparable in the absence of ECT2 (Fig. 8a,b and Extended Data Fig. 10m), suggesting that the

physical feature of m^{6}A itself could not promote microprocessor activity in pri-miRNA processing. Next, we pre-incubated pri-miRNAs with a gradient dosage of ECT2 before microprocessor assays. Whereas ECT2 did not impact the processing of unmethylated pri-miRNAs, the protein could significantly enhance the cleavage efficiency of methylated pri-miRNAs (Fig. 8a,b). Furthermore, this enhancement was remarkable when the ECT2 concentrations were low but sufficient for binding the m^{6}A sites. Importantly, the ECT2-mediated enhancement of the methylated pri-miRNAs relied on the recognition and binding of m^{6}A by the reader ECT2 as ECT2-W521A did not enhance the cleavage of m^{6}A-methylated pri-miRNAs (Fig. 8a,b). These results suggested that the m^{6}A readers exemplified by ECT2 could launch on m^{6}A sites located on the ss segments of pri-miRNAs while affiliating with microprocessor, consequently facilitating miRNA production. At higher concentrations of ECT2 and its variant, the cleavage efficiency of pri-miRNAs was reduced, probably because ECT2 bound and occupied the duplex regions of pri-miRNAs and blocked their processing. Collectively, we concluded that components of the m^{6}A pathway play both methylation-independent and methylation-dependent roles in promoting miRNA production (Fig. 8c).

Discussion

Here, we report that the MTC and microprocessor, two otherwise distinct RNPs that are respectively engaged in epitranscriptome modification and pri-miRNA processing, can mutually modulate each other's function. On one side, SE acts beyond its canonical role in miRNA biogenesis and functions as a positive regulator of m^{6}A modification. To do this, SE utilizes its intrinsic LLPS capacity to modulate the phase behaviours conferring the solubility of MTB, which would otherwise rapidly form insoluble condensates. The SE-driven liquid phase separation enables MTC to uptake RNA substrates inside the complex to facilitate m^{6}A deposition. Meanwhile, the co-condensate can protect the IDPs from 20S proteasome-mediated degradation. On the other hand, MTC promotes miRNA biogenesis by recruiting the microprocessor to chromatin, initiating co-transcriptional processing of pri-miRNAs. MTC can also deposit m^{6}A on ss basal and flanking regions of pri-miRNAs, granting the m^{6}A readers, exemplified by ECT2, to enrich the substrates and supply them to its tethered microprocessor for continuing processing.

The mechanism of SE-driven phase separation of MTB is different from the way by which SE triggers co-condensation with the microprocessor or its inhibitors, SAID1/2, to regulate miRNA production[6,14,15]. The microprocessor components DCL1 and HYL1 are well-folded proteins. Without SE, these constituents are diffused but still functional and their amount[6,39] even accumulates[16]. Here, MTB, an IDP, heavily relies on SE for its solubility and, to a certain extent, its stability. In this context, SE acts an 'anti-freeze' to shift the equilibrium of MTB away from forming insoluble condensates towards the soluble condensates, conferring the MTC with robust enzymatic activity. Importantly, both SE and MTB can also stabilize each other by altering their conformations and excluding proteasome from the surrounding niche. In this perspective, SE behaves as a 'chaperone', like heat shock proteins (HSPs)[44,45], instead of a well-perceived 'scaffold' for multiple RNPs[13]. Hence, co-condensation of SE and MTB represents an escape mechanism that prevents 20S proteasome-mediated degradation of diffuse proteins, illuminating the roles of phase separation in controlling protein stability. This scenario is reminiscent of the PGL-1/-3 that could evade autophagic degradation by undergoing LLPS[46,47].

Notably, SE-modulated MTB phase separation is also different from the previously reported condensation patterning of mammalian METTL3 or *Arabidopsis* MTA. Mammalian METTL3 and METTL14 are both structured proteins. METTL3, when fused with the IDR of CRY2, could form puncta in mammalian cell lines, while METTL14 could not[18]. In *Arabidopsis*, MTA appears to orchestrate CRY2 in a co-LLPS manner to determine m^{6}A deposition of light signalling genes[19]. However, MTB does not directly interact with CRY2 and it is unlikely that the two proteins undergo co-condensation[19]. Whether MTA–CRY and MTB–SE cross-talk to regulate light signalling pathways or other biological processes warrants further studies.

We rediscovered that m^{6}A could facilitate miRNA production, and uncovered three unique features. First, we accredited the m^{6}A-mediated facilitation of miRNA production to the m^{6}A readers, exemplified by ECT2. This is different from the mechanism in mammals where the enhancement is accredited to HNRNPA2B1, which does not contain the YTH domain and is not a direct m^{6}A 'reader' but could influence miRNA production via an 'm^{6}A switch' mechanism[25]. Second, we pinpointed the m^{6}A modification sites on the ss basal and flanking regions of pri-miRNAs, clarifying earlier confusion of the possible locations of m^{6}A on the stem-loop regions. We argue that methylation in the stem-loop region could impair pri-miRNA processing as m^{6}A inherently inclines to unfold RNAs owing to the frailty of m^{6}A–uracil base pairs[25]. Third, the occupation of m^{6}A readers may spatially obstruct the microprocessor from the accessibility to the substrates. Indeed, both plant m^{6}A reader ECT2 and mammalian HNRNPA2B1 (ref. 24) could bind to the structured regions of pri-miRNAs with approximately an eightfold diminished affinity, independent of m^{6}A recognition, which might subsequently suppress the processing of substrates. In line with this, the m^{6}A writers have been observed to preferably deposit m^{6}A onto ssRNA regions in mammals[48]. Additionally, we elucidated that MTC could orchestrate co-transcriptional processing nearby the chromatin and post-transcriptional processing of pri-miRNAs in the nucleoplasm. Whether MTC possesses such a mechanism in other organisms awaits future investigation.

Online content

Any methods, additional references, Nature Portfolio reporting summaries, source data, extended data, supplementary information, acknowledgements, peer review information; details of author contributions and competing interests; and statements of data and code availability are available at https://doi.org/10.1038/s41556-024-01530-8.

References

1. Alberti, S. & Hyman, A. A. Biomolecular condensates at the nexus of cellular stress, protein aggregation disease and ageing. *Nat. Rev. Mol. Cell Biol.* **22**, 196–213 (2021).
2. Li, P. B. et al. Phase transitions in the assembly of multivalent signalling proteins. *Nature* **483**, 336–340 (2012).
3. Peeples, W. & Rosen, M. K. Mechanistic dissection of increased enzymatic rate in a phase-separated compartment. *Nat. Chem. Biol.* **17**, 693–702 (2021).
4. Chong, S. et al. Imaging dynamic and selective low-complexity domain interactions that control gene transcription. *Science* **361**, eaar2555 (2018).
5. Wei, M. T. et al. Nucleated transcriptional condensates amplify gene expression. *Nat. Cell Biol.* **22**, 1187–1196 (2020).
6. Xie, D. et al. Phase separation of SERRATE drives dicing body assembly and promotes miRNA processing in *Arabidopsis*. *Nat. Cell Biol.* **23**, 32–39 (2021).
7. Shin, Y. & Brangwynne, C. P. Liquid phase condensation in cell physiology and disease. *Science* **357**, eaaf4382 (2017).
8. Banani, S. F., Lee, H. O., Hyman, A. A. & Rosen, M. K. Biomolecular condensates: organizers of cellular biochemistry. *Nat. Rev. Mol. Cell Biol.* **18**, 285–298 (2017).
9. Kato, M. & McKnight, S. L. A solid-state conceptualization of information transfer from gene to message to protein. *Annu. Rev. Biochem.* **87**, 351–390 (2018).
10. Kumar Deshmukh, F., Yaffe, D., Olshina, M. A., Ben-Nissan, G. & Sharon, M. The contribution of the 20S proteasome to proteostasis. *Biomolecules* **9**, 190 (2019).
11. Shang, B., Li, C. & Zhang, X. How intrinsically disordered proteins order plant gene silencing. *Trends Genet.* **40**, 260–275 (2024).

12. Emenecker, R. J., Holehouse, A. S. & Strader, L. C. Emerging roles for phase separation in plants. *Dev. Cell* **55**, 69–83 (2020).
13. Jozwiak, M., Bielewicz, D., Szweykowska-Kulinska, Z., Jarmolowski, A. & Bajczyk, M. SERRATE: a key factor in coordinated RNA processing in plants. *Trends Plant Sci.* https://doi.org/10.1016/j.tplants.2023.03.009 (2023).
14. Li, Q. et al. DEAD-box helicases modulate dicing body formation in *Arabidopsis*. *Sci. Adv.* **7**, eabc6266 (2021).
15. Shang, B. et al. Intrinsically disordered proteins SAID1/2 condensate on SERRATE for dual inhibition of miRNA biogenesis in *Arabidopsis*. *Proc. Natl Acad. Sci. USA* **120**, e2216006120 (2023).
16. Li, Y. et al. Degradation of SERRATE via ubiquitin-independent 20S proteasome to survey RNA metabolism. *Nat. Plants* **6**, 970–982 (2020).
17. Wang, L. et al. PRP4KA phosphorylates SERRATE for degradation via 20S proteasome to fine-tune miRNA production in *Arabidopsis*. *Sci. Adv.* **8**, eabm8435 (2022).
18. Han, D. et al. Dynamic assembly of the mRNA m6A methyltransferase complex is regulated by METTL3 phase separation. *PLoS Biol.* **20**, e3001535 (2022).
19. Wang, X. et al. A photoregulatory mechanism of the circadian clock in *Arabidopsis*. *Nat. Plants* **7**, 1397–1408 (2021).
20. Ries, R. J. et al. m(6)A enhances the phase separation potential of mRNA. *Nature* **571**, 424–428 (2019).
21. Gao, Y. et al. Multivalent m(6)A motifs promote phase separation of YTHDF proteins. *Cell Res.* **29**, 767–769 (2019).
22. Alarcon, C. R., Lee, H., Goodarzi, H., Halberg, N. & Tavazoie, S. F. *N*6-methyladenosine marks primary microRNAs for processing. *Nature* **519**, 482–485 (2015).
23. Bhat, S. S. et al. mRNA adenosine methylase (MTA) deposits m(6)A on pri-miRNAs to modulate miRNA biogenesis in *Arabidopsis thaliana*. *Proc. Natl Acad. Sci. USA* **117**, 21785–21795 (2020).
24. Alarcon, C. R. et al. HNRNPA2B1 is a mediator of m(6)A-dependent nuclear RNA processing events. *Cell* **162**, 1299–1308 (2015).
25. Murakami, S. & Jaffrey, S. R. Hidden codes in mRNA: control of gene expression by m(6)A. *Mol. Cell* **82**, 2236–2251 (2022).
26. Zhang, H. et al. A comprehensive online database for exploring approximately 20,000 public *Arabidopsis* RNA-seq libraries. *Mol. Plant* **13**, 1231–1233 (2020).
27. Arribas-Hernandez, L. & Brodersen, P. Occurrence and functions of m(6)A and other covalent modifications in plant mRNA. *Plant Physiol.* **182**, 79–96 (2020).
28. Erdos, G., Pajkos, M. & Dosztanyi, Z. IUPred3: prediction of protein disorder enhanced with unambiguous experimental annotation and visualization of evolutionary conservation. *Nucleic Acids Res.* **49**, W297–W303 (2021).
29. Jumper, J. et al. Highly accurate protein structure prediction with AlphaFold. *Nature* **596**, 583–589 (2021).
30. Evans, R. et al. Protein complex prediction with AlphaFold-Multimer. Preprint at *bioRxiv*https://doi.org/10.1101/2021.10.04.463034 (2022).
31. Wang, X. et al. Structural basis of *N*(6)-adenosine methylation by the METTL3–METTL14 complex. *Nature* **534**, 575–578 (2016).
32. Bose, M., Lampe, M., Mahamid, J. & Ephrussi, A. Liquid-to-solid phase transition of oskar ribonucleoprotein granules is essential for their function in *Drosophila* embryonic development. *Cell* **185**, 1308–1324 e1323 (2022).
33. Lu, S. et al. Heat-shock chaperone HSPB1 regulates cytoplasmic TDP-43 phase separation and liquid-to-gel transition. *Nat. Cell Biol.* **24**, 1378–1393 (2022).
34. Cheng, S. et al. Mammalian oocytes store mRNAs in a mitochondria-associated membraneless compartment. *Science* **378**, eabq4835 (2022).
35. Zhong, S. et al. Anaphase-promoting complex/cyclosome regulates RdDM activity by degrading DMS3 in *Arabidopsis*. *Proc. Natl Acad. Sci. USA* **116**, 3899–3908 (2019).
36. Dominissini, D. et al. Topology of the human and mouse m6A RNA methylomes revealed by m6A-seq. *Nature* **485**, 201–206 (2012).
37. Speth, C. et al. *Arabidopsis* RNA processing factor SERRATE regulates the transcription of intronless genes. *eLife* **7**, e37078 (2018).
38. Wang, Z. et al. SWI2/SNF2 ATPase CHR2 remodels pri-miRNAs via SERRATE to impede miRNA production. *Nature* **557**, 516–521 (2018).
39. Gonzalo, L. et al. R-loops at microRNA encoding loci promote co-transcriptional processing of pri-miRNAs in plants. *Nat. Plants* **8**, 402–418 (2022).
40. Bajczyk, M. et al. SERRATE interacts with the nuclear exosome targeting (NEXT) complex to degrade primary miRNA precursors in *Arabidopsis*. *Nucleic Acids Res.* **48**, 6839–6854 (2020).
41. Scutenaire, J. et al. The YTH domain protein ECT2 is an m(6)A reader required for normal trichome branching in *Arabidopsis*. *Plant Cell* **30**, 986–1005 (2018).
42. Wei, L. H. et al. The m(6)A reader ECT2 controls trichome morphology by affecting mRNA stability in *Arabidopsis*. *Plant Cell* **30**, 968–985 (2018).
43. Arribas-Hernandez, L. et al. Principles of mRNA targeting via the *Arabidopsis* m(6)A-binding protein ECT2. *eLife* **10**, e72375 (2021).
44. Mogk, A., Bukau, B. & Kampinga, H. H. Cellular handling of protein aggregates by disaggregation machines. *Mol. Cell* **69**, 214–226 (2018).
45. Tyedmers, J., Mogk, A. & Bukau, B. Cellular strategies for controlling protein aggregation. *Nat. Rev. Mol. Cell Biol.* **11**, 777–788 (2010).
46. Zhang, G., Wang, Z., Du, Z. & Zhang, H. mTOR regulates phase separation of PGL granules to modulate their autophagic degradation. *Cell* **174**, 1492–1506 e1422 (2018).
47. Zheng, H., Peng, K., Gou, X., Ju, C. & Zhang, H. RNA recruitment switches the fate of protein condensates from autophagic degradation to accumulation. *J. Cell Biol.* **222**, e202210104 (2023).
48. Liu, J. et al. A METTL3–METTL14 complex mediates mammalian nuclear RNA *N*6-adenosine methylation. *Nat. Chem. Biol.* **10**, 93–95 (2014).

Methods

No statistical methods were used to pre-determine sample sizes. Randomization and blinding design were not relevant to this study.

Plant materials and growth conditions

Arabidopsis thaliana ecotype Columbia (Col-0), *se-1* (CS3257), *se-2* (SAIL_44_G12), *se-3* (SALK_083196), *hyl1-2* (SALK_064863), *ect2-1* (SALK_002225C) and *ect2*; *ect3*; *ect4* (CS2110132) were used for this study.

For generating knockdown lines, binary vectors including *pBA-p35S*::*amiR-MTA-a*, *pBA-p35S*::*amiR-MTA-b*, *pBA-p35S*::*amiR-MTB* and *pBA-p35S*::*amiR-FIP37* were transformed into Col-0 by the floral-dip transformation method. Transgenic plants were screened for the presence of artificial miRNAs and the decrease of target transcripts using small RNA blot or quantitative PCR with reverse transcription (RT–qPCR), respectively. Subsequently, *amiR-MTA-a* plants were used for the majority of experiments as *mta*, including RNA-seq, m^6A analysis, miRNA analysis and crossed with *pMIR167A::β-glucuronidase* (*GUS*) for GUS histochemical analysis. The 20S proteosome mutants were generated in a previous study[16].

The *pSE*::*FM-SE* and *pSE*::*gSE-eGFP* (renamed as *pSE*::*SE-GFP*) were generated in previous studies (respectively, refs. 15and [38]). For generating additional complementation and mutation lines, the homozygous *se-1*$^{-/-}$ mutant was transformed with binary vectors of *pBA-pSE*::*SE* derivatives by the floral-dip transformation method[49]. The transgenic plants were screened by western blot analysis and RT–qPCR. Subsequently, to test whether SE and its derivatives can restore the overexpression of MTB, a background switch was achieved by crossing transgenic plants with *se-1*; *p35S::Flag-MTB*.

For generating transgenic lines, binary vectors *pH7-pMTB*::*YFP-gMTB* and *pBA-p35S*::*FM (Flag-4xMyc)-FIP37* were transformed into Col-0, and *pBA-pMTB*::*mCherry-gMTB* was dipped into *pSE*::*SE-GFP*[15], respectively. The T1 transgenic lines expressing the tagged proteins were screened by western blot analysis or confocal microscopy. Subsequently, *pH7-pMTB*::*YFP-gMTB* was crossed with *se-1* to switch background.

Col-0 (WT), mutants and transgenic lines were grown on soil (Jolly Gardener/LP5) or MS plates under a 12 h light/12 h dark regime at 22 ± 1 °C and ~50% relative humidity. Typically, 3-week-old plants were collected for MeRIP-seq, RNA-seq, small RNA (sRNA)-seq, RT–qPCR, western blot analyses and ChIP/RIP PCR, unless specifically mentioned.

The Col-0; *pMIR167A*::*GUS*, Col-0; *p35S*::*Flag-MTA*, Col-0; *p35S*::*Flag-MTB*, *se-1*; *p35S*::*Flag-MTA* and *se-1*; *p35S*::*Flag-MTB* seeds were generated by Dr. Bin Yu's laboratory. The *ect2-1*; *ect3-1*; *ect4-2*; *pECT2*::*ECT2-mCherry* (CS2110846) and *ect2-1*; *ect3-1*; *pECT2*::*3xHA-ECT2* (CS2110850) were obtained from Arabidopsis Biological Resource Center. The mutants were crossed with *ect2-1* to switch background(s).

Vector construction

The plant binary constructs were made using the Gateway system (Thermo Fisher). For the majority of coding DNA sequences (CDSs) and genomic sequences, an entry vector, pENTR1A (Thermo Fisher), was used for initial cloning, followed by the recombination reaction between attL and attR sites (LR reaction). Constructions using digested vectors were performed using either T4 ligations or NEBuilder HiFi DNA Assembly Master Mix with the standard procedure. The complete list of primers for all constructs can be found in Supplementary Table 7.

The CDS of *MTA*, *MTB*, *N-truncated MTB* (1–634), *C-truncated MTB* (635–963), *FIP37*, ECT2 and *VIR*, and the genomic DNA of *gMTA* and *gMTB* were amplified and cloned into a pENTR1A vector. The point mutation and truncation derivates of SE and point mutation of ECT2 were generated by PCR and cloned into a pENTR1A vector; the chimera protein of *LCD*^{FUS}*-SEΔIDR1* was obtained with a previous approach[6] and cloned into a pENTR1A vector. The binary vector of *pBA-pSE*::*DC* and *pBA-pSE*::*mCherry-DC* was generated using the 2,241 bp before the start codon, as in a previous study[38]. The same promoter sequence of *SE* was adopted to generate *pBA-pSE*::*mCherry-DC*. The LR reaction was performed with *pBA-pSE*::*DC* and pENTR1A carrying different variants, yielding *pBA-pSE*::*SE* and its derivates.

To generate native promoter-driven plasmids, 3,223 bp and 2,374 bp before the start codon were chosen as promoters for *MTA* and *MTB*, respectively. The promoters were amplified and cloned into pBA002a-DC-CFP (digested by BamH I and Xba I), *pBA002a-mCherry-DC* (digested by BamH I and Xba I) and pH7WGY (digested by SpeI and Sac I) through HIFI recombination (New England Biolabs (NEB)), yielding *pBA-pMTA*::*DC-CFP*, *pBA-pMTB*::*mCherry-DC* and *pH7-pMTB*::*YFP-DC*. For protein transient expression in *Arabidopsis* mesophyll protoplast and tobacco plants, *pENTR1A-MTA, pENTR1A-MTB* and *pENTR1A-SE* and its variants were used in the LR reaction to generate *pBA-p35S*::*MTA-CFP*, *pBA-pMTA*::*MTA-CFP*, *pH7-p35S*::*YFP-MTB*, *pH7-pMTB*::*YFP-MTB*, *pBA-p35S*::*mCherry-SE*, *pBA-pSE*::*mCherry-SE* and its derivates. To make transgenic plants, *pENTR1A-gMTB* was used in the LR reaction to obtain the binary construct of *pBA-pMTB*::*mCherry-gMTB* and *pH7-pMTB*::*YFP-gMTB*.

For generating artificial miRNA constructs, a template of *pENTR-amiR159*(ref. 16) was amplified with specific primers and the PCR products were subjected to Xma I and Bgl II digestion. The resulting fragments were ligated to the Xma I and Bgl II digested *pENTR/D-amiR-PAG1*(ref. 16) backbone to generate *pENTR/D-amiR-gene*. For generating Y2H constructs, the destination vectors *pGADT7-DC* and *pGBKT7-DC* were used in the LR reaction. For generating BiFC constructs, *pBA-p35S*::*nYFP-DC* and *pBA-p35S*::*cYFP-DC* were used in the LR reaction. For generating LCI constructs, *pCambia1300-p35S*::*cLUC-HA-DC* and *pCambia1300-p35S*::*MYC-DC-nLUC* were used in the LR reaction. Plasmids containing microprocessor components and 20S proteasome subunits used in Y2H, BiFC and LCI assays were generated in a previous study[16].

For protein purification constructs, CDSs of *MTA*, *FIP37*, *ECT2, ECT2-W521A*, *SE* and its derivates were cloned into a pET28a-6xHis-SUMO vector through BamH I and Sal I restriction sites. *MTB* was cloned into a Xho I/Sma I-digested pAcGHLT-C vector. For fluorescence-tagged constructs, *mCherry-FUS*^{LCD}, *MTA-CFP*, *YFP-MTB*, *mCherry-SE* and *mCherry-SE-variants* were amplified from *pBA-pSE*::*mCherry-LCD*^{FUS}*-SEΔIDR1*, *pBA-p35S*::*MTA-CFP*, *pH7-p35S*::*YFP-MTB* and *pBA-p35S*::*mCherry-SE* and its derivates, respectively.

Leptomycin B treatment

Five-day-old vertical cultured seedlings were transferred to 3 ml liquid MS medium for 12 h, then leptomycin B (Enzo Life Sciences) was added to 2.5 μM, or an equal amount of 100% ethanol was added to the medium and incubated for another 12 h.

Nuclear–cytoplasmic fractionation

The 3-week-old plants were used for nuclear–cytoplasmic fractionation. Briefly, 0.5 g of plant was homogenized with liquid nitrogen to obtain a fine powder and then suspended with 6 ml of lysis buffer (20 mM Tris–HCl pH 7.5, 20 mM KCl, 2 mM EDTA, 2.5 mM $MgCl_2$, 25% glycerol, 250 mM sucrose, 5 mM dithiothreitol (DTT), 50 μM MG-132 and 1× protease inhibitor (Roche)). Then, 100 μl of lysate was collected as 'total'. The lysates were then filtered through two layers of Miracloth twice and centrifuged at 1,500*g* for 10 min at 4 °C. After centrifugation, 1 ml of the supernatant was collected as 'cytoplasmic fraction' followed by another centrifuged at 10,000*g* for 10 min at 4 °C. The pellet from 6 ml of lysate was washed with 5 ml of nuclear resuspension buffer 1 twice (20 mM Tris–HCl pH 7.4, 25% glycerol, 2.5 mM $MgCl_2$ and 0.2% Triton X-100). After washing, the pellet was resuspended with 500 μl of nuclear resuspension buffer 2 (20 mM Tris–HCl pH 7.5, 0.25 M sucrose, 10 mM $MgCl_2$, 0.5% Triton X-100, 5 mM β-mercaptoethanol, 50 μM MG-132 and 1× protease inhibitor (Roche)). Then, the resuspended sample was carefully added on the top of 500 μl of nuclear resuspension buffer 3 (20 mM

Tris–HCl pH 7.5, 1.7 M sucrose, 10 mM $MgCl_2$, 0.5% Triton X-100, 5 mM β-mercaptoethanol, 50 μM MG-132 and 1× protease inhibitor (Roche)) and they were centrifuged at 16,000*g* for 45 min at 4 °C. The final pellet was resuspended in 300 μl of nuclei sonication buffer (40 mM Tris–HCl pH 7.4, 150 mM NaCl, 5 mM $MgCl_2$, 1% SDS, 1 mM DTT, 1% Triton X-100, 2% glycerol, 1 mM phenylmethyl sulfonyl fluoride (PMSF), 50 μM MG-132 and 1× protease inhibitor (Roche)). Sonication was performed with 15 cycles of 30 s sonication and 90 s pause. Following centrifugation at 21,000*g* for 15 min at 4 °C, the supernatant was collected as the 'nuclear fraction'. The method was adopted from a previous study[16].

Nucleoplasmic RNA extraction

The nucleoplasmic fraction was obtained with a modified method adopted from a previous study[50]. Briefly, 2 g from 3-week-old seedlings was homogenized with liquid nitrogen to obtain a fine powder and then suspended with 12 ml Honda buffer (0.44 M sucrose, 1.25% (w/v) Ficoll, 2.5% (w/v) dextran T40, 20 mM HEPES–KOH pH 7.4, 10 mM $MgCl_2$, 1 mM DTT, 1× protease inhibitor (Roche) and 10 U ml^{-1} SUPERase-In RNase Inhibitor). Debris was removed by passing through two layers of a Miracloth twice. The pellet was obtained by centrifugation at 1,500*g* for 10 min at 4 °C, followed by a wash with 5 ml of Honda buffer containing 0.5% Triton X-100 for three times. The final pellet was collected as nuclei. The nuclei were then fully resuspended in 1 ml of nuclear lysis buffer (25 mM HEPES–KOH pH 7.4, 300 mM KCl, 0.8 M urea, 1 mM DTT, 1% Tween-20, 200 U ml^{-1} SUPERase-In RNase Inhibitor) and centrifuged at 21,000*g* for 10 min at 4 °C. The supernatant was collected as the nucleoplasmic fraction. The nucleoplasmic fraction was then subjected to TRIzol treatment for RNA isolation,

Sedimentation assay

Ten-day-old seedling and 3-week-old plants were collected and frozen in liquid nitrogen. Samples were ground into a fine powder and aliquoted into Eppendorf tubes. To extract total protein, a fivefold weight volume of 1× SDS loading buffer was added to the powder. Alternatively, the powder was mixed with fourfold weight volume of lysis buffers (40 mM Tris–HCl pH 8.0, 50–800 mM NaCl, 2 mM $MgCl_2$, 50 μM $ZnCl_2$, 1 mM DTT, 0.5% Triton X-100, 2% glycerol, 1 mM PMSF, 50 μM MG-132 and 1× Complete EDTA-free protease inhibitor (Roche)) and rotated for 20 min at 4 °C. Subsequently, the lysate was subjected to centrifugation at 21,000*g* for 15 min at 4 °C. The resulting supernatant was collected and mixed with onefold weight volume of 5× SDS loading buffer, referring to the soluble fraction. Meanwhile, the resulting pellet was resuspended with a fivefold volume of 1× SDS loading buffer and collected as the insoluble fraction.

To quantify, the enrichment was calculated as ($supernatant_{protein}$/$supernatant_{control}$)/($pellet_{protein}$/$pellet_{control}$). The relative enrichment was further compared with that of Col-0 at the condition of 50 mM NaCl lysis buffer, in which the value was arbitrarily set as 1.

Western blot

The blots were detected with primary antibodies against Flag (Sigma-Aldrich, A8592, immunoblotting (IB) 1:5,000), actin (Sigma-Aldrich, A0480, IB 1:5,000), histone 3 (Agrisera, AS10 710, IB 1:5,000), AGO1 (Agrisera, AS09 527, IB 1:1,000), SE (Homemade, IB 1:5,000)[16], ubiquitin (Santa Cruz Biotechnology, sc8017, IB 1:1,000), HYL1 (homemade, IB 1:5,000)[16], YFP and GFP (Roche, 11814460001, IB 1:2,000), DCL1 (Agrisera, AS12 2102, IB 1:1,000), His (Sigma-Aldrich, H1029, IB 1:5,000), HSP70 (Agrisera, AS08 371, IB 1:5,000), UGPase (Agrisera, AS14 2813, IB 1:5,000), MTA (homemade, IB 1:1,000) and MTB (homemade, IB 1:1,000). The control IPs were conducted with IgG (Sigma-Aldrich, I4506, 3 μg per IP). Secondary antibodies were goat-developed anti-rabbit (Cytiva, NA934, IB 1:3,000) and anti-mouse IgG (Cytiva, NA931, IB 1:3,000). The anti-MTA and anti-MTB antibodies were generated by Dr. Zhonghui Zhang's laboratory using full-length recombinant proteins from *E. coli*. Detailed validation is described in the Nature Portfolio Reporting Summary and shown in the Supplementary Information.

Co-IP

Three-week-old *Arabidopsis thaliana* plants were collected and immediately frozen in liquid nitrogen before being ground into a fine powder. The total protein was extracted with a buffer containing 40 mM Tris–HCl pH 8.0, 150 mM NaCl, 2 mM $MgCl_2$, 50 μM $ZnCl_2$, 1 mM DTT, 0.5% Triton X-100, 2% glycerol, 1 mM PMSF, 50 μM MG-132 and one pellet per 10 ml of complete EDTA-free protease inhibitor (Roche). The supernatant obtained after centrifugation was incubated with antibody-conjugated beads at 4 °C for 2 h. Anti-Flag M2 magnetic beads (Sigma-Aldrich, M8823) and GFP-trap magnetic beads (ChromoTek, gtma) were used for enriching Flag- and YFP-tagged proteins, respectively. In contrast, protein A/G beads conjugated with indicated antibodies were employed for other targets. Immunoprecipitate with IgG was used as a negative control. Unspecific-bound binding was eliminated by five consecutive washes with IP buffer, and the beads were subsequently boiled with 2× SDS loading buffer for western blot analyses. For the co-IP assays with RNase digestion, 50 μg ml^{-1} of RNase A (Sigma-Aldrich, R4875) was added to lysates and then incubated at room temperature for 10 min before IP.

RIP/ChIP assay

Three-week-old seedlings were cross-linked using the buffer (20 mM Tris–HCl pH 7.4, 1 mM PMSF, 1 mM EDTA, 0.4 M sucrose and 1% formaldehyde) and ground to fine powder in liquid nitrogen. Plant nuclei were isolated from 2 g of material and homogenized with 300 μl of the nuclei sonication buffer (40 mM Tris–HCl pH 7.4, 150 mM NaCl, 5 mM $MgCl_2$, 50 μM $ZnCl_2$, 1% SDS, 1 mM DTT, 1% Triton X-100, 2% glycerol, 1 mM PMSF, 50 μM MG-132, one pellet per 10 ml complete EDTA-free protease inhibitor and 100 U ml^{-1} SUPERase-In RNase Inhibitor). Sonication was performed with 15 cycles of 30 s sonication and 90 s pause for MTA IP, and 12 cycles for H3 IP[51]. Following centrifugation at 21,000*g* for 15 min at 4 °C, the supernatant was diluted with a ninefold volume of dilution buffer (40 mM Tris–HCl pH 7.4, 150 mM NaCl, 5 mM $MgCl_2$, 50 μM $ZnCl_2$, 1 mM DTT, 2% glycerol, 1 mM PMSF, 50 μM MG-132, one pellet per 10 ml complete EDTA-free protease inhibitor and 100 U ml^{-1} SUPERase-In RNase Inhibitor) before IP. The IPs were performed at 4 °C with agitation for 2 h (RIP) or overnight (ChIP). Either antibodies of endogenous MTA and H3 or Flag antibodies were used for RIP or ChIP, respectively. IP samples were subjected to a series of washing steps involving dilution buffer, high salt wash buffer (20 mM Tris–HCl pH 7.4, 500 mM NaCl, 5 mM $MgCl_2$, 50 μM $ZnCl_2$, 1 mM DTT, 1 mM PMSF, 0.5% Triton X-100, 50 μM MG-132, one pellet per 10 ml complete EDTA-free protease inhibitor and 200 U ml^{-1} SUPERase-In RNase Inhibitor), LiCl wash buffer (0.25 M LiCl, 1% NP-40, 1% sodium deoxycholate, 20 mM Tris–HCl pH 7.4 and 1 mM EDTA) and Proteinase K buffer (20 mM Tris–HCl pH 7.4, 200 mM NaCl and 100 U ml^{-1} SUPERase-In RNase Inhibitor). Each washing step included a quick buffer resuspension and centrifugation at 1,000*g* for 1 min at 4 °C followed by a second wash with 5 min agitation. RNA or DNA was eluted from de-cross-linking with Proteinase K solution (20 mM Tris–HCl pH 7.4, 200 mM NaCl, 1 mg ml^{-1} Proteinase K, 1% SDS and 200 U ml^{-1} SUPERase-In RNase Inhibitor) on a Thermomixer shaker at 65 °C for 6 h. The RNA was then purified using RNA Clean and Concentrator kits (ZYMO, R1017) and treated with DNase before RT–qPCR analysis. The DNA was subjected to RNase treatment and then purified using DNA Clean and Concentrator kits (ZYMO, D4004).

RT–qPCR

DNA was removed before reverse transcription with a mixture of random hexamers and $oligo(dT)_{12\text{-}18}$. Primers for stem-loop RT–qPCR of miRNA expression can be found in the previous study[52]. Relative expression level was calculated with the $2^{-\Delta\Delta Ct}$ method. Primers are listed in Supplementary Table 7.

sRNA-seq and bioinformatics analysis

Total RNA was extracted from 3-week-old plants, followed by separation of small RNAs in 15% denaturing urea gels and purification for library generation. sRNA was separated in 15% denaturing urea gels and purified for library generation. The library was prepared according to a homemade method[53], which includes adaptor ligation, reverse transcription, PCR amplification and purification. The resulting library was then subjected to high-throughput sequencing and bioinformatics analysis was performed to generate reads per million values based on mapped reads, and miR161.1, as it consistently showed no changes between *mta* and Col-0 plants in both our sRNA RT–qPCR and published sRNA sequencing assays[23], was used for normalization.

Y2H assays

The positive control was adopted from previously study[54]. Briefly, different combinations of constructions were co-transformed into the yeast strain AH109 and grown on synthetic defined medium plates with a screening condition. At least ten independent colonies were tested for each interaction.

In vitro 20S proteasome decay assay

The 20S proteasome and the control IP were purified from 5 g of powder of *pPAG1*::*gPAG1-FM* transgenic plants[16,55] and Col-0 using 300 µl of M2 beads, respectively. The immunoprecipitates were subjected to stringent washes with 800 mM NaCl buffer. The purified proteasome that tested active using succinyl-Leu-Leu-Val-Tyr -7-amido-4-methylcoumarin (Sigma-Aldrich, S6510) was used for further assay[55]. The concentrations of 20S proteasome and test proteins were determined by the Bradford method using bovine serum albumin as a standard. Specifically, recombinant purified SE (100 nM) and Flag–MTB (10 nM), immunoprecipitated from *p35S*::*Flag-MTB* plants, were incubated with purified 20S proteasome (20 nM) in a reaction buffer (50 mM Tris–HCl pH 7.5 and 150 mM NaCl) containing 2% dimethylsulfoxide (DMSO) or 50 µM MG-132. The aliquots were incubated in a PCR machine at 22 °C with a 37 °C lid. The reaction was stopped by adding SDS–polyacrylamide gel electrophoresis (PAGE) loading and boiling.

Expression and purification of recombinant protein

GST-6×His-DCL1 and HYL1 proteins were purified in previous work[38]. For purification of SE and its derivatives fused with or without mCherry, MTA, MTA–CFP, FIP37, LCD of FUS, ECT2 and ECT2-W521A, recombinant proteins were purified in bacterial cells. To induce recombinant protein expression in *E. coli*, cells transformed into BL21(DE3) were grown in LB medium at 37 °C until OD_{600} reached 0.6. Recombinant protein expression was induced by adding isopropyl-β-D-thiogalactopyranoside to 0.5 mM and incubated at 16 °C overnight. The induced cells were collected and resuspended in the lysis buffer (20 mM Tris–HCl pH 8.0, 800 mM NaCl, 2% glycerol, 1 mM β-mercaptoethanol, 1 mM PMSF, 0.5% Triton X-100 and one pellet per 50 ml Complete EDTA-free protease inhibitor (Roche)) and disrupted by using a high-pressure homogenizer (Microfluidics). The cleared lysate was supplemented with 20 mM imidazole and loaded on a HisTrap HP column (GE Healthcare, 17-5248-02). The peak fractions containing the recombinant proteins were pooled and digested by adding 30 µg of His-SUMO Protease during dialysis with 2 l buffer (20 mM Tris–HCl pH 8.0, 500 mM NaCl and 1 mM β-mercaptoethanol) at 4 °C for 12 h. Ni beads were used to remove uncut proteins and His-SUMO protease. Cleaved recombinant proteins were loaded onto a HiLoad 16/600 Superdex 200 pg column for further purification with an identical condition (20 mM Tris–HCl pH 8.0 and 500 mM NaCl). The two-step purified proteins were either concentrated or dialysed with 2 l dialysis buffer (20 mM Tris–HCl pH 8.0, 150 mM NaCl, 5 mM β-mercaptoethanol and 40% glycerol) at 4 °C for 12 h. Concentrated proteins were immediately used for in vitro phase separation assays. The dialysed proteins were flash frozen in liquid nitrogen and then stored at −80 °C.

For purification of MTB and YFP–MTB, *pAcGHLT-GST-6xHis-MTB* and *pAcGHLT-GST-6xHis-YFP-MTB* were co-transfected with BaculoGold baculovirus DNA (BD Biosciences, 554740) into sf9 insect cells (BD Biosciences, 554738; authenticated by the vendor BD Biosciences) to generate recombinant baculovirus according to the manufacturer's instructions. The recombinant viruses were amplified for two rounds, and P3 virus was collected for large-scale protein expression. P3 virus was added to 2.5×10^6 sf9 insect cells per ml for propagation, and insect cells were collected 70 h later. The cell pellet was resuspended in lysis buffer (50 mM Tris–HCl pH 8.0, 1 M NaCl, 2% glycerol, 2 mM β-mercaptoethanol, 3 mM PMSF, 1% Triton X-100 and one pellet per 50 ml Complete EDTA-free protease inhibitor (Roche)) and disrupted with a high-pressure homogenizer (Microfluidics). The lysate was load onto to HisTrap HP column and the elutes containing the recombinant proteins were pooled and subjected to two continued dialysis with 1 l buffer (20 mM Tris–HCl pH 8.0, 500 mM NaCl and 1 mM β-mercaptoethanol) at 4 °C for 2 h per time. Then, the proteins were loaded onto a GST trap and the elutes containing the recombinant proteins were pooled and subjected to thrombin protease (Sigma) digestion with 2 l buffer (20 mM Tris–HCl pH 8.0, 500 mM NaCl and 1 mM β-mercaptoethanol) at 4 °C for 16 h. Cleaved recombinant proteins were loaded onto a HiLoad 16/600 Superdex 200 pg column for further purification with an identical condition (20 mM Tris–HCl pH 8.0 and 500 mM NaCl). Purified proteins were either concentrated for in vitro phase separation assays or dialysed with 2 l buffer (20 mM Tris–HCl pH 8.0, 500 mM NaCl, 5 mM β-mercaptoethanol and 40% glycerol) at 4 °C for 6 h for storage at −80 °C.

In vitro condensate formation

Aliquots of tested proteins were centrifuged at 15,000*g* for 5 min to remove any aggregates. Droplet formation was induced by diluting the proteins using Tris–HCl pH 7.5 at 20 mM. All of in vitro phase separation experiments were carried out in buffer with a final salt concentration of 20 mM Tris–HCl pH 7.5, 150 mM NaCl and 50 µM $ZnCl_2$ without crowding agent, unless mentioned in figure legends. Slides were imaged at 5 min intervals starting from the preparation to allow ample time for droplet settling on the glass surface.

We conducted in vitro co-condensate formation through three distinct approaches as depicted in Fig. 2c. In the first method (Fig. 2c, top), individual proteins were initially adjusted to concentrations ranging from 800 mM to 150 mM in the protein buffer before their combination. Subsequently, the resultant mixture was examined using confocal microscopy. In the second approach (Fig. 2c, middle), different proteins were initially combined in a solution containing 800 mM NaCl. The salt concentration was then reduced to 150 mM through dilution before further analysis. Finally (Fig. 2c, bottom), SE droplets were first formed before the sequential addition of other proteins and RNAs.

Confocal microscopy and analysis

All image acquisitions were carried out using a Leica stellaris 5 laser-scanning confocal microscope with a HC PL APO 63×/1.40 oil-immersion objective and LAS X Life Science Microscope software. Sequential scanning module was applied when two or more fluorescence signals expected.

For observation of in vitro condensates, the excitation wavelengths of CFP, GFP, YFP, mCherry and Cy5 are 405 nm, 488 nm, 514 nm, 587 nm and 651 nm, respectively. The corresponding emissions for each of these proteins are 470–515 nm, 500–530 nm, 525–550 nm, 597–630 nm and 661–700 nm, respectively. For observation of protoplast, root tip and pollen samples, the excitation wavelengths of CFP, GFP, YFP and mCherry were 405 nm, 488 nm, 514 nm and 587 nm, respectively. Accordingly, the emissions for each of these proteins are 470–515 nm, 498–530 nm, 524–550 nm, and 597–630 nm, respectively. Chlorophyll auto-fluorescence was detected at 680–710 nm.

To perform time-lapse microscopy of in vitro condensate fusion, the samples were observed as described method without a 15 min interval, and images were captured every 5 s over 15 min. Time-lapse microscopy of in vivo condensate fusion was executed by acquiring images every 5 s over 5 min.

To perform 3D rendering analysis of in vitro and in vivo assays, condensates on the glass surface and the signals located in the same layer as the cell nucleus were scanned with LIghtning module, respectively. The 3D stimulation was carried out with LAS X Life Science Microscope software.

BiFC

The isolation and transfection of *Arabidopsis* mesophyll protoplasts from 4-week-old Col-0 and *se-1* plants were used. Approximately 12 h after transfection, the fluorescence signals in the protoplasts were visualized using a Leica stellaris 5 laser-scanning confocal microscope.

FRAP

All FRAP assays were carried out using Leica stellaris 5 laser-scanning confocal microscope with a HC PL APO 63× /1.40 oil-immersion objective and LAS X Life Science Microscope software.

Condensates were subjected to photobleaching using a laser intensity of 100% at corresponding emission, and pre-bleaching fluorescence intensity was obtained by capturing five images. Fluorescence intensity was then recorded every 5 s for 10 min after bleaching. FRAP analysis was performed using fluorescence intensity values and double normalization with pre-bleaching and unbleaching regions, as well as dynamic range scaling from 0 to 1.0.

Liquid chromatography–mass spectrometry

Isolation of mRNA from total RNAs was performed using oligo$(dT)_{25}$ Dynabeads (NEB, S1419S). Next, 500 ng of mRNAs were subjected to enzymatic digestion with nuclease P1 (NEB, M0660S) at 37 °C for 6 h, followed by the addition of NH_4HCO_3 to a final concentration of 110 mM and 1 U of alkaline phosphatase (Sigma-Aldrich, P6774) and incubation at 37 °C for another 6 h. Enzyme activity was quenched by heating samples at 70 °C for 10 min then placing them on ice for 5 min. After centrifugation at 21,000*g* for 15 min, the supernatants were collected for further analysis. Pure commercial adenosine (Sigma-Aldrich, A1852) and m^6A (TargetMol, T6599) standards were also subjected to the same procedure, and standard curves were generated by running the standards of a series of concentration.

HPLC analysis was carried out using an UltiMate 3000 HPLC system equipped with a Phenomenex Luna 5 µm C18(2) 100 Å, 4.6 mm × 50 mm column coupled to MS analysis by an ISQ EM single quadrupole mass spectrometer. The mobile phase consisted of buffer A (0.1% formic acid in water) and buffer B (100% acetonitrile). Nucleosides were quantified using the nucleoside-to-base ion mass transitions of m/z 268.0 (A) and m/z 282.0 (m^6A). The efficiency of the system was tested using commercial methylated and unmethylated standards.

LCI

All of the constructs were then transformed into *Agrobacterium tumefaciens* strain ABI. The OD values were monitored using an ultraviolet-visible spectrophotometer, then the constructs were co-infiltrated with equal ratios into combinations into *N. benthamiana*. The signal of luciferase complementation was captured 72 h after inoculation.

In vitro transcription and labelling of transcripts

In vitro transcription and 5′ labelling of RNA substrates was performed as described previously[56]. RNA substrates were transcribed under the T7 promoter in vitro using PCR products or annealed oligos as templates, followed by DNase treatment. The RNAs were fractionated with denaturing urea–PAGE gels and extracted from gel slices for further analysis. Structured RNAs were obtained by heating to 95 °C for 3 min in RNA folding buffer (40 mM Tris–HCl pH 7.4 and 50 mM KCl) and gradually cooled down to room temperature. Primer and oligo sequences are listed in Supplementary Table 7.

For internal labelling of RNA, a mixture of 10 mM Cy5-UTP (Enzo Life Science) and 50 mM UTP mixture was used for in vitro transcription.

For 5′ end labelling of RNA, 5 pmol of dephosphorylated RNAs were labelled with ^{32}P-γ-ATP (PerkinElmer) by T4 polynucleotide kinase (NEB). Purified RNAs were adjusted to 1,000 counts per min (c.p.m.) per µl.

Methylated pri-miRNA synthesis

Methylated pri-miRNAs were obtained by ligating a methylated oligo and an unmethylated RNA. In the RNA ligation reaction, a donor RNA of extended length was obtained from in vitro transcription and then used for dephosphorylation followed a T4 Kinase treatment to obtain a monophosphate group. A shorter and methylated acceptor RNA was commercially synthesized with hydroxyl groups at both ends. Subsequently, the donor and acceptor RNAs were mixed at 1:10 by molecular weight for ligating reaction (1× RNA ligase 1 buffer, 5% of DMSO, 1 mM of ATP, 1 U μl^{-1} of SUPERase-In RNase Inhibitor, 20% of PEG 8000 and 1 µl of RNA ligase 1) at room temperature for 5 h. RNACleanup XP beads (Beckman Coulter, A63987) were then used to recover RNA with a length greater than 100 nt, which was subsequently subjected for 5′ end ^{32}P-γ-ATP labelling and purification through denaturing urea gel. Finally, the purified RNAs was folded as described above and adjusted to 1,000 c.p.m. μl^{-1}.

EMSAs

Buffers used in EMSA assays were adopted from a previous study[38]. Briefly, recombinant proteins and labelled RNA were mixed in the EMSA buffer (20 mM Tris–HCl pH 8.0, 95 mM NaCl, 1 mM DTT, 0.1% NP-40, 1 U μl^{-1} SUPERase-In RNase Inhibitor). The final pooled concentration of NaCl was ~150 mM, of which 50 mM was from protein solution and 5 mM from RNA solution. Mixtures were incubated at room temperature for 30 min and resolved on native 1% agarose gel. The images were quantified with ImageJ. The K_d and apparent K_d were calculated using Prism 9 (GraphPad) software fitting a Hill slope model.

In vitro microprocessor reconstitution assay

In vitro Microprocessor dicing activity assays were performed according to the established protocol[38]. RNA substrate with ~500–2,000 c.p.m. signal intensity was subjected to incubation with ECT2, ECT2-W521A and His-sumo at the indicated molecular amounts at room temperature for 10 min. The reaction was further initiated by adding 2 pmol of SE, followed by a second incubation of 10 min. A protein mixture containing 2 pmol of HYL1 and 1 pmol of DCL1 was subsequently added to the RNA–proteins mixture and the final pooled salt concentration was adjusted to 20 mM Tris–HCl pH 7.5, 50 mM KCl, 4 mM $MgCl_2$, 1 mM DTT, 5 mM ATP, 1 mM GTP and 1 U μl^{-1} SUPERase-In RNase Inhibitor to initiate processing at 37 °C for 20 min. The reaction was stopped by adding an equal volume of 2× denaturing loading buffer and boiling the mixture at 95 °C for 10 min. The processed products were separated using a denaturing urea gel electrophoresis. Quantification of the microprocessor dicing cleavage efficiency was carried out by the ratio of processed products compared with unprocessed pri-miRNAs.

Mesophyll protoplast assay

Protoplasts were prepared from *Arabidopsis* mesophyll cells. Four-week-old *Arabidopsis* leaves were meticulously sliced into slender strips and subjected to enzymatic digestion in a solution (1.25% cellulose, 0.3% macerozyme, 0.4 M mannitol, 20 mM KCl, 20 mM MES, 10 mM $CaCl_2$, 5 mM β-mercaptoethanol and 0.1% bovine serum albumin). The leaf strips were vacuum infiltrated for 30 min, then incubated in darkness for 3 h at room temperature until the protoplasts were released. Following filtration through a 75 mm mesh nylon membrane,

the protoplasts were collected by centrifugation at 100*g* for 5 min at 4 °C. The collected protoplasts were then subjected to two washes with a cold W5 solution (154 mM NaCl, 125 mM $CaCl_2$, 5 mM KCl, 2 mM MES and 5 mM glucose). The protoplasts were rested on ice for 30 min, centrifuged at 100*g* for 5 min at 4 °C and then resuspended in MMG solution (0.4 M mannitol, 15 mM $MgCl_2$ and 4 mM MES). A mixture of 200 µl of the MMG solution containing approximately 10^6 protoplasts, 10 µg of each plasmid and an equal volume of a PEG solution (comprising 40% PEG 4000, 0.2 M mannitol and 0.1 M $CaCl_2$) was incubated at room temperature for 10 min. Subsequently, 1 ml of W5 solution was added to halt the transfection process, followed by centrifugation at 100*g* for 2 min. The protoplasts were resuspended in 1 ml of W5 solution and incubated in darkness at room temperature overnight. After the transfection, the mesophyll protoplasts were gently resuspended for microscopic examination.

MeRIP-seq and data analysis

MeRIP-seq was conducted using a combination of methods from a previous study[36] and a commercial kit (NEB, E1610S). Briefly, 3-week-old plants were used for mRNA purification. Approximately 5 µg of mRNA mixed with 10 fmol of methylated and unmethylated standards (NEB, E1610S) was used for fragmentation (NEB, E6150S). RNAs were then used for anti-m^{6}A (NEB, E1610S) and anti-GFP (Sigma-Aldrich, G1546) IP, respectively. Immunoprecipitates were washed with series of buffer as protocol suggested and then eluted by incubation with 200 µl Proteinase K solution (50 mM Tris–HCl pH 7.5, 50 mM NaCl, 2 mg ml^{-1} Proteinase K, 1% SDS and 100 U ml^{-1} SUPERase-In RNase Inhibitor) on a Thermomixer shaker at 37 °C for 1 h. RNA purified with Trizol/RNA Clean and Concentrator kits (ZYMO, R1017) was then used for end repair and 5′ end ^{32}P-γ-ATP labelling. Labelled RNA was purified with denature urea gel and then two ends adaptor ligation was conducted. Complementary DNA was synthesized with primer reverse complementary to the 3′ end adaptor. PCR products amplified from RNA-derived cDNA was subjected to sequencing on an Illumina NovaSeq6000 platform in paired-end mode with 150 bp per reads at Novogene.

MeRIP-seq analysis was conducted according to a previous protocol[57]. Briefly, raw data were initially filtered for a quality control and trimmed to remove the adaptor sequences by Cutadapt. Reads were aligned to *Arabidopsis thaliana* reference genome (TAIR 10) using HISAT2. To obtain HC-m^{6}A peaks in each sample, exomePeak2 was conducted with the threshold as $P < 0.05$ and $\log_2$(enrichment) >1. $\log_2$(enrichment) represents $\log_2$(IP/input), $\log_2$(fold change) represents $\log_2(\text{enrichment}_{\text{mutant}}/\text{enrichment}_{\text{WT}})$. To detect differential methylation levels, peak candidate calling by exomePeak2 with $P < 0.99$, $\log_2$(enrichment) >0 and Deseq2 normalization were separated into m^{6}A loci and background depending on whether the candidates overlapped with HC-m^{6}A peaks, respectively. To discover methylation modification on pri-miRNAs, peaks were identified using exomePeak2 with pc_count_cutoff of 10, bg_count_cutoff of 5, $P < 0.05$ and $\log_2$(enrichment) >0, or using sliding window algorithm with a block of 25 nucleotides, IP_mean_count ≥5, winscore >0 and normalization with median of genes[36]. The metagene analysis was performed with the Guitar package. The motif of m^{6}A peaks was analysed using HOMER Motif Analysis. IGV was used to visualize the m^{6}A peaks.

MeRIP RT–qPCR

MeRIP and RNA purification were conducted as described above. To detect m^{6}A on pri-miRNA, full-length mRNAs were used for IP. Subsequently, cDNA was synthesized with oligo(dT) and random hexamers. Enriched m^{6}A signals from IPs were initially normalized to their input and then to that of Col-0 for relative enrichment calculation.

In vitro methylation assay

The RNA substrate sequence was adopted from a previous study[58]. The reaction mixture was performed in a 20 mM Tris–HCl pH 8.0, 100 mM NaCl, 2 mM $MgCl_2$, 50 µM $ZnCl_2$, 1 U µl^{-1} SUPERRNase-In RNase Inhibitor, 2 mM DTT, 6% glycerol, 0.1% NP-40 buffer with 2 µM RNA, 0.1 µM methyltransferase (MTA and MTB), 1 µM auxiliary protein (various forms of SE and His-sumo) and 1 mM SAM (A4377, Sigma) in a total volume of 20 µl. The reaction was conducted at 37 °C for 2 h. The reaction was stopped by adding NaCl to 1 M and was kept at room temperature for 15 min. RNA was then purified using RNA Clean and Concentrator kits (ZYMO, R1017) for subsequent MeRIP enrichment and ^{32}P-γ-ATP labelling. RNA was visualized by running a 15% urea–PAGE gel for phosphor imaging.

Protein 3D structure stimulation

Protein structure prediction was performed using AlphaFold 2.2.0 with the AlphaFold2[29] and AlphaFold-multimer[30] modules for protein monomers and complexes, respectively. The software package was downloaded from the official GitHub repository and the necessary dependencies were installed. The predicted structures were saved in Protein Data Bank format in the output directory and the model with the highest predicted score was used for subsequent analysis. The Protein Data Bank files were visualized using ChimeraX.

Graph drawing

Graphs with dot plots (individual data points) were drawn using GraphPad Prism 9. Models and illustrations were made with Biorender.

Statistics and reproducibility

Statistical analyses of quantification results were performed using GraphPad Prism 9. All statistical data show the mean ± s.d. of at least three biologically independent experiments or samples. Two-tailed unpaired Student's *t*-test, Fisher's exact test, one-way analysis of variance (ANOVA) with Dunnett's multiple comparison test, two-way ANOVA analysis with Dunnett's multiple comparisons test and two-way ANOVA analysis with Tukey's multiple comparisons test were performed in GraphpPad Prism 9. DEseq2 was performed for identifying methylated peaks in MeRIP-seq analysis. The hypergeometric distribution test was conducted in R programming. No statistical method was used to pre-determine sample size, which was determined in accordance with previous studies[6,16,38] and the standard practices in the field. All experiments were independently repeated more than three times with similar results obtained and the exact replicate numbers are provided in the respective figure legends. No data were excluded from our studies. Plants were randomly assigned to experimental groups whenever possible. For other experiments, the experiments were randomized and the investigators were blinded to allocation.

Reporting summary

Further information on research design is available in the Nature Portfolio Reporting Summary linked to this article.

Data availability

All data are available in the main text or the supplementary materials. High-throughput sequencing data generated by this study can be accessed in the National Center for Biotechnology Information BioProject database under accession code PRJNA1102430. SE ChIP-seq data can be accessed in the European Nucleotide Archive under accession number ERP016859 (ref. 37). The MTA sRNA-seq data published in previous study can be accessed in the the National Center for Biotechnology Information Gene Expression Omnibus database under accession code GSE122528 (ref. 23). For pan-transcriptome analysis, data were downloaded from an *Arabidopsis* RNA-seq database, a comprehensive online repository housing over 20,000 publicly available *Arabidopsis* RNA-seq libraries (http://ipf.sustech.edu.cn/pub/athrna/)[26] and the accession codes include DRX065024,DRX065025, DRX065030 (root), DRX066825, DRX092558, DRX092559 (leaf), DRX014760, DRX014761, DRX084079 (seedling), DRX066823, DRX066824, DRX066832

(shoot), GSM1501691, GSM1501692, GSM1694242 (stem), SRX822029, SRX822030, GSM1855883 (meristem), ERX1512314, ERX1512315, ERX1512316 (flower), ERX1719913, ERX1719914, ERX1719915 (seed), GSM1276497, GSM1276499, GSM1276501(embryo), and GSM1276498, GSM1276500, GSM1276502 (endosperm), which are also provided in the Supplementary Table 1. Genetic materials will be available when requested. Source data are provided with this paper.

Code availability

This paper does not report original code.

References

49. Zhang, X., Henriques, R., Lin, S. S., Niu, Q. W. & Chua, N. H. Agrobacterium-mediated transformation of *Arabidopsis thaliana* using the floral dip method. *Nat. Protoc.* **1**, 641–646 (2006).
50. Jia, J. et al. Post-transcriptional splicing of nascent RNA contributes to widespread intron retention in plants. *Nat. Plants* **6**, 780–788 (2020).
51. Zhang, X. et al. A comprehensive map of intron branchpoints and lariat RNAs in plants. *Plant Cell* **31**, 956–973 (2019).
52. Zhang, Z. et al. KETCH1 imports HYL1 to nucleus for miRNA biogenesis in *Arabidopsis*. *Proc. Natl Acad. Sci. USA* **114**, 4011–4016 (2017).
53. Sun, D., Ma, Z., Zhu, J. & Zhang, X. Identification and quantification of small RNAs. *Methods Mol. Biol.* **2200**, 225–254 (2021).
54. Ma, Z. et al. *Arabidopsis* SERRATE coordinates histone methyltransferases ATXR5/6 and RNA processing factor RDR6 to regulate transposon expression. *Dev. Cell* **45**, 769–784 e766 (2018).
55. Li, Y., Sun, D., Yan, X., Wang, Z. & Zhang, X. In vitro reconstitution assays of *Arabidopsis* 20S proteasome. *Bio Protoc.* **11**, e3967 (2021).
56. Zhu, H. et al. Bidirectional processing of pri-miRNAs with branched terminal loops by *Arabidopsis* Dicer-like1. *Nat. Struct. Mol. Biol.* **20**, 1106–1115 (2013).
57. Su, R. et al. METTL16 exerts an m(6)A-independent function to facilitate translation and tumorigenesis. *Nat. Cell Biol.* **24**, 205–216 (2022).
58. Su, S. et al. Cryo-EM structures of human m(6)A writer complexes. *Cell Res.* **32**, 982–994 (2022).

Acknowledgements

This work was supported by grants from the National Institutes of Health (NIH, GM127414) and National Science Foundation (NSF, MCB 1818082) to B.Y., the NSF of Guangdong Province (2020B1515020007), the NSF of China (NSFC, 31771349, 32170593) and the Guangdong Provincial Pearl River Talent Plan (2019QN01N108) to Z.Z., and the NIH (R35GM151976), NSF (MCB 2139857) and the Welch Foundation (A-2177-20230405) to X.Z.

Author contributions

X.Z. and S.Z. conceived the project and designed the experiments. Z.Z. and B.Y. independently discovered the project of SE–MTB interaction. S.Z. performed most of the experiments. X.L. generated genetic materials and plasmids and participated in confocal microscope analysis. Jiyun Zhu and T.M. performed HPLC–MS and data analysis. C.L. analysed MeRIP-seq and sRNA-seq data. H.B. and J.C. generated MTA and MTB antibodies and validated partial results. L.G. created lines of Flag-tagged conjugated MTA and MTB over-expression transgenic plants and native promoter-driven GFP-tagged MTB, with either Col-0 or *se-1* background. Jiaying Zhu, T.O. and N.L. contributed to in vitro RNA transcription. X.Y. participated in protein purification. H.K. and X.P. provided intellectual and experimental support. S.Z. wrote the initial draft of the paper, X.Z. thoroughly edited the paper and all authors contributed to the proofreading.

Competing interests

The authors declare no competing interests.

Additional information

Extended data is available for this paper at https://doi.org/10.1038/s41556-024-01530-8.

Supplementary information The online version contains supplementary material available at https://doi.org/10.1038/s41556-024-01530-8.

Correspondence and requests for materials should be addressed to Zhonghui Zhang or Xiuren Zhang.

Peer review information *Nature Cell Biology* thanks Jungnam Cho, Monika Chodasiewicz, and the other, anonymous, reviewer(s) for their contribution to the peer review of this work. Peer reviewer reports are available.

https://doi.org/10.1038/s41556-024-01530-8

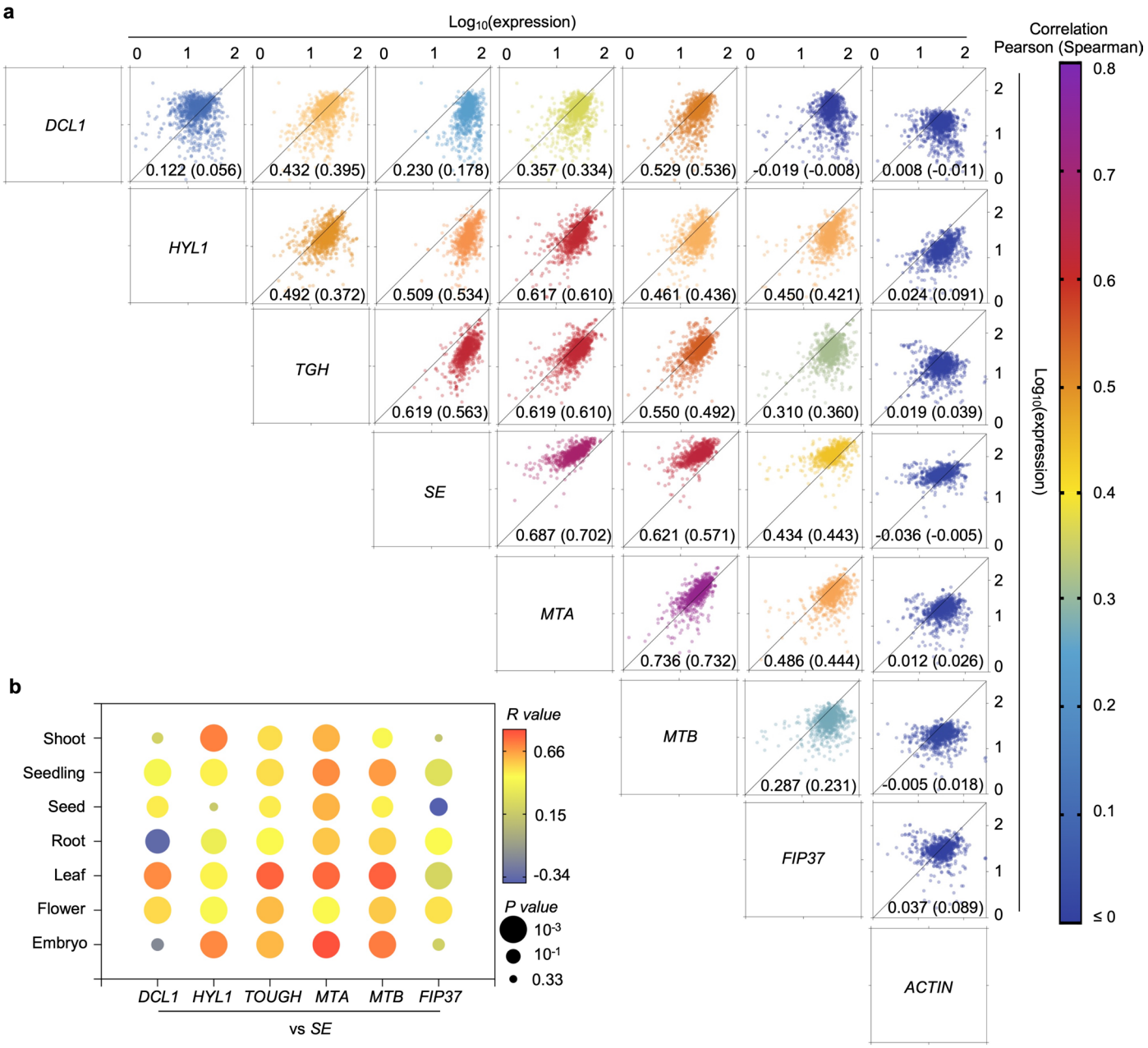

Extended Data Fig. 1 | Pan-transcriptome network association analysis reveals obvious association of the expression patterns between SE and m^{6}A RNA methylation writers. a, **b**, Pan RNA-seq network analysis showed synchronous expression association of microprocessor components and m^{6}A writers over all samples (**a**), or across different tissues (**b**). Spearman (or Pearson) correlation analysis was conducted to assess the expression relationship using over 1,000 RNA-seq data from various wild-type plant tissues. The house keeping gene *ACTIN1* (AT2G37620) serves as a control. Each point in (**a**) represents expression levels of two indicated genes shown in $\log_{10}$(FPKM) in individual RNA-seq datasets. In (**b**), R values, Spearman R correlation. P values for small, medium and large cycles are 0.33, 0.1 and 0.001, respectively. Unpaired two-sided t-test.

https://doi.org/10.1038/s41556-024-01530-8

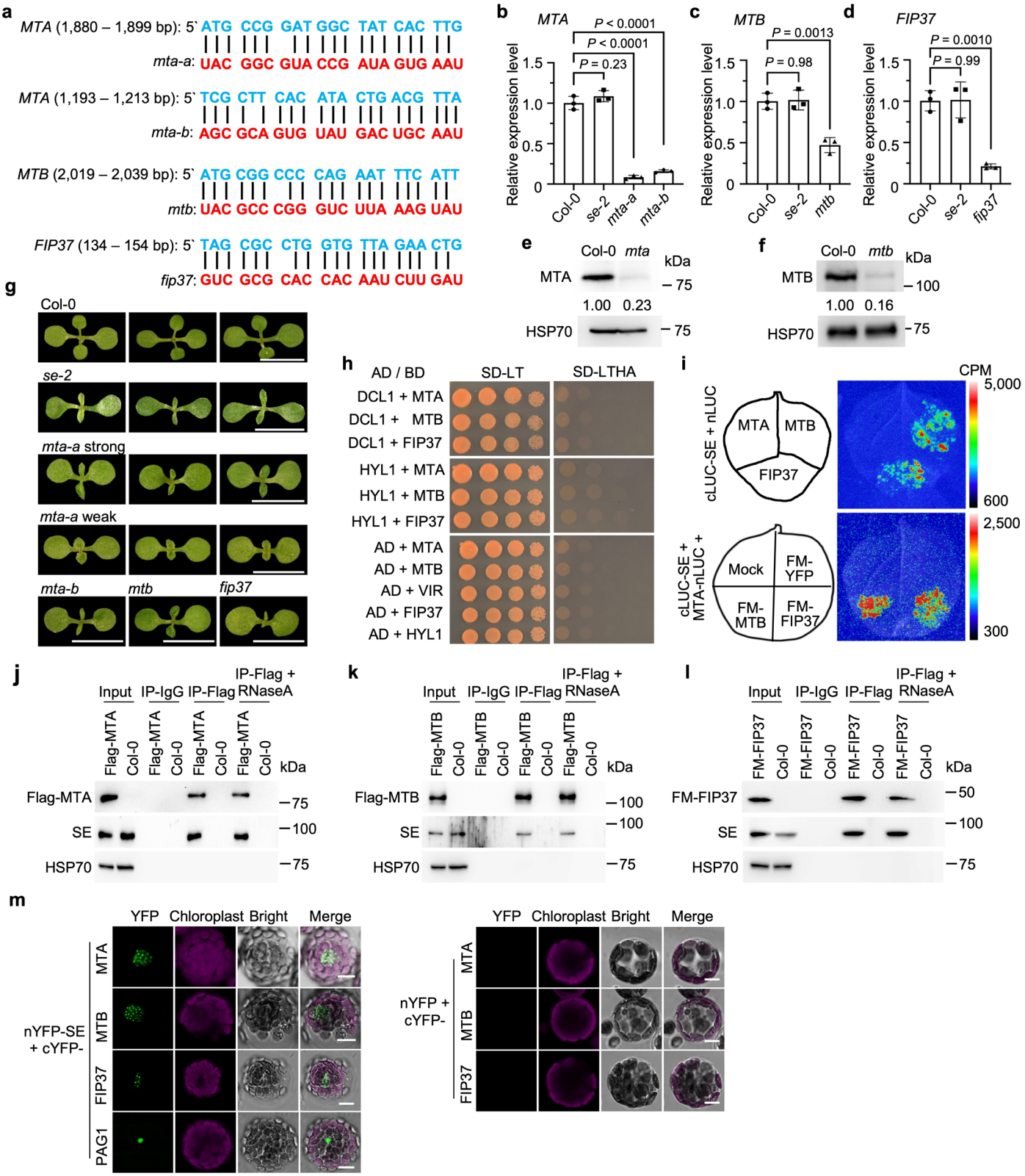

Extended Data Fig. 2 | See next page for caption.

https://doi.org/10.1038/s41556-024-01530-8

Extended Data Fig. 2 | Experimental validation of the genetic association between SE and MTC in developmental processes, modulation of gene expression, and protein-protein interactions. a, Design of artificial miRNAs (*mta-a*, *-b*, *mtb*, and *fip37*). The sequence alignment of the artificial miRNAs (in red) with their target sequences (in blue). Be noted: two independent artificial-miRNA lines for MTB and FIP37 were generated and validated. One elite line for each was used for further studies. **b** – **d**, RT-qPCR assays showed that the amount of *MTA*, *MTB* and *FIP37* transcripts was largely reduced in knockdown lines of *mta* (**b**), *mtb* (**c**), and *fip37* (**d**) vs Col-0 and *se-2*, respectively. Data are mean ± s.d. of three independent experiments. P values, one-way ANOVA analysis with Dunnett's multiple comparisons test. For (b), p values for relative expression of MTA at the *se-2*, *mta-a*, and *mta-b* vs Col-0 are 0.23, < 0.0001, and < 0.0001, respectively. For (c), p values for relative expression of MTB at the *se-2* and *mtb* vs Col-0 are 0.98 and 0.0013, respectively. For (d), p values for relative expression of FIP37 at the *se-2* and *fip37* vs Col-0 are 0.99 and 0.0010, respectively. **e**, **f**, Western blots showed the reduced MTA (**e**) and MTB (**f**) proteins in their amiR-KD lines. Endogenous proteins were detected by indicated antibodies, respectively. HSP70 was a loading control. **g**, Knockdown lines of *mta*, *mtb*, and *fip37* displayed developmental defects in seedlings. The photos were taken of 10-day-old seedlings, with Col-0 and *se-2* serving as controls. Scale bars, 1 cm. **h**, Y2H screening showed that neither DCL1 nor HYL1 directly interact with m^6A writers. 1:5 serial dilutions are shown. -LT, lacking Leu and Trp; -LTHA, lacking Leu, Trp, His and Ade. **i**, LCI assays in *Nicotiana Benthamiana* demonstrated that both MTB and FIP37 can mediate the interaction between MTA and SE. CPM: Count per minute **j** – **l**, Co-IP assays validated the interaction between SE and MTC in plants. Proteins were extracted from transgenic plants of *p35S*::*Flag-MTA* (**j**), *p35S*::*Flag-MTB* (**k**), and *p35S*::*Flag-4xMyc-FIP37* (**l**) transgenic plants, respectively. Lysates were then supplied with or without 50 μg/mL of RNase A prior to IP with an anti-FLAG antibody. SE was detected via a specific anti-SE antibody. HSP70 serves as a negative control. **m**, BiFC assays validated the interactions between SE and MTC in *Arabidopsis* mesophyll protoplast. PAG1 serves as a positive control. and showed similar results. Scale bar, 10 μm. At least three independent experiments were performed (**e**, **f**, **i**, **j**, **k**, and **l**), ten transgenic plants exhibited were photographed (**g**), ten independent colonies (**h**) and ten independent protoplasts for each interaction were tested (**m**), and representative images are shown.

https://doi.org/10.1038/s41556-024-01530-8

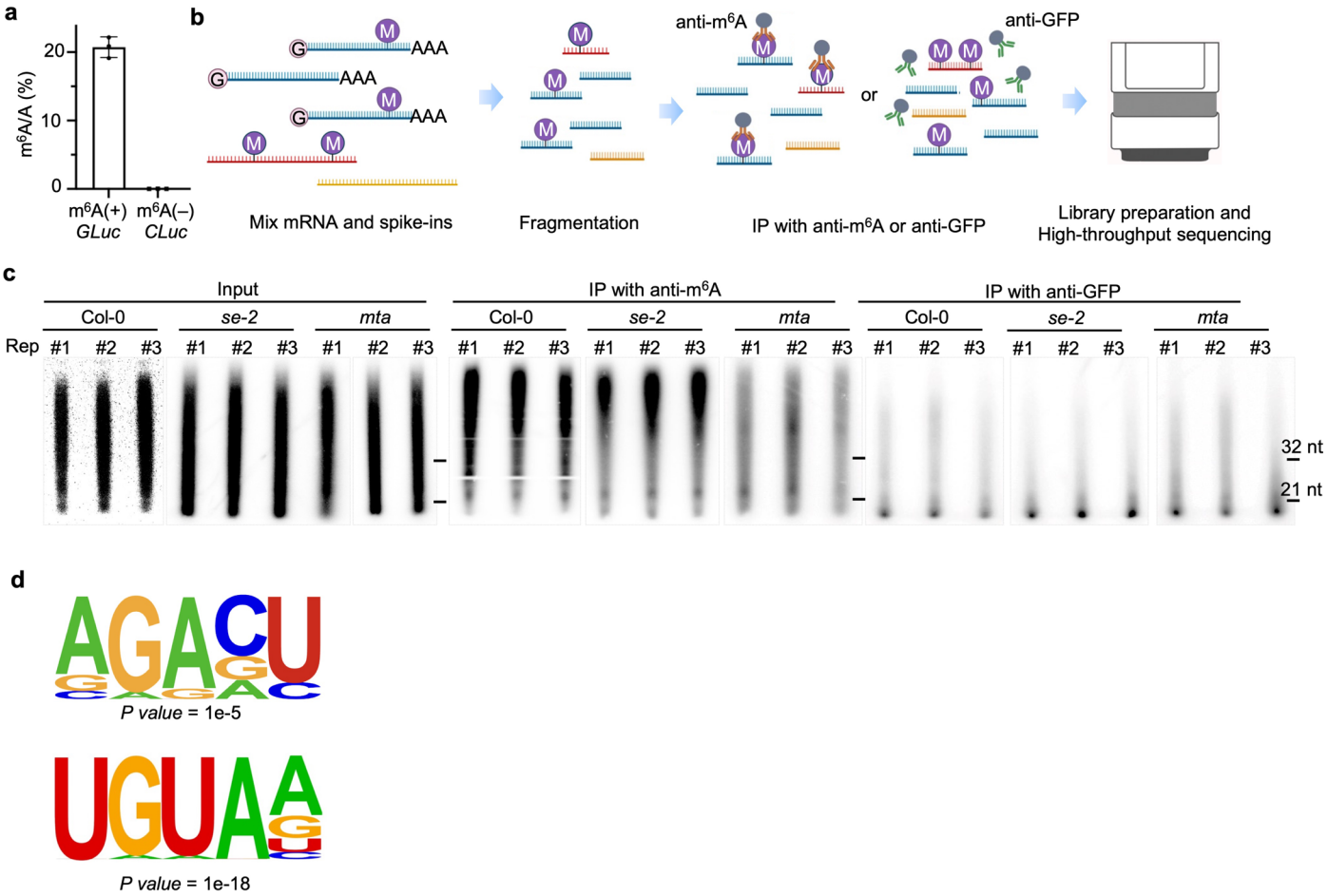

Extended Data Fig. 3 | MeRIP-Seq shows different m^{6}A epi-transcriptome profiling of Poly(A) + RNA in *se* and *mta* vs Col-0. a, HPLC-MS quantification of m^{6}A/A levels of commercial m^{6}A (+) and m^{6}A (−) spike-ins, *GLuc* (m^{6}A/A, ~20%) and *CLuc*, respectively. Data are mean ± s.d. of three independent experiments. **b**, Schematic approach for MeRIP-Seq. Briefly, the purified poly(A) + RNA was mixed with internal controls containing m^{6}A modified (red) and unmodified (yellow) spike-ins, and then fragmented. The resulting fragments were immunoprecipitated using a specific anti-m^{6}A antibody. Parallel IPs using an anti-GFP antibody were performed as negative controls. The IP-ed RNAs were then processed for library construction and high-throughput sequencing, enabling the identification and quantification of m^{6}A modifications at a transcriptome-wide level. **c**, Autography images of input and m^{6}A RNA enriched by indicated antibodies in (**b**). One tenth of the input and all of immunoprecipitated RNA were de-phosphorylated and then labelled with P^{32}-ATP before resolvement in 8% urea gels. **d**, The motif sequences for m^{6}A modifications in the context.

https://doi.org/10.1038/s41556-024-01530-8

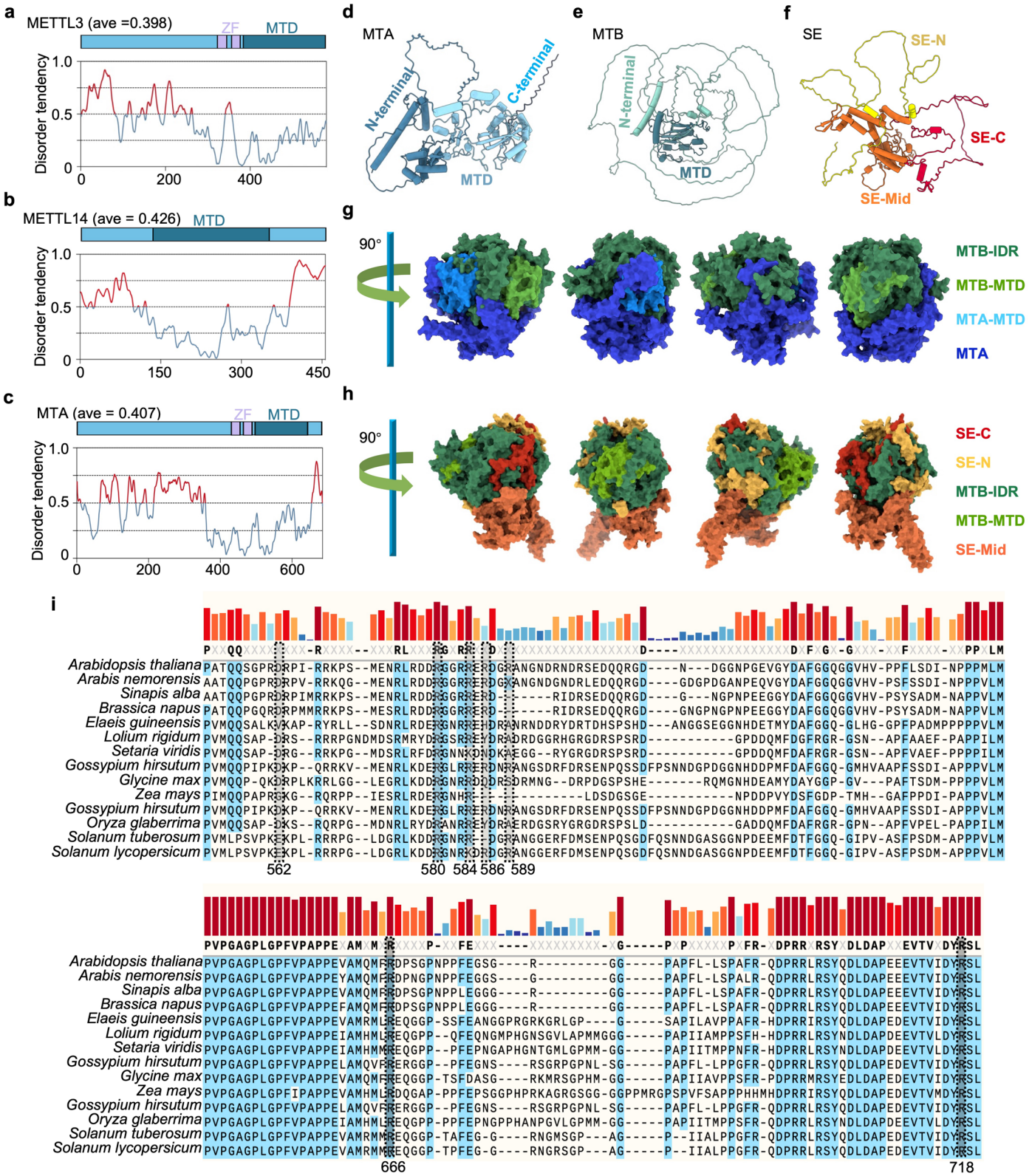

Extended Data Fig. 4 | Computational simulation reveals that the IDR regions of SE and MTB mediate the protein-protein interaction. a – **f**, Computational simulation via IUPred3 (**a** – **c**) and AlphaFold2 (**d** – **f**) showed disorder regions of animal (**a**, **b**) and plant m^{6}A writers (**c** – **e**), and plant SE (**f**). For IUPred3 analysis, a window size of 30 consecutive residues was used. The predicted disordered and ordered regions are presented in red and blue, respectively. The left y-axis represents the tendency score, while the x-axis represents positions of amino acids. ZF, zinc finger; MTD, methyltransferase domain. **g**, **h**, 3D models of heterotypic assembly, including a human-MTC mimicking structure of MTA-MTB (**g**), and an IDR-coupled folding model of SE-MTB (**h**). Both models were predicted via the multimer module of AlphaFold2. The different entities are color-coded as indicated. In (**h**), the N-terminal IDR of MTB wrapped around the C-terminal IDR of SE to create a pivotal interaction interface which served as the nexus of the MTB-SE assembly, which was further stabilized by the N-terminal IDR of SE clasping MTB. Furthermore, the MTase domain of MTB and the zinc finger domain of SE maintained a functionally active conformation like that of MTC or the monomer, respectively. **i**, Sequence alignment of C-terminal of SE and its homologs across different species showed that R718 is conserved through plants. Predicted seven donors of hydrogen bonds in the SE-MTB interaction were highlighted in dashed boxes.

https://doi.org/10.1038/s41556-024-01530-8

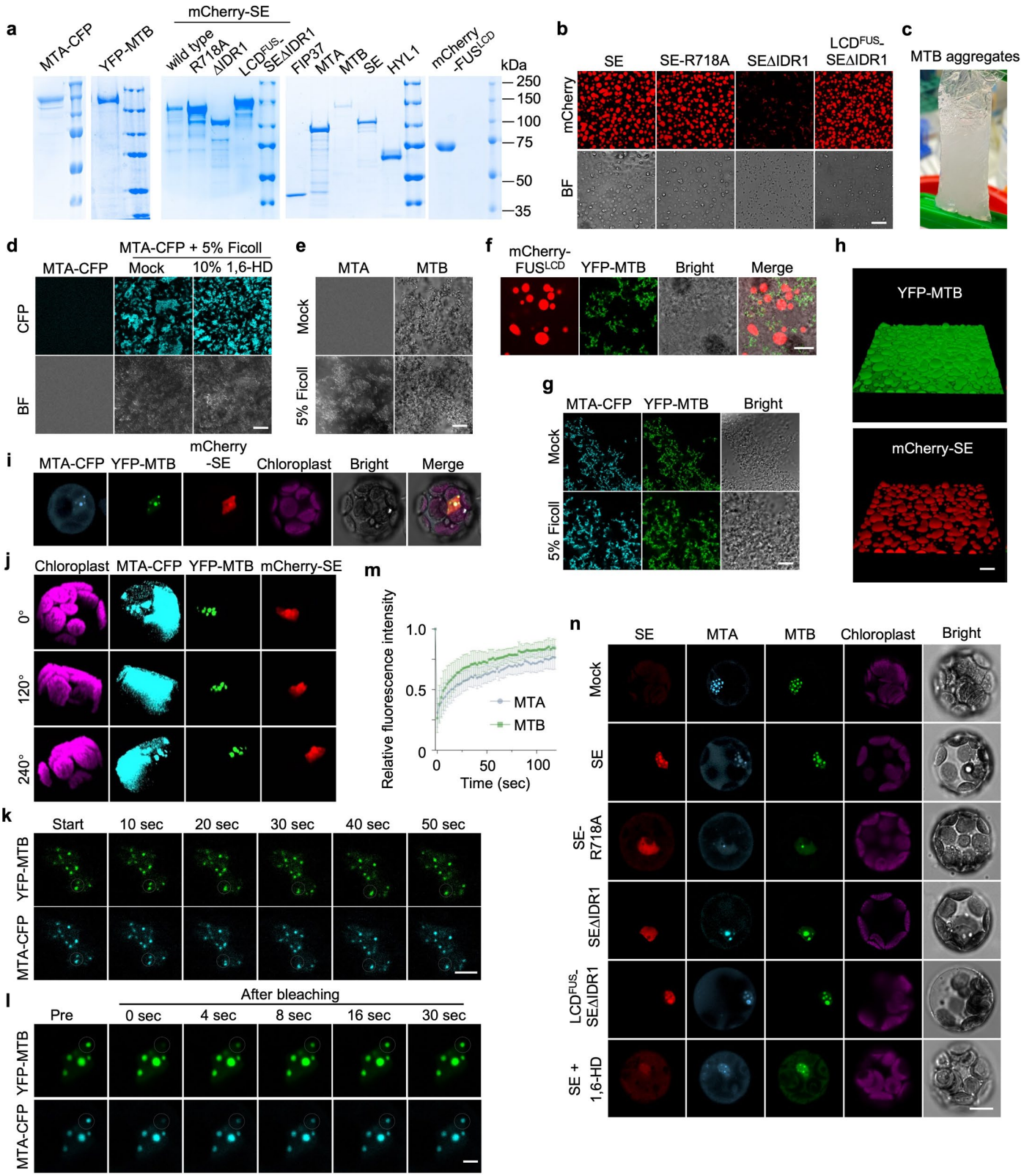

Extended Data Fig. 5 | See next page for caption.

https://doi.org/10.1038/s41556-024-01530-8

Extended Data Fig. 5 | MTA and MTB show liquid-liquid phase separation only in the presence of SE. a, Coomassie Brilliant Blue (CBB) staining of purified recombinant proteins for *in vitro* assays in SDS–PAGE gels. **b**, *In vitro* droplet formation of 3 μM purified mCherry-SE, mCherry-SE-R718A, mCherry-SEΔIDR1, and mCherry-LCD^{FUS}-SEΔIDR1. **c**, Recombinant MTB protein formed aggregates when dialyzed from high salt solution (800 mM) into a low salt (150 mM) solution. **d**, *In vitro* assays with 3 μM MTA-CFP indicated that the presence of the crowder 5% Ficoll resulted in insoluble condensates resistant to 10% 1,6-HD. **e**, *In vitro* condensate formation assays indicated that the removal of the fluorescent tag had no impact on the phase behavior of either MTA or MTB. **f**, Confocal images shows no co-condensates formed by LCD^{FUS} and MTB *in vitro*. **g**, Confocal images showed co-condensation of MTA-CFP and YFP-MTB with or without 5% Ficoll. **h**, Rendered 3D shapes of SE-MTB co-condensates. **i** – **m**, Confocal images revealed that transiently expressed MTA-CFP, YFP-MTB, and mCherry-SE in *Arabidopsis* mesophyll cells from Col-0 display liquid-like co-condensates. In (**i**), overlapped signals were observed. In (**j**), rendered 3D modeling reveals that co-condensates exhibit a spherical shape. In (**k**), fusion of co-condensates is presented with time-lapse live imaging. In (**l**, **m**), FRAP assays and the recovery curve showed that MTC displays liquid-like phase behavior. Data are mean ± s.d. of eight independent experiments. **n**, Confocal microscopic images showed the fluorescence of transiently expressed proteins in *Arabidopsis* mesophyll protoplast prepared from *se-1*. Be noted that SE and LCD^{FUS}-SEΔIDR1, but not SE-R718A and SEΔIDR1, formed liquid-like co-condensates with MTA and MTB in protoplasts. 2.5% 1,6-HD treatment was adopted 10 min prior before imaging which disrupted liquid-like condensates. For (**a**, **b**, **f**, and **n**), SEΔIDR1, plant SE depleting N-terminal IDR; LCD^{FUS}- SEΔIDR1 is a chimera protein of human FUS's LCD and SEΔIDR1; FUS^{LCD}, human FUS's LCD without SEΔIDR1. Scale bars, 10 μm (**b**, **d** – **g**), 5 μm (**h**, **n**), and 2.5 μm (**i**, **j**, **k**, and **l**). At least three independent experiments were performed (**a** – **h**), at least eight independent protoplasts were tested (**i** – **n**), and representative images are shown.

https://doi.org/10.1038/s41556-024-01530-8

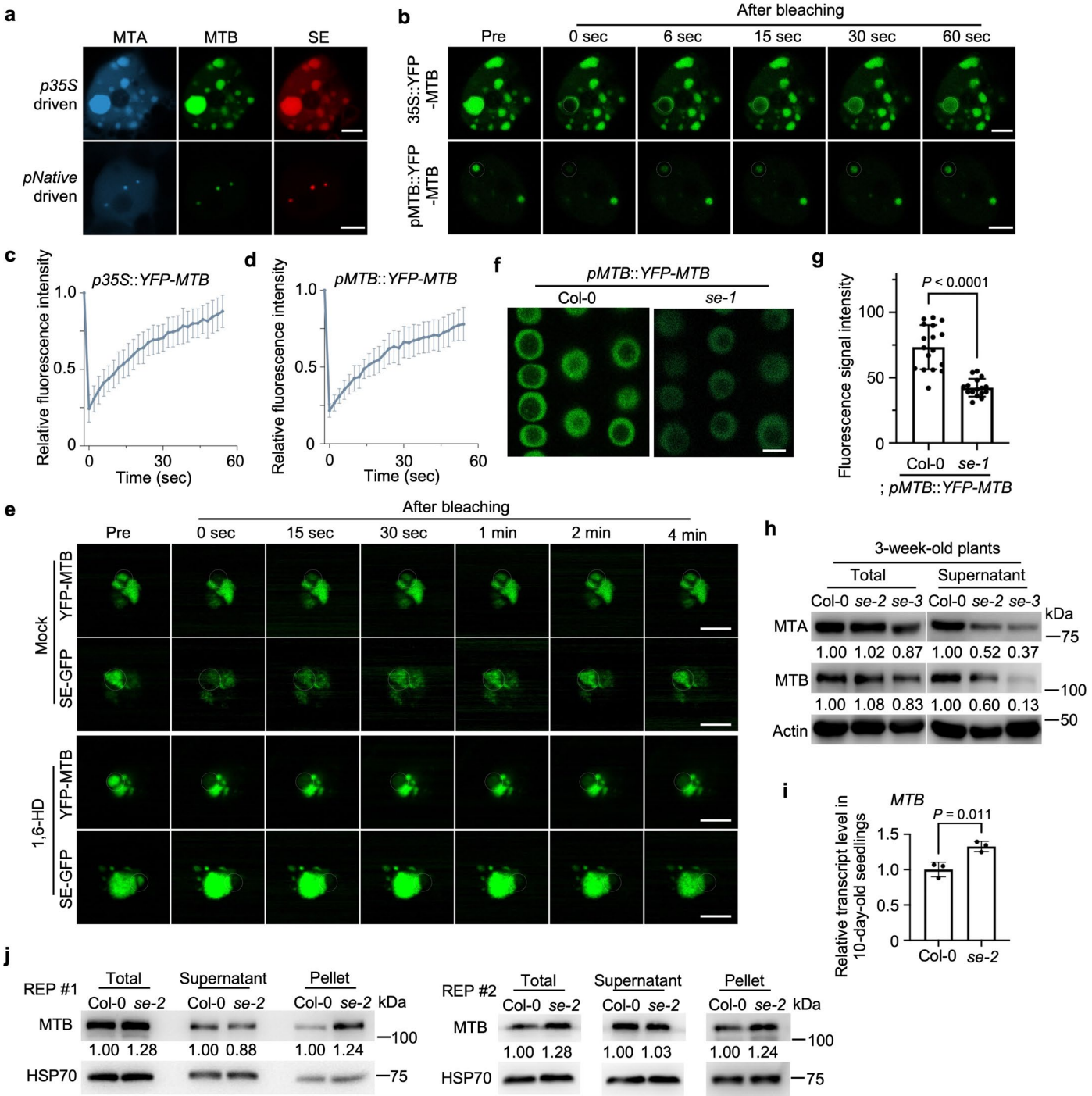

Extended Data Fig. 6 | SE regulates the phase behaviors of MTC in plants. **a** – **d**, Confocal images (**a**) and FRAP assays (**b** – **d**) revealed that SE and MTC have similar phase behaviors when transiently expressed via (**a**, **b**, **upper panels, and c**) 35S and (**a**, **b**, **bottom panels**, **and d**) their native promoters in *N. benthamiana*. Data are mean ± s.d. of at least eight independent experiments. **e**, FRAP assays showed that SE and MTB condensates undergo phase transition from liquid-like to a gel- or solid- like behavior upon 1,6-HD treatment that blocks the signal recover after bleaching. Regions of interest were labelled with white circles. **f**, **g**, Confocal images (**f**) and statistical analysis (**g**) revealed the decreased MTB signal in *se-1* vs Col-0. In (**g**), counting mode was used to analyse detectable photon for normalization. Data are mean ± s.d. of sixteen independent experiments. P value is < 0.0001, an unpaired two-sided t-test. **h**, Immunoblots with three-week-old plants detected the proteins in indicated fractions extracted from *se-2* and *se-3* vs Col-0. **i**, RNA-seq[53] analysis exhibited that increased expression of *MTB* in ten-day-old seedling in *se-2* vs Col-0. Data are mean ± s.d. of three independent replicates. P value is 0.011, an unpaired two-sided t-test. **j**, Two biological replicates of immunoblots with ten-day-old seedling detected a decreased ratio of soluble (supernatant) MTB in *se-2* vs Col-0 where the amount was arbitrarily assigned a value of 1. Scale bars, 2.5 μm (**a**, **b**, **e**, and**f**). At least eight (**a**, **b**, and**e**), sixteen (**f**), and three (**h**, **j**) independent experiments were performed, and representative images are shown.

https://doi.org/10.1038/s41556-024-01530-8

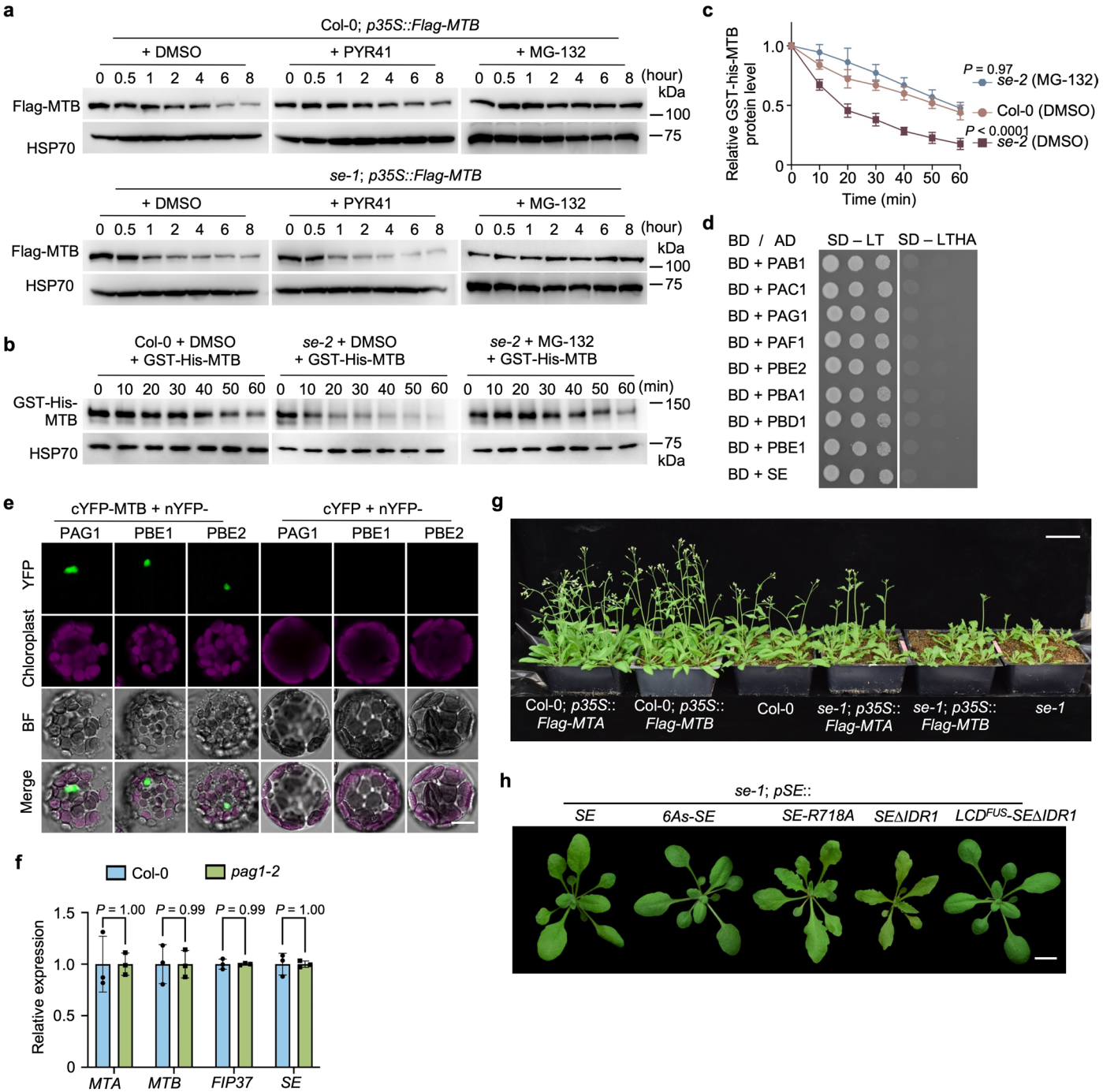

Extended Data Fig. 7 | SE stabilizes MTB by preventing 20S-proteasome-mediated degradation in plants. a – **c**, MTB-decay assays. Immunoblot assays showed that different protein stabilities of the plant MTB protein (**a**) and purified recombinant MTB protein (**b**) in the presence of the indicated reagents. The statistical analysis (**c**) of left-over MTB in (**b**). CHX, cycloheximide, 0.5 mM; MG-132, 50 μM; PYR-41, 50 μM. Only the comparisons with the Col-0 (DMSO) group are shown. P values for *se-2* (MG-132) and *se-2* (DMSO) vs Col-0 (DMSO) are 0.97 and < 0.0001, respectively. Two-way ANOVA analysis with Tukey's multiple comparisons test results. See also supplementary table 4 for detailed comparisons. **d**, **e**, Y2H (**d**) and BiFC assays (**e**) showed interactions between MTB and 20S proteasome subunits, including PAG1, PBE1, and PBE2. In (**d**), negative controls for Fig. 4h (1:10 serial dilutions) are shown. SD-LT, synthetic defined medium lacking Leu and Trp; -LTHA, lacking Leu, Trp, His and Ade. **f**, RNA-seq[15] analysis showed the expression level of m^{6}A writers in *pag1* vs Col-0. Data are mean ± s.d. of three biological replicates. P values for *MTA*, *MTB*, *FIP37*, and *SE* at *pag1-2* vs Col-0 are 1.00, 0.99, 0.99, and 1.00, respectively. Unpaired two-sided t-test. **g**, Overexpression of MTA in Col-0 and *se-1* could promote flowering time whereas overexpression of MTB could only do this in Col-0, but not in the *se-1* background. **h**, MTB-interaction compromised or IDR-depleted SE variants could not complement the developmental defects of *se-1*. 6As-SE, in which all potential hydrogen donors in C-terminal were mutated except R718; SE-R718A, which has compromised interaction with MTB; SEΔIDR1, which lacks the N-terminal IDR, failed to form spherical co-condensates; LCD^{FUS}-SEΔIDR1, a chimera protein of human FUS's LCD fused with SEΔIDR1, exhibits a pattern analogous to wild-type SE. Three-week-old plants were imaged. Scale bars, 10 μm (**e**), 5 cm (**g**), 1 cm (**h**). Three independent experiments (**a**, **b**) were performed, at least 10 independent colonies and protoplasts for each interaction were tested (**d**, **e**), at least ten transgenic plants showed similar phenotype (**g**, **h**), and representative images are shown.

https://doi.org/10.1038/s41556-024-01530-8

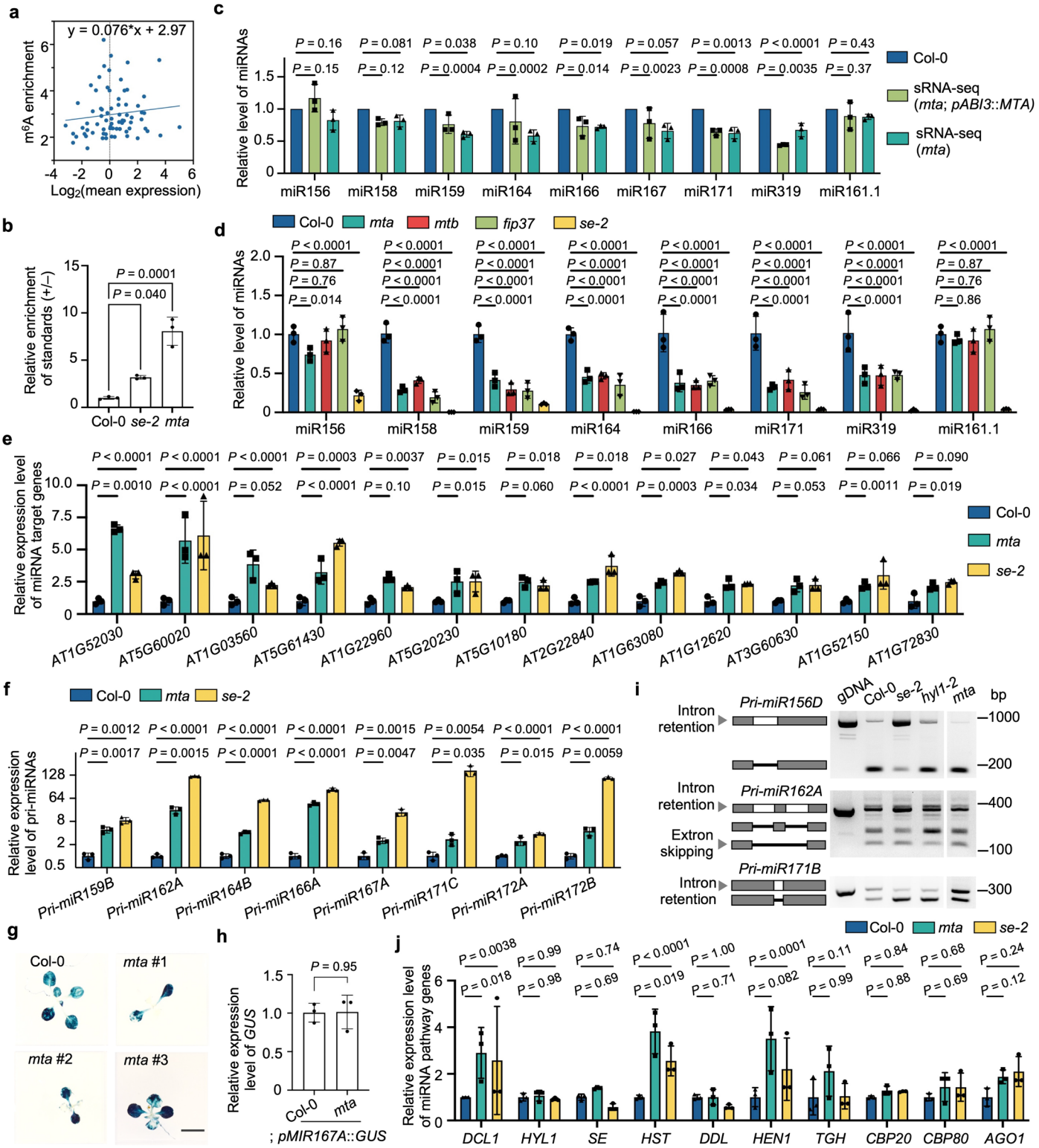

Extended Data Fig. 8 | See next page for caption.

https://doi.org/10.1038/s41556-024-01530-8

Extended Data Fig. 8 | MTC promotes miRNA production. a, Linear regression analysis did not detect significant correction between expression and methylation profiles of methylated pri-miRNAs identified by exomePeak2 in *se-2*. **b**, Statistical analysis showed that enrichment efficiencies of m^6A (+) vs m^6A (−) spike-ins were inversely correlated with the endogenous m^6A levels in m^6A-IP-qPCR. Enrichment efficiency of methylated spikes was divided by the one of unmethylated spikes in individual samples and then normalized to that of Col-0 in which the value was arbitrarily set as 1. P values for relative enrichment of standards at *se-2* and *mta* are 0.040 and 0.0001, respectively. **c** – **f**, Bar graphs showed that reduction of miRNA (**c**, **d**), accumulation of miRNA target transcripts (**e**) and pri-miRNAs (**f**) in indicated plants. In (**c**), our sRNA-seq results and public sRNA-seq[24] were exhibited in parallel. In (**d**), small RNA RT-qPCR analysis of indicated miRNAs. In (**e**), RNA-seq analysis of miRNA target genes. In (**f**), RT-qPCR analysis of pri-miRNAs. *U6* and *UBQ10* served as internal controls for normalization of miRNAs in (**d**) and pri-miRNAs in (**f**), respectively. For (**c**), p values for relative expression of miR156, miR158, miR159, miR164, miR166, miR167, miR171, miR319, and miR161.1, at the sRNA-seq of *mta*; pABI3::MTA vs Col-0 are 0.15, 0.12, 0.0004, 0.0002, 0.014, 0.0023, 0.0008, 0.0035, and 0.37, at the sRNA-seq *mta-a* vs Col-0 are 0.16, 0.081, 0.038, 0.10, 0.019, 0.057, 0.0013, < 0.0001, and 0.43, respectively. For (**d**), p values for relative expression of miR158, miR164, miR166, miR167, miR171, miR319 are all < 0.0001, for miR156 and miR161.1, at *mta* vs Col-0 are 0.014 and 0.86, at *mtb* vs Col-0 are 0.76 and 0.76, at *fip37* vs Col-0 are 0.87 and 0.87, at *se-2* vs Col-0 are both < 0.0001, respectively. For (**e**), p values for relative expression of genes at *mta* vs Col-0 are 0.0010, < 0.0001, 0.052, < 0.0001, 0.10, 0.015, 0.060, < 0.0001, 0.0003, 0.034, 0.053, 0.0011, and 0.019, at *se-2* vs Col-0 are < 0.0001, < 0.0001, < 0.0001, 0.0003, 0.0037, 0.015, 0.018, 0.018, 0.027, 0.043, 0.061, 0.066, and 0.090, respectively. For (**f**), p values for relative expression of pri-miRNAs at *mta* vs Col-0 are 0.0017, 0.0015, < 0.0001, < 0.0001, 0.0047, 0.035, 0.015, and 0.0059, at *se-2* vs Col-0 are 0.0012, < 0.0001, < 0.0001, < 0.0001, 0.0015, 0.0054, < 0.0001, and < 0.0001, respectively. **g**, **h**, MTA does not impact the transcription of *MIR167a* locus. Both histochemical staining analysis (**g**) and RT-qPCR of GUS activity (**h**) showed comparable transcriptional levels of *MIR167a* in *mta* vs Col-0. Two-week-old seedlings were analyzed. Scale bar, 0.5 cm. For (h), P value is 0.95. **i**, RT-PCR analysis showed that the patterns of pri-miRNA alternative splicing are comparable in Col-0 and *mta*. **j**, RNA-seq analysis showed that the transcript levels of microprocessor components are not decreased in *mta* vs Col-0. P values for relative expression of miRNA pathway genes at *mta* vs Col-0 are 0.018, 0.98, 0.69, 0.019, 0.71, 0.082, 0.99, 0.88, 0.69, and 0.12, at *se-2* vs Col-0 are 0.0038, 0.99, 0.74, < 0.0001, 1.00, 0.0001, 0.11, 0.84, 0.68, and 0.24, respectively. The experiments were replicated three times and representative results are shown (**i**, **g**). Data are mean ± s.d. of three independent experiments (**b** – **f**, **h**, and **j**). P values, one-way (**b**) and two-way (**c** – **e**, and **j**) ANOVA with Dunnett's multiple comparison test, and unpaired two-sided t-test (**f**, **h**).

https://doi.org/10.1038/s41556-024-01530-8

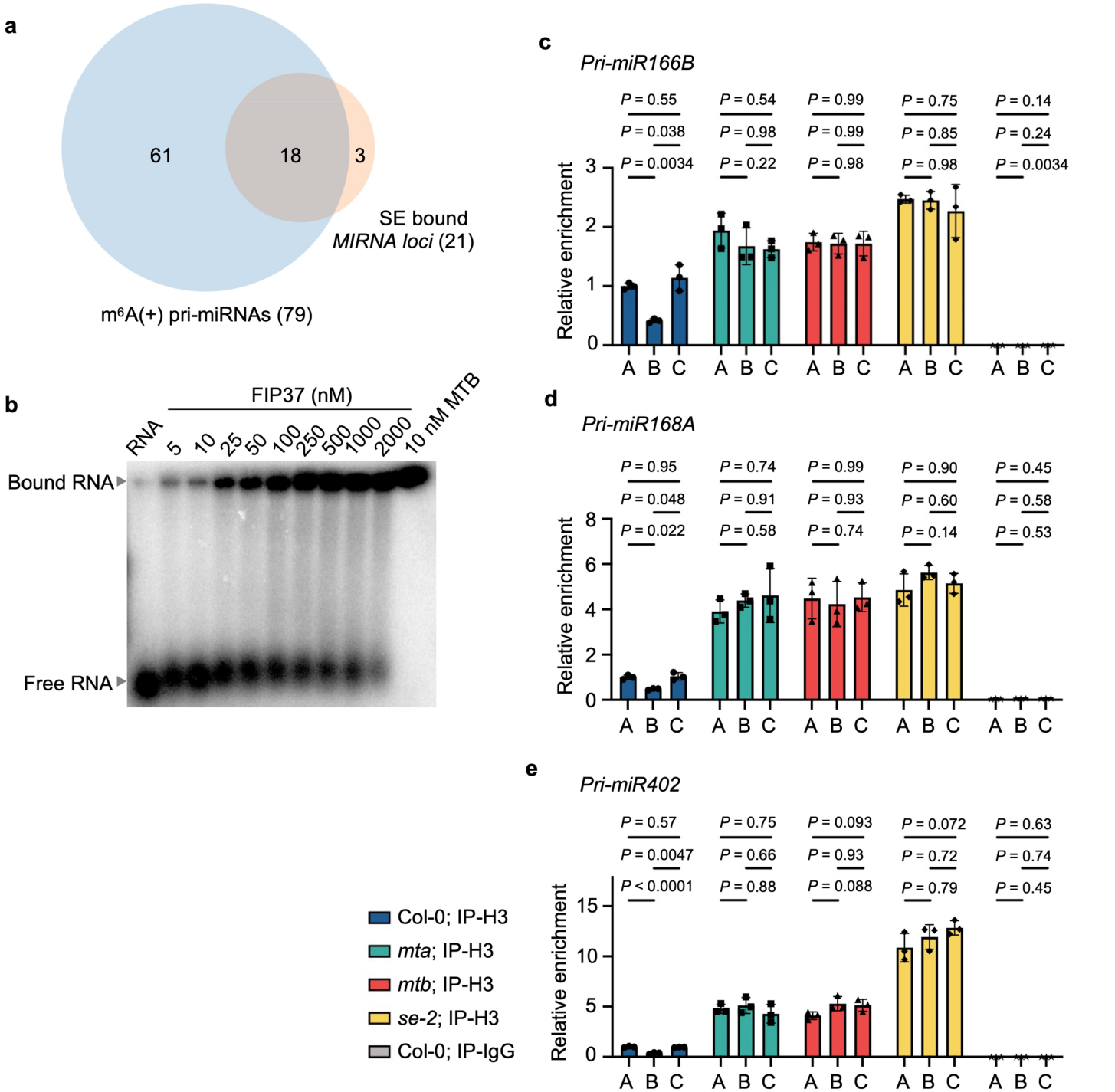

Extended Data Fig. 9 | MTC enables co-transcriptional processing of pri-miRNAs. a, Comparation of public SE ChIP-seq[36] and our MeRIP-seq on *MIRNA* revealed that SE is remarkably enriched in the loci that yield methylated pri-miRNAs. **b**, EMSA showed that FIP37's RNA affinity is much weaker than that of MTB. The experiments were replicated three times and a representative result was shown. **c** – **e**, H3-RIP-qPCR assays detected increased retention of different fragments of tested pri-miRNAs along *MIRNA* loci in the indicated mutants vs Col-0. Be noted that defective processing of pri-miRNAs was observed with pri-miR166B (**c**), pri-miR168A (**d**), and pri-miR402 (**e**) in the mutants vs Col-0. IP with IgG serves as a negative control. A, B, and C refer to 5′ flanking, pre-miRNA, and 3′ flanking sequences of pri-miRNA as indicated in Fig. 6n. Data are mean ± s.d. of three independent experiments. P values, two-way ANOVA with Tukey's multiple comparison test. For (**c**), p values for relative enrichment of A vs B, B vs C, and A vs C at Col-0 are 0.0034, 0.038, and 0.55, at *mta* are 0.22, 0.98, and 0.54, at *mtb* are 0.98, 0.99, and 0.99, at *se-2* are 0.98, 0.85, and 0.75, at IgG control are 0.0034, 0.24, and 0.14, respectively. For (**d**), p values for relative enrichment of A vs B, B vs C, and A vs C at Col-0 are 0.022, 0.048, and 0.95, at *mta* are 0.58, 0.91, and 0.74, at *mtb* are 0.74, 0.93, and 0.99, at *se-2* are 0.14, 0.60, and 0.90, at IgG control are 0.53, 0.58, and 0.45, respectively. For (**e**), p values for relative enrichment of A vs B, B vs C, and A vs C at Col-0 are < 0.0001, 0.0047, and 0.57, at *mta* are 0.88, 0.66, and 0.75, at *mtb* are 0.088, 0.93, and 0.093, at *se-2* are 0.79, 0.72, and 0.072, at IgG control are 0.45, 0.74, and 0.63, respectively.

https://doi.org/10.1038/s41556-024-01530-8

a

Bait	Gene	Log_2(fold change)	*P* values
SE	ECT1	1.5929	0.259
	ECT2	2.086	0.04206
	ECT3	4.484	0.001918
	ECT5	1.618	0.2479
	CPSF30	1.618	0.2479

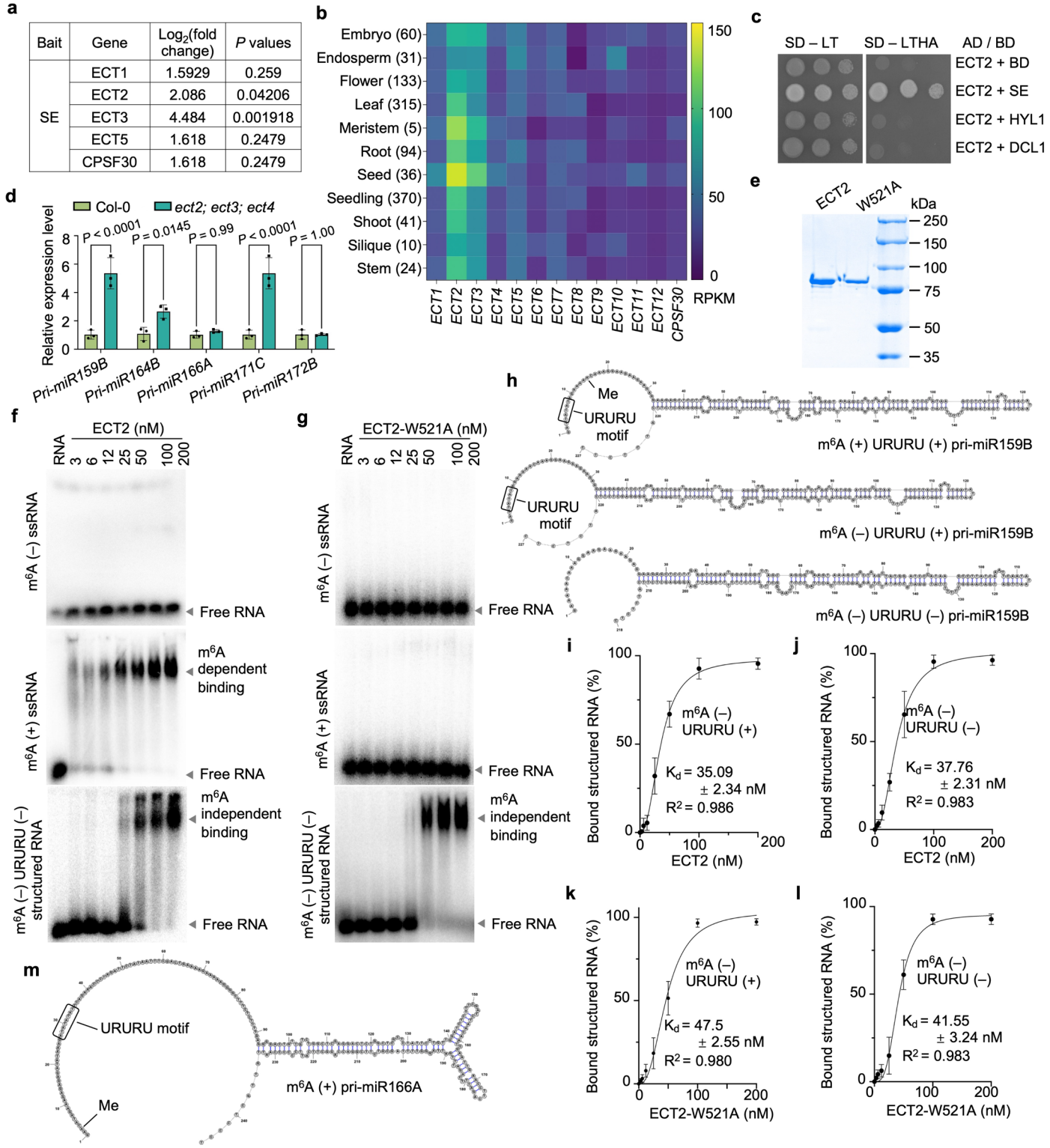

Extended Data Fig. 10 | See next page for caption.

https://doi.org/10.1038/s41556-024-01530-8

Extended Data Fig. 10 | Plant m^{6}A readers ECT2 can facilitate pri-miRNA processing via binding to m^{6}A sites whereas inhibiting the processing when binding to structured region of pri-miRNAs. a, IP-MS[39] analysis identified several m^{6}A readers in the SE immunoprecipitates. **b**, Pan RNA-seq network analysis showed the expression profiles of *Arabidopsis* m^{6}A readers across various tissues. **c**, Y2H assays showed that ECT2 interacts with SE, but not with HYL1 nor DCL1. At least 10 independent colonies tested for each interaction. 1:10 serial dilutions are shown. SD-LT, synthetic defined medium lacking Leu and Trp; -LTHA, lacking Leu, Trp, His and Ade. **d**, RT-qPCR analysis showed that the expression level of some pri-miRNAs was increased in the *ect2*; *ect3*; *ect4* triple mutant vs Col-0. Data are mean ± s.d. of three biological replicates. P values, unpaired two-sided t-test. P values for indicated genes at *ect2; ect3; ect4* vs Col-0 are < 0.0001, 0.0145, 0.99, < 0.0001, and 1.00, respectively. **e**, CBB staining of purified recombinant ECT2 and ECT2-W521A in SDS-PAGE. **f**, **g**, EMSA assays showed the capacities of ECT2 (**f**) and ECT2-W521A (**g**) binding to different substrates. For ssRNA substrates, oligonucleotides were synthesized with the context GA(m^{6}A)CAUAGAAAGAGAGAGAUAUAAA carrying a m^{6}A locus and an identical sequence without m^{6}A. Structured RNAs were folded prior to binding assays. The experiments were replicated three times and representative results are shown. **h**, Illustration and sequence of structured RNAs used in EMSA. **i** – **l**, The binding curves of ECT2 and ECT2-W521A to structured RNAs in (**f**, **g**). The K_d values were calculated from the EMSA images quantification with s.d. from three experiments, ECT2 and m^{6}A (−) URURU (+) structured RNA (**i**), ECT2 and m^{6}A (−) URURU(−) structured RNA (**j**), ECT2-W521A and m^{6}A (−) URURU (+) structured RNA (**k**), and ECT2-W521A and m^{6}A (−) URURU(−) structured RNA (**l**). Be noted that ECT2 has clearly higher binding affinity to m^{6}A-substrates than m^{6}A-lacked substrates. See also Fig. 7 for K_d of ECT2 / ECT2-W521A and m^{6}A (+) URURU (+) structured RNA. Data are mean ± s.d. of three biological replicates. **m**, Illustration and sequence of m^{6}A (+) pri-miR166A used in the processing assay.

nature portfolio

Corresponding author(s): xiuren zhang

Last updated by author(s): Jul 29, 2024

Reporting Summary

Nature Portfolio wishes to improve the reproducibility of the work that we publish. This form provides structure for consistency and transparency in reporting. For further information on Nature Portfolio policies, see our Editorial Policies and the Editorial Policy Checklist.

Statistics

For all statistical analyses, confirm that the following items are present in the figure legend, table legend, main text, or Methods section.

n/a	Confirmed
☐	☒ The exact sample size (*n*) for each experimental group/condition, given as a discrete number and unit of measurement
☐	☒ A statement on whether measurements were taken from distinct samples or whether the same sample was measured repeatedly
☐	☒ The statistical test(s) used AND whether they are one- or two-sided *Only common tests should be described solely by name; describe more complex techniques in the Methods section.*
☒	☐ A description of all covariates tested
☒	☐ A description of any assumptions or corrections, such as tests of normality and adjustment for multiple comparisons
☐	☒ A full description of the statistical parameters including central tendency (e.g. means) or other basic estimates (e.g. regression coefficient) AND variation (e.g. standard deviation) or associated estimates of uncertainty (e.g. confidence intervals)
☐	☒ For null hypothesis testing, the test statistic (e.g. *F*, *t*, *r*) with confidence intervals, effect sizes, degrees of freedom and *P* value noted *Give P values as exact values whenever suitable.*
☒	☐ For Bayesian analysis, information on the choice of priors and Markov chain Monte Carlo settings
☒	☐ For hierarchical and complex designs, identification of the appropriate level for tests and full reporting of outcomes
☐	☒ Estimates of effect sizes (e.g. Cohen's *d*, Pearson's *r*), indicating how they were calculated

Our web collection on statistics for biologists contains articles on many of the points above.

Software and code

Policy information about availability of computer code

Data collection

For confocal microscopy assays, CFP, GFP, YFP, and mCherry signals were detected with Leica stellaris 5 laser-scanning confocal microscope with a HC PL APO 63x /1.40 oil-immersion objective and LAS X Life Science Microscope Software (version 4.6.0.27096). Signals were excited with wavelengths of 405 nm, 488 nm, 514 nm, 587 nm, and 651nm, and were captured with wavelengths of 470 – 515 nm, 500 – 530 nm, 525 – 550 nm, 597 – 630 nm, and 661 – 700 nm, respectively. Chlorophyll auto-fluorescence was detected with 680 – 710 nm.
For Western blot assays, the signals were detected with ChemiDoc XRS imaging system (BioRad, version 6.1).
For small RNA sequencing and MeRIP sequencing data were collected using Illumina NovaSeq 6000 sequencing platforms.
For structural stimulation of proteins and protein complexes was performed using AlphaFold (version 2.2.0) with monomer and multimer module, respectively.

Data analysis

For confocal microscopy assays, data were analyzed with LAS X Life Science Microscope Software (version 4.6.0.27096).
For the images of processing assay, western blots, and EMSA assays were quantified with imageJ (version 1.53k), the Kd and apparant Kd were calculated using Prism 9 (GraphPad, version 9.5.1).
For small RNA sequencing analysis, Adaptors of sRNA reads were trimmed by cutadapt (version 3.4) Reads with length between 19- to 28-nt were selected and mapped to the genome using Bowtie (version 1.2.3). Bam files were sorted by SAMtools (version 1.11). Reads were counted by Subread (version 2.0.2).
For MeRIP sequencing, the raw data was trimmed by Cutadapt (version 1.18) and aligned by HISAT2 (version 2.1.0). The unique mapped reads were selected by SAMtools (version 1.9). Peak calling and compared were performed using exomePeak2 (version 1.6.1). Motif analysis was performed with HOMER (v5.1, 7-16-2024).Peak density was analyzed by Guitar (Version 2.20.0). Integrative Genomics Viewer (version 2.12.3) was used to visualize the sequencing data.
For pan-transcriptome analysis, the correlation analysis was calculated using Prism 9 (GraphPad, version 9.5.1).
The hypergeometric distribution test was conducted in R programming (version 4.3.2).

For proteins structural analysis, the PDB files were visualized using ChimeraX (version 1.4rc202205290614). The prediction of hydrogen bond networks was conducted using an online tool, https://proteintools.uni-bayreuth.de/bonds/.

For manuscripts utilizing custom algorithms or software that are central to the research but not yet described in published literature, software must be made available to editors and reviewers. We strongly encourage code deposition in a community repository (e.g. GitHub). See the Nature Portfolio guidelines for submitting code & software for further information.

Data

Policy information about availability of data

All manuscripts must include a data availability statement. This statement should provide the following information, where applicable:

- Accession codes, unique identifiers, or web links for publicly available datasets
- A description of any restrictions on data availability
- For clinical datasets or third party data, please ensure that the statement adheres to our policy

Arabidopsis thaliana reference genome (TAIR 10).
Pri-miRNA annotations were combined with dataset from PMID: 26141515 and PMID: 29124087.
For pan-transcriptome analysis, data were downloaded from http://ipf.sustech.edu.cn/pub/athrna/
All high throughput sequences data generated in this study can be access in the NCBI BioProject database under accession code PRJNA1102430.
The SE ChIP-seq data published in previous study (PMID: 30152752) can be accessed in the European Nucleotide Archive (ENA) under accession number ERP016859
The mta sRNA-seq data published in previous study (PMID: 32817553) can be accessed in the the NCBI GEO database under accession code GSE122528

Research involving human participants, their data, or biological material

Policy information about studies with human participants or human data. See also policy information about sex, gender (identity/presentation), and sexual orientation and race, ethnicity and racism.

Reporting on sex and gender	N/A
Reporting on race, ethnicity, or other socially relevant groupings	NA
Population characteristics	N/A
Recruitment	N/A
Ethics oversight	N/A

Note that full information on the approval of the study protocol must also be provided in the manuscript.

Field-specific reporting

Please select the one below that is the best fit for your research. If you are not sure, read the appropriate sections before making your selection.

☒ Life sciences ☐ Behavioural & social sciences ☐ Ecological, evolutionary & environmental sciences

For a reference copy of the document with all sections, see nature.com/documents/nr-reporting-summary-flat.pdf

Life sciences study design

All studies must disclose on these points even when the disclosure is negative.

Sample size	No statistical method was used to pre-determine sample size. Standard sample size was chosen similar to those in PMID: 29769717 and PMID: 33288888.
Data exclusions	No data was excluded.
Replication	All experiments were independently repeated more than three times with similar results obtained, and the exact replicate numbers are provided in the respective figure legends.
Randomization	Plants were randomly assigned to experimental groups whenever possible. For other experiments, the experiments were randomized and the investigators were blinded to allocation.
Blinding	The experiments were randomized and the investigators were blinded to allocation.

Reporting for specific materials, systems and methods

We require information from authors about some types of materials, experimental systems and methods used in many studies. Here, indicate whether each material, system or method listed is relevant to your study. If you are not sure if a list item applies to your research, read the appropriate section before selecting a response.

Materials & experimental systems

n/a	Involved in the study
☐	☒ Antibodies
☐	☒ Eukaryotic cell lines
☒	☐ Palaeontology and archaeology
☒	☐ Animals and other organisms
☒	☐ Clinical data
☒	☐ Dual use research of concern
☐	☒ Plants

Methods

n/a	Involved in the study
☒	☐ ChIP-seq
☒	☐ Flow cytometry
☒	☐ MRI-based neuroimaging

Antibodies

Antibodies used

Monoclonal anti-FLAG (Sigma-Aldrich, A8592,clone: M2, IB 1:5000)
Mouse monoclonal anti-actin (Sigma-Aldrich, A0480, clone:10-B3, IB 1:5000),
Polyclonal rabbit anti-histone 3 (Agrisera, AS10 710, IB 1:5000)
Polyclonal rabbit anti-AGO1 (Agrisera, AS09 527, IB 1:1000)
Polyclonal rabbit anti-SE (Seong Wook Yang's Lab, 1:5000 dilution, PMID: 32690892)
Monoclonal mouse anti-ubiquitin (Santa Cruz Biotechnology, sc8017, clone C4P1, IB 1:1000)
Polyclonal rabbit anti-HYL1 (Seong Wook Yang's Lab, PMID: 32690892)
Polyclonal rabbit anti-DCL1 (Agrisera, AS12 2102, IB 1:1000)
Monoclonal mouse anti-YFP/GFP (Roche, 11814460001, clones 7.1 and 13.1, IB 1:2000)
Monoclonal mouse anti-His (Sigma-Aldrich, H1029, clone HIS-1, IB 1:5000)
Polyclonal rabbit anti-HSP70 (Agrisera, AS08 371, IB 1:5000)
Polyclonal rabbit anti-MTA (Zhonghui Zhang's lab, full length protein expressed from E.coli, IB 1:1000)
Polyclonal rabbit anti-MTB (Zhonghui Zhang's lab, full length protein expressed from E.coli, IB 1:1000)
Polyclonal rabbit UGPase (Agrisera, AS14 2813, IB 1:5000)
IgG from huamn serum (Sigma-Aldrich, I4506, 3 µg per reaction)
Secondary antibodies were goat-developed anti-rabbit (Cytiva, NA934NA934, IB 1:3000) and anti-mouse IgG (Cytiva, NA931, IB 1:3000)

Validation

Monoclonal anti-FLAG, https://www.sigmaaldrich.com/US/en/product/sigma/a8592
Mouse monoclonal anti-actin, https://www.sigmaaldrich.com/US/en/product/sigma/a0480, and see also validation in PMID: 32690892
Polyclonal rabbit anti-histone 3, https://www.agrisera.com/en/artiklar/h3-histone-h3.html,, and see also validation in PMID: 32690892
Polyclonal rabbit anti-AGO1, https://www.agrisera.com/en/artiklar/ago1-argonaute-1.html, and see also validation in PMID: 32690892
Polyclonal rabbit anti-SE (PMID: 32690892)
Monoclonal mouse anti-ubiquitin, https://www.scbt.com/p/ubiquitin-antibody-p4d1, and see also validation in PMID: 32690892
Polyclonal rabbit anti-HYL1 (PMID: 32690892)
Polyclonal rabbit anti-DCL1 (PMID: 32690892)
Monoclonal mouse anti-YFP/GFP, https://www.sigmaaldrich.com/US/en/product/roche/11814460001, and see also validation in PMID: 32690892
Monoclonal mouse anti-His, https://www.sigmaaldrich.com/US/en/product/sigma/h1029, and see also validation in PMID: 32690892
Polyclonal rabbit anti-HSP70, https://www.agrisera.com/en/artiklar/hsp70-heat-shock-protein-70-cytoplasmic.html
Polyclonal rabbit UGPase, https://www.agrisera.com/en/artiklar/ugpase-udp-glucose-pyrophosphorylase-cytoplasm-marker-hordeum-vulgare.html
IgG from huamn serum, https://www.sigmaaldrich.com/US/en/product/sigma/i4506
Anti-rabbit, https://www.sigmaaldrich.com/US/en/product/sigma/gena9341ml, and see also validation in PMID: 32690892
Anti-mouse, https://www.sigmaaldrich.com/US/en/product/sigma/gena9311ml, and see also validation in PMID: 32690892
All commercial antibodies used were validated by original companies and inhouse with Arabidopsis proteins. All homemade antibodies used were validated by inhouse with Arabidopsis proteins and recombinant proteins.

Polyclonal rabbit anti-MTA and polyclonal rabbit anti-MTB were employed for the first time. These antibodies were generated by full length recombinant proteins expressed from E.coli. Initially, their specificity was validated by their ability to recognize the purified recombinant proteins (Supplementary Data 1). Subsequently, both antibodies were tested on plant lysates, where they effectively recognized the endogenous plant proteins. This was evidenced by the significantly decreased band intensities observed in knockdown mutants compared to wild-type plants (Extended Data Fig. 2e,f). Additionally, we generated Flag-tagged plant proteins in transgenic lines, confirming that both antibodies specifically recognized these tagged proteins (Fig. 5a).

Eukaryotic cell lines

Policy information about cell lines and Sex and Gender in Research

Cell line source(s)

sf9 insect cell, BD Biosciences, Cat# 554738

Authentication	sf9 insect cell was authenticated by vendor for recombinant protein induction and purification (BD Biosciences)
Mycoplasma contamination	All cell lines tested negative for mycoplasm contamination.
Commonly misidentified lines (See ICLAC register)	No commonly misidentified cell lines were used in this study.

Dual use research of concern

Policy information about dual use research of concern

Hazards

Could the accidental, deliberate or reckless misuse of agents or technologies generated in the work, or the application of information presented in the manuscript, pose a threat to:

No	Yes	
☒	☐	Public health
☒	☐	National security
☒	☐	Crops and/or livestock
☒	☐	Ecosystems
☒	☐	Any other significant area

Experiments of concern

Does the work involve any of these experiments of concern:

No	Yes	
☒	☐	Demonstrate how to render a vaccine ineffective
☒	☐	Confer resistance to therapeutically useful antibiotics or antiviral agents
☒	☐	Enhance the virulence of a pathogen or render a nonpathogen virulent
☒	☐	Increase transmissibility of a pathogen
☒	☐	Alter the host range of a pathogen
☒	☐	Enable evasion of diagnostic/detection modalities
☒	☐	Enable the weaponization of a biological agent or toxin
☒	☐	Any other potentially harmful combination of experiments and agents

Plants

Seed stocks	Seeds of se-1 (CS3257), se-2 (SAIL_44_G12), hyl1-2 (SALK_064863), and ect2; ect3; ect4 (CS2110132). were obtained from Arabidopsis Biological Resource Center. Artifical miRNA knock-down transgenic plants of amiR-mta, amiR-mtb, and amiR-fip37 were generated by xiuren zhang's lab in this study.
Novel plant genotypes	In summary, the amiR-mta, amiR-mtb, and amiR-fip37 exhibit phenotypic traits similar to those previously reported (PMCID: PMC5488176, PMCID: PMC6364302, PMCID: PMC5635872, PMCID: PMC6002192), including irregular leaf shapes, serration, reduced plant stature, delayed development, and late flowering.
Authentication	Seeds of se-1 (CS3257), se-2 (SAIL_44_G12), hyl1-2 (SALK_064863), and ect2; ect3; ect4 (CS2110132) were authenticated by Arabidopsis Biological Resource Center.